DISS. ETH NO. 17636

GROWTH AND CHARACTERIZATION OF THIN MANGANITE FILMS AND IN- SITU ANALYSIS OF THE LASER INDUCED PLASMA

A dissertation submitted to the

ETH ZÜRICH

for the degree of

Doctor of Natural Sciences

presented by

Stela Canulescu

Dipl. Phys. Ing., University of Bucharest

born on 02.04.1979

citizen of Romania

accepted on the recommendation of

Prof. Dr. A. Wokaun, *examiner*

Prof. Dr. D. Günther, *co- examiner*

PD Dr. T. Lippert, *co- examiner*

2008

This document has been typeset using a LaTeX typesetting system.

Things should be made as simple as possible,
but not any simpler.

Albert Einstein

Acknowledgements

There are many people I would like to acknowledge for being at the right place during this time.

First of all, I am deeply grateful to my supervisor, Dr. Thomas Lippert, for advices, continuous support, barbecue parties and for being always enthusiastic about the project. I would like to thank to Prof. Dr. Alexander Wokaun for the good supervision and for the challenging questions.

Many thanks go to the group of Solid State Chemistry and Catalysis from Materials EMPA, Dübendorf, in special to Dr. Anke Weidenkaff (group leader), Dr. Myriam Aguirre (for the TEM measurements and analysis) and Dr. Rosa Robert (for the XRD measurements).

Special acknowledgements for Dr. Camelia Borca from Micro- XAS beamline, PSI, Villigen for the XAS measurements, but also for the fruitful discussions. Many thanks to Francois Loviat for the XPS measurements, and to Dr. Jörg Wambach for the experimental support in vacuum issues.

I would like to thank to Dr. Max Döbeli from the Institute of Particle Physics, ETH Zürich, for the elemental composition measurements. I would also like to thanks to the group of D. Günther, Laboratory of Inorganic Chemistry, ETH, Zürich for the LA- ICP-MS measurements.

Many thanks to Dr. Anglos Demetrios and Dr. Evie Papadopoulou from FORTH, Greece, for their assistance during the Marie Curie Fellow, but also for the good atmosphere during the stage.

Many, many thanks to Dr. Giedrius Kopitkovas, Dr. Markus Kuhnke, Dr. Lukas Urech, Dr. Thomas Dumont, Dr. Marc Hauer for their help and collaboration in the UHV chamber setup. This project could not have been ended without their participation.

I would also like to acknowledge the youngest PhD students from my group, Ivan Marozau, Sebastian Heiroth, Franziska Simmen, Romain Fardel.

In particular, I would like to thank to Ahed Aladwan for his patience, understanding, mature advices and continuous care during my PhD period. To my friends Raluca, Daniel, Frederic (for the help with the french translation), Elsa and many, many others for helping me to socialize. Special thanks to my special friend Niels, for cheering me up a lot in the last stage of the PhD.

Lastly, my thanks go to my family, especially to my mother, for the few hundred messages she sent me during this time ...

Abstract

It has been shown that Pulsed Laser Ablation is a suitable technique for the deposition of thin films with a complex stoichiometry. This thesis comprises investigations of the ablation phenomena which are concerned with the plume expansion/dynamics, as well as studies about the film growth. In particular, Pulsed Reactive Crossed Beam Laser Ablation (PRCLA) has been selected for film deposition due to several advantages, such as an overall deposition pressure lower compared to classical PLD and the possibility to grow films without oxygen deficiencies.

The perovskite-type compounds, e.g. $La_{0.6}Ca_{0.4}MnO_3$, were selected for these studies, because they exhibit a spectacular increase of the bulk resistivity by several orders of magnitude in the presence of a magnetic field. This effect has been named colossal magnetoresistance. A possible integration of those materials in device applications based on the sensitivity to magnetic fields represents one of the major tasks for industrial applications, such as magnetic recording. The main goal for future applications is to obtain high magnetoresistance (MR) values at temperatures as close as possible to room temperature. The purpose of this study is to establish the optimum deposition conditions, i.e. substrate materials, target to substrate distance and post annealing steps, for the growth of the manganite materials. A good epitaxial quality of the films allows us to study the influence of the crystallinity on the transport properties of the films compared to the bulk material. The film microstructure and the strain induced at the substrate–film interface are important factors that influence the crystallinity of the manganite compounds, film composition, and the electrical properties.

The presence of oxygen vacancies in the manganites affects dramatically the transport properties of the materials, e.g. the magnetoresistance ratio. Heavy annealing of the manganite films leads to an increase of the oxygen content and of the Mn^{4+} species in the perovskite structure. As a consequence, the bulk resistivity decreases and the magnetoresistance ratio increases. Different annealing treatments have shown that desired electrical properties, i.e. conductivity and magnetoresistance, are obtained after heavy annealing in O_2 .

A more complex perovskite compound, i.e. $La_{0.6}Ca_{0.4}Mn_{0.8}Fe_{0.2}O_3$, has also been investigated. In this material some of the Mn ions (Jahn- Teller ions) are substituted by Fe ions (non Jahn- Teller ions), which can be used to probe the importance of the double exchange interaction (electron hopping in the Mn^{3+}- O^{2-}- Mn^{4+} network) for magnetoresistance.

The structural analysis reveal that Fe substitution in the Mn site does not change the structure significantly, but the exchange of the Mn^{3+} by Fe^{3+} results in a loss of the magnetoresistance properties, which confirms the importance of the DE mechanism.
The composition of the plume generated by laser ablation from a $La_{0.6}Ca_{0.4}MnO_3$ manganite target was studied for different irradiation wavelengths, i.e. 193 nm, 266 nm and 308 nm. A correlation of the plume dynamics and composition with the resulting properties of the grown films would allow to tune the film properties for an envisioned application.
A quadrupole mass spectrometer was employed as main analytical tool to study the ablation plume. The kinetic energy of the positive/negative ions and neutral species in the plume was measured using an electrostatic deflection energy analyzer, while the mass distribution of the species was analyzed with a quadrupole mass filter.
The data indicate that the ionic yield increases with increasing photon energy. In vacuum, the oxygen species possess higher kinetic energies compared to the other plume species, suggesting that the oxygen deficiencies in these films would be due to re-sputtering of the growing films by the high kinetic energy species.
A comparison between vacuum and PRCLA conditions (8×10^{-2} Pa O_2 and 200 kPa N_2O (τ= 400 μs)) reveals that the ablation plume and composition change drastically in the presence of the gas pulse. The N_2O gas pulse, synchronized with the laser, leads to the creation of a large amount of reactive atomic oxygen species, diatomic species, and to a decrease of the kinetic energy of the ablated species. The increase in the plume reactivity, i.e. concentration of atomic oxygen, is desired when manganite thin films are grown, in order to incorporate the necessary amount of oxygen into the film. The kinetic energy of the particles from the plume, which can also be controlled by the irradiation wavelength and background pressure, is important for the epitaxial growth of the film (together with the substrate temperature).
A large amount of negative ions is also created by the ablation process during PRCLA. They may play an important role in the plume dynamics and composition, and may also influence considerably the properties of the films. The formation mechanism of negative species and their role in the growth of the oxides remains an open question at the moment. Complementary spectroscopic methods, such as plume imaging and emission spectroscopy have been applied to analyze whether the observed Ca deficiencies in $La_{0.6}Ca_{0.4}MnO_3$ can be associated with a large angular spread of the light species within the plume. A similar compound containing an even lighter element, ($LiMn_2O_4$), was chosen to study possible different temporal and spatial dynamics of the different species. The data reveal that the lithium species have a very large angular distribution. This would imply that all

films containing Li as light element grown by PLD are deficient in the light element. The analysis reveal therefore that the large angular distribution of the light elements in the plume is indeed reflected in the film composition.

Using the same alternative spectroscopic methods, e.g. plume imaging and emission spectroscopy, a study regarding the dynamics of the plume induced by fs and ns ablation of a $La_{0.6}Ca_{0.4}CoO_3$ target was also performed because in films grown by fs irradiation Ca but also Co deficiencies were observed. The comparison of the plume for ablation with the two different pulse lengths reveals a different expansion in vacuum for fs and ns ablation. The Co I species reveal higher kinetic energies, even faster than the ions, in the case of fs irradiation, while for ns- irradiation all species exhibit similar velocities. Additionally, a more ellipsoidal shape of the plume was observed for fs ablation, while ns ablation results in a more spherical shape.

In the presence of a background gas pronounced changes were detected for fs and ns irradiation. All species revealed lower kinetic energies, and the plume appears less ellipsoidal in shape for fs irradiation. Additionally, an even stronger deceleration of the plume created by fs irradiation is detected (even slower than the species for ns irradiation), and the Co species reveal in background gas the same velocities and distribution as the other species.

Résumé

Il a été montré que l'ablation laser pulsé est une technique convenant à la déposition des couches minces ayant une stoechiométrie complexe. Cette thése étudie les phénomènes d'ablation, comme l'expansion et la dynamique de la plume, ainsi que des mesures concernant l'optimization des conditions de dépôts des couches minces.

En particulier, la technique de "Pulsed Reactive Crossed Beam Laser Ablation (PRCLA)" a été choisie pour le dépôt de couches minces pour plusieurs raisons: i) pression de dépôt inférieur comparé à PLD classique et ii) la possibilité de déposer des films avec un contenu d'oxygène plus élevé.

Parmi les matériaux perovskite, les manganites du type $La_{0.6}Ca_{0.4}MnO_3$, ont été sélectionnés parce q'ils indiquent une immense variation de résistance d'un conducteur induite par un champ magnétique externe. C'est cet effet que l'on appelle "magnétorésistance colossale". Les applications de ces matériaux sont interesantes dans le développement de nouvelles technologies, telles que les mémoires magnétiques.

Le principal objectif est d'obtenir de la magnétorésistance (MR) à une température proche de la température ambiante.

Plusieures series de dépôts ont été réalisées par ablation pulsée puor optimiser les conditions de croissance de couches minces du $La_{0.6}Ca_{0.4}MnO_3$. Nous avons varié les paramètres les plus importants, qui sont les substrats, la distance cible- substrat et les traitements de recuit subsequents. Il est important d'évaluer l'influence de la cristallinité sur les propriétés de transport des couches comparé à la cible céramique.

Nous avons observé que la microstructure du film et le stress résiduel sont des facteurs importants qui influencent la cristallinité, la composition, et les propriétés électriques des films.

Les études indiquent que l'oxygène est important pour les propriétés de transport du manganites et la magnétorésistance (MR). Un recuit prolongé augmente le contenu d'oxygène et les ions Mn^{4+}. En conséquence, la résistivité de la couche diminue et la magnétorésistance augmente. Les meilleures propriétés électriques des films sont obtenues après des recuits prolongés dans O_2.

Après avoir établi les conditions de croissance pour des couches minces de $La_{0.6}Ca_{0.4}MnO_3$, nous avons étudié l'influence de l'incorporation du Fe dans le matériau. Dans ce matériau, certains ions Mn (Jahn-Teller ions) sont remplacés par les ions Fe (non Jahn-Teller Ions), pour étudier l'effet de la double échange (DE) sur la MR.

Les analyses par diffraction des rayons X révèlent que la substitution du Mn par le Fe ne change pas la structure du matériau de manière significante, mais l'échange du Mn^{3+} par le Fe^{3+} diminue la MR, ce qui confirme l'importance du mécanisme DE.
La composition de la plume d'ablation obtenue par irradiation d'une cible de manganite $La_{0.6}Ca_{0.4}MnO_3$ a été étudiée pour différentes longueurs d'onde, soit 193 nm, 266 nm et 308 nm. L'étude de l'expansion de la plume d'ablation est nécessaire pour maîtriser les propriétés des couches minces.
Un spectromètre de masse quadrupôle a été utilisé pour l'étude de la plume d'ablation. L'énergie cinétique des ions positifs/négatifs et des espèces neutres a été mesurée avec un analyseur d'énergie électrostatique, et la distribution des espèces avec le spectromètre de masse.
Les résultats indiquent que le rendement d'émission des ions augmente avec l'énergie des photons. Dans le vide, l'oxygène possède une énergie cinétique plus élevée comparé aux autres espèces présents dans la plume. Cela suggère que le manque d'oxygène dans ces films serait due au procès de pulverasation au bombardement du substrat par des espèces ayant de hautes énergies cinétiques.
Une comparaison entre le vide et PRCLA (8×10^{-2} Pa O_2 et 200 kPa N_2O (τ= 400 μs)) revèle que la plume d'ablation et la composition change en présence de gaz. Les collisions entre les élementes éjectés et l'oxygéne provenant de la gas de N_2O, synchronisé avec le laser, permette de former d'une grande quantité d'oxygène atomique et espèces di- atomiques, et réduit l'énergie cinétique des espèces ablatés. L'augmentation de la réactivité de la plume est souhaitée pour incorporer une quantité suffisante d'oxygène dans le film. L'énergie cinétique des particules ablatés, qui peut être contrôlée par la longueur d'onde d'irradiation et le gas résiduel, est importante pour la croissance épitaxiale des couches minces.
Une grande quantité d'ions négatifs sont observées dans le procès d'ablation en présence de l'impulsion de gaz pulsé (PRCLA). Ces éspeces peuvent être importants pour la dynamique et la composition de la plume d'ablation, et peut aussi influencer considérablement les propriétés des couches minces. Le mécanisme de formation des ions négatifs et leur rôle dans la croissance des manganites restera une question ouverte pour l'instant.
Enfin, des méthodes spectroscopiques complémentaires, tels que l'imagerie de la plume et la spectroscopie d'émission, ont été appliqués pour déterminer si les carences en Ca observées dans l'ablation du $La_{0.6}Ca_{0.4}MnO_3$ peuvent être associés avec une grande distribution angulaire des espèces ablatées dans la plume. Nous avons choisi un matériel qui contient un élément léger (Li dans $LiMn_2O_4$) pour étudier la dynamique spatiale et

temporelle des espèces ablatées. Les résulats révèlent que les espèces contenant lithium ont une plus large distribution angulaire comparé aux autres éspeces de la plume. Cela impliquerait que tous les films contenant du Li comme élément léger sont déficients en lithium. Cela montre que la large distribution angulaire d'un élément léger dans le plume est reflété dans la composition des couches minces.

Les mêmes méthodes spectroscopiques, comme l'imagerie de la plume et la spectroscopie d'émission, one été utilisés pour étudier l'émission de la plume induite par impulsion de durée fs et d'une ablation de durée ns d'une cible de $La_{0.6}Ca_{0.4}CoO_3$. Les études précédentes pour synthétiser des films en ablation fs de $La_{0.6}Ca_{0.4}CoO_3$ ont montré des carences en Ca et Co.

Dans le vide, une comparaison entre les plumes d'ablation de fs et de ns révèlent une expansion différente. En cas d'irradiation de fs, les Co neutres (Co I) révèlent une énergie cinétique plus élevée que les Co ions, pendant que pour l'irradiation de ns toutes les espèces présentent des vitesses similaires. Une forme ellipsoidale de la plume a été observé pour l'ablation de fs, pendant que pour l'ablation de ns la plume est de forme sphérique.

L'éxpansion des plumes de fs et ns est différente en présence d'un gaz. L' énergie cinétique des éspeces diminue et la plume apparaît moins ellipsoïdale pour l'irradiation de fs. Une décélération plus forte est détectée dans le régime fs (même plus lent que dans le régime ns), et le Co éspeces évidencent les mêmes vitesses comme pour les autres espèces de la plume.

Contents

1 Different growth methods using a laser as irradiation source **4**

1.1 Pulsed Laser Deposition 5

1.1.1 Principle 5

1.1.2 General features 5

1.1.2.1 Plume formation near the surface 5

1.1.2.2 Plume expansion 6

1.2 Pulsed Reactive Crossed Beam Laser Ablation 7

2 Experimental **8**

2.1 Lasers and materials description 9

2.2 The High Vacuum chamber 9

2.3 The multifunctional Ultra High Vacuum (UHV) chamber 10

2.4 The quadrupole mass spectrometer (Hiden EQP) 14

2.4.1 Description and experimental notes. 14

2.4.2 Test of the sensitivity of the mass spectrometer on a NIST 610 sample . . 19

2.4.3 Time resolved mass and energy spectra 20

2.5 Plume imaging and emission spectroscopy setup at FORTH, Greece 21

3 Characterization techniques **22**

3.1 Profilometry 23

3.2 Atomic Force Microscope (AFM) 23

3.3 X-ray Diffraction (XRD) 23

3.4 Rutherford Back- Scattering (RBS) 24

3.5 Elastic Recoil Detection Analysis (ERDA) 25

3.6 Proton Induced X-Ray Emission (PIXE) 26

3.7 X-rays photoelectron spectroscopy (XPS) 26

3.8 X-ray absorption spectroscopy (XAS) 27

3.9 Electrical characterization methods 29
3.9.1 Physical Properties Measurements System (PPMS) 29
3.9.2 The Hall effect 30

4 Thin Manganite Films: Deposition and Characterization 32
4.1 **Overview of the Manganite Materials** 33
4.1.1 Lattice features 33
4.1.2 Electronic and electrical properties 34
4.2 **LCMO thin films: Morphology and Crystalline quality** 36
4.2.1 Role of the growth parameters 37
4.2.1.1 Elemental composition studies 37
4.2.1.2 Strain in thin manganite films induced by different substrates . 40
4.2.1.3 Thickness dependence on the target- to- substrate distance . . . 42
4.2.2 Microstructure of $La_{0.7}Ca_{0.3}MnO_3$ epitaxial thin films 45
4.2.3 Effect of annealing on the thin film properties 48
4.2.3.1 Morphological, compositional and electrical characterization . . 48
4.2.3.2 Study of the Mn oxidation states in $La_{0.7}Ca_{0.3}MnO_3$ films . . . 51
4.3 **Fe doped $La_{0.7}Ca_{0.3}Mn_{1-x}Fe_xO_3$ (x=0.2) thin films** 56
4.3.1 Motivation 56
4.3.2 Characterization of the $La_{0.7}Ca_{0.3}Mn_{0.8}Fe_{0.2}O_3$ the thin films 57
4.3.3 Electronic properties of the Fe (20%) doped $La_{0.7}Ca_{0.3}MnO_3$ thin films . 61
4.4 **Conclusions** 64

5 Characterization of the Plume Induced by Laser Ablation of a Manganite Target by mass spectrometry 65
5.1 Studies of the plume in vacuum 66
5.1.1 Overview 66
5.1.2 Experimental setup 66
5.1.3 Plume composition in vacuum: wavelength dependence 67
5.1.4 Laser fluence dependence on the ionic/ neutral yield. 70
5.1.5 Kinetic energy distribution of the ablated species 72
5.1.5.1 Theoretical aspects 72
5.1.5.2 Results and discussions 73
5.1.6 Angular distribution of the plume species 76
5.1.6.1 Plume angular distribution studies using a mass spectrometer . 76
5.1.6.2 Plasma analysis by a Langmuir probe 79
5.2 Interaction between the ablation plume and a N_2O reactive gas pulse 81
5.2.1 Introduction 81

5.2.2 Mass distribution of the plume species 82
5.2.3 Formation of O^+, O^- species 83
5.2.4 Formation of positive diatomic species 84
5.2.5 Formation of negative diatomic species 86
5.2.6 Discussion 87
5.3 Conclusions 89

6 Alternative spectroscopic methods for plume characterization. 90
6.1 **Study of the plume expansion during laser ablation of $LiMn_2O_4$** 91
6.1.1 Introduction 91
6.1.2 Optical emission spectroscopy studies 93
6.1.3 Time resolved imaging of the $LiMn_2O_4$ plume 96
6.1.4 Discussions 102
6.1.5 Conclusions 109
6.2 **Ns and Fs Laser Ablation of $La_{0.6}Ca_{0.4}CoO_3$: Comparison Between Plume Dynamics** 111
6.2.1 Motivation 111
6.2.2 Optical emission spectroscopy studies in ns and fs ablation 112
6.2.3 Time resolved plume imaging in fs and ns regime 114
6.2.3.1 Vacuum 114
6.2.3.2 **Plume expansion at 60 Pa O_2** 119
6.2.4 Discussions and conclusions 122

7 Conclusions 123

REFERENCES 133

CURRICULUM VITAE 141

Chapter 1

Different growth methods using a laser as irradiation source

Pulsed Laser Deposition is based on material removal when a high power laser (most commonly used are UV lasers) is absorbed by a sample. The following section will briefly describe the laser-matter interaction, as well as the dynamics of the plume expansion in different environments, such as vacuum or in presence of a background gas.

1.1 Pulsed Laser Deposition

1.1.1 Principle

Pulsed Laser Deposition (PLD) showed remarkable results for the deposition of high T_c superconductors [1], nitrides [2], carbides [3], dielectrics [4], and semiconductors [5].
The principle of pulsed laser deposition is simple and versatile: (i) an intense laser beam is focused through an optical window onto a target placed in a vacuum chamber; (ii) above a certain threshold fluence, a luminous plasma arising from the excited species of the ablated material is formed and (iii) the evaporated material will recondense on a substrate which can be placed in an **on axis** geometry (perpendicular to the expanding plume) or **off- axis** (parallel or at an angle to the expanding plume).

1.1.2 General features

1.1.2.1 Plume formation near the surface

As a consequence of the laser- matter interaction, the photon energy is coupled to the lattice through electronic processes. The absorption of the laser light by a material occurs generally over an optical depth of several nanometers. The energy is transferred to electrons (metals) or phonons (non- metals). The relaxation processes of electrons are very fast, in the order of 10^{-14} s to 10^{-13} s. It has been shown that the time scale for electron energy transfer to the lattice is around 1.5 ps for a metal, and is strongly dependent on the thermal conductivity, specific heat, and electron- phonon coupling [6]. For non metals the relaxation time varies between 10^{-12} s and 10^{-3} s.
The absorption process occurs on a much shorter time scale compared to the thermal diffusion process, giving rise to vaporization and plasma formation. The vaporization process can be described by the heat flow theory, where the surface temperature of the target at the end of the laser pulse is determined by the light absorption and thermal diffusivity. Is it therefore expected that the laser ablation mechanisms differ for nanosecond to femtosecond ablation.
Femtosecond laser irradiation
The use of fs pulses in the ablation process, and in particular for nanoparticle synthesis, has been successful demonstrated [7]. The fs ablation has several advantages compared to longer pulse lengths. Firstly, for a given fluence, a solid heats up to a higher temperature and pressure compared to ns ablation, since the energy is delivered before significant thermal conduction occurs. Secondly, there are no secondary interactions between the laser beam and the ablated material.

Nanosecond laser irradiation

For irradiation with a ns pulse, there is enough time for the thermal wave to propagate into the bulk material causing melting and evaporation of the material. There are two dominant mechanisms involved in the plume absorption, i.e. inverse Bremsstrahlung (IB) and photoionization (PI). These phenomena induce vapor ionization and excitation through collisions with excited and ground state neutrals. Ns ablation of metals results in the formation of a liquid phase and ejection of droplets which are embedded in the film. However, these drawbacks were reduced and ns lasers are used for the growth of a large variety of materials.

1.1.2.2 Plume expansion

Plume expansion in vacuum

The plume expansion in vacuum is considered adiabatic, as long as there is no mass and energy transfer to the ablation plume. According to the Anisimov model, the plume expansion is characterized by an ellipsoid. As the ablation rate (in ns ablation) exceeds 0.1 monolayer per second, high particle densities are formed at the target surface. Multiple scattering between plume species tends to thermally equilibrate the plasma, resulting in the formation of a Knudsen layer [8]. The Knudsen layer modifies the Maxwell- Boltzmann distribution to a shifted function, which includes the center of mass velocity given by equation 1.1:

$$f(v) = A \cdot (\frac{m}{2\pi k})^{\frac{3}{2}} \cdot v^n e^{\frac{-m(v-u)^2}{2kT}} dv \tag{1.1}$$

where m is the mass of the particles, k is the Boltzmann constant, v is the speed along the propagation direction, u is the stream velocity, T is the stream speed, which describes the angular distribution of the propagation, and n is an integer (typically 3-4).

Plume expansion into a background gas

A background gas can be utilized to reduce the kinetic energy of the plume species, increase the number of chemical reactions between the plume and gas molecules, and to form diatomic species. The plume dynamics is affected by the gas type and gas pressure, as it will be discussed below.

At low background pressure ($<$ 1 Pa), the plume expands similar to vacuum conditions.

At intermediate background pressures (10 Pa- 100 Pa), the background gas influences progressively the plume dynamics. During expansion in a background gas, the plume pushes the gas away, inducing a compression of the gas and of the plasma plume. When the mean free path of the plume species is reduced, a shock wave is formed, and the plume pressure equalizes the background pressure [9]. According to the model of Zeldovich and Raizer, the plume mass can be determined by equation 1.2:

$$M_p \approx \frac{2}{3} \cdot \pi R_{SKW}^3 \cdot \rho_g \tag{1.2}$$

where ρ_g represents the gas density and R_{SKW} is the distance at which the hemispherical shock wave starts.

The spherical expansion, calculated using the blast wave model can be described as:

$$R_{b.w.}(t) = \varepsilon_0 (\frac{2E_0}{\rho_g})^{\frac{1}{5}} t^{\frac{2}{5}} \tag{1.3}$$

where ε and ρ are constants determined by the specific heat ratio and the mass density of the layer.

At pressures larger than 100 Pa, a strong confinement of the plume occurs due to multiple scattering with the background gas. A stopping distance smaller than 1 cm was reported for laser ablation of a $LaMnO_3$ target [10].

1.2 Pulsed Reactive Crossed Beam Laser Ablation

The main feature of Pulsed Reactive Crossed Beam Laser Ablation (PRCLA) is the interaction between the ablated plume and a pulsed gas. The purpose of the pulsed gas valve is mainly to limit the use of the reactive gas when transfer and deposition of material occurs, but also to provide higher pressure during the interactions, yet to maintain the vacuum. This can be achieved experimentally by using a distance of maximum 1 cm between the nozzle and the ablation point on the target, which results in a strong degree of scattering between the gas and the plume species (see Figure 1.1). After passing the interaction region, the two beams expand collisionless into a low background gas (0.1 Pa) while maintaining their reactivity for the films growth [6].

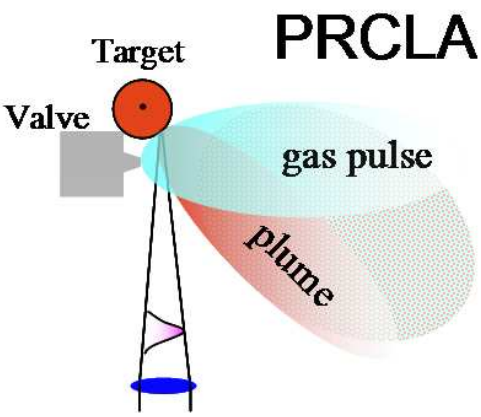

Figure 1.1: Schematic of the Pulsed Reactive Crossed Beam Laser Ablation.

Chapter 2

Experimental

This chapter describes the experimental setup and applied techniques for plasma studies. The multifunctional UHV chamber, which includes various in situ characterization techniques, such as a mass spectrometer/ion gun from Hiden Analytical, a Langmuir probe, and an emission spectroscopy will be described. Technical details of the EQP mass and energy analyzer, as well as an assessment of its sensitivity will be given.

2.1 Lasers and materials description

The ceramic targets and (100) oriented substrates used for films synthesis are summarized in Table 2.1. The targets rods, which are sintered from powders prepared by spray pyrolysis at Praxair Surface Technology, have a diameter of 12.7 mm and length of 50 mm. The substrates used for heating are Si (100) (one side polished, 10 mm x 10 mm x 0.375 cm).

Table 2.1: Targets and substrates.

Targets	Substrates (one side polished)
$La_{0.6}Ca_{0.4}MnO_3$	$LaAlO_3$ (100) (LAO)
$La_{0.6}Ca_{0.4}Mn_{0.8}Fe_{0.2}O_3$	$SrTiO_3$ (100) (STO)
	$[(LaAlO_3)O_3(Sr_2AlTaO_6)_{0.7}]$ (100) (LSAT)

The UV lasers used for the ablation experiments can be divided into two classes:
(a) excimer lasers (Lambda Physics): KrF excimer laser (λ=248 nm, FWHM 20 ns), ArF (λ= 193 nm, FWHM 25 ns) and XeCl (λ=308 nm, FWHM 30 ns).
(b) solid state lasers: Nd- YAG solid state laser (λ=355 nm, λ=266 nm, FWHM 6 ns).
The growth of the thin films was performed in the HV chamber and the plasma analysis in the UHV chamber. The two different experimental setups will be described in the following sections.

2.2 The High Vacuum chamber

The High Vacuum (HV) chamber, designed mainly for film deposition, can be evacuated with a turbo molecular pump (Pfeiffer TMU 521) to a base pressure of $\sim 3\times10^{-4}$ Pa.
The target system is assembled from the top of the HV chamber. Translation and rotation of the target is performed during deposition to ensure an uniform ablation. The target motion was set in such a way that the distance between two ablation points is $\sim$ 0.8 mm (laser frequency of 10 Hz).
The substrates are heated by clamping a Si wafer to them, while their rough sides are in contact. The Si wafers are ohmically heated by passing a DC current through them. The temperature of the Si wafers was determined by monitoring the bulk resistivity of the Si wafers and using a reference table [11]. The target to substrate distance can be varied from 3 cm to 10 cm.
The nozzle of the gas pulse is located at $\sim$ 1 cm from target and at the same height as the focused laser beam. Two different gas sources are used during film deposition, i.e. from a synchronized pulsed gas source operating at a pressure of 200 Pa O_2 or N_2O (τ= 400 ns pulse length) and an additional oxygen background pressure of 8×10^{-2} Pa. The overall pressure measured with the gauge in PRCLA is $\sim 10^{-1}$ Pa.

2.3 The multifunctional Ultra High Vacuum (UHV) chamber

Figure 2.1 shows a photograph of the UHV setup as it stands at Paul Scherrer Institut, Switzerland. The Ultra High Vacuum (UHV) can be divided into four main parts: the **Load Lock**, **Transfer Cross**, **Laser In**, and **Main Chamber**.

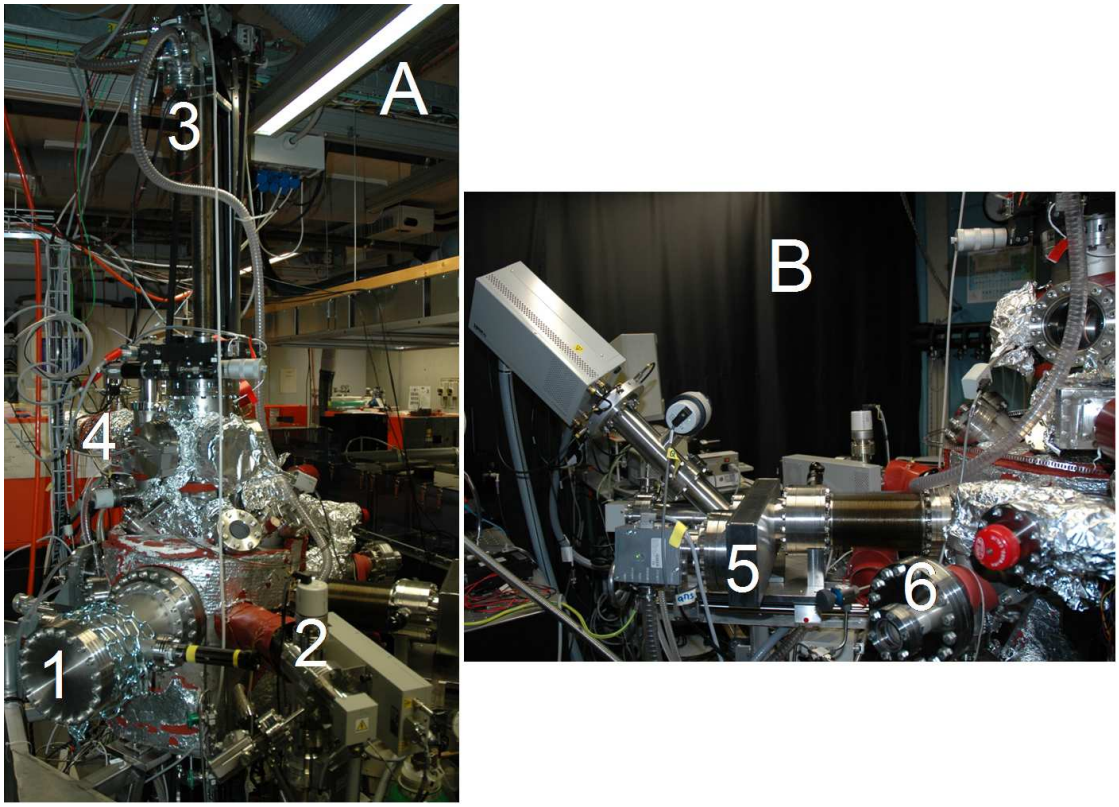

Figure 2.1: A photograph of the UHV experimental setup used in this work. On the left side (A) emission spectroscopy (1), ion gun (2), sample manipulator system (3), and load lock (4) are visible, and on the right side (B) the EQP mass spectrometer (5) and laser entrance window (6).

The **Load Lock** is designed for in- situ loading of samples. A pressure lower than 5×10^{-5} Pa is maintained in the Load Lock using a turbo molecular pump from Pfeiffer (TMU 071P). The pressure is monitored with a Compact full cathode gauge (model PKR 251). A manual manipulator assembled into the Load Lock is used for sample transfer from the Transfer Cross into the transfer cell. The Transfer cell can be afterwards unloaded and transported to the XPS setup of the General Energy Department. The cell is pumped with a battery powered ion pump which maintains a pressure lower than 10^{-5} Pa, allowing a sample transfer from the PLD chamber to the XPS chamber avoiding therefore air contaminants.

The **Transfer Cross** is used either for in situ sample transfer from the Load Lock into the main chamber (and viceversa) or for manual loading of the sample. The pressure is monitored using a Compact Pirani gauge (TPR 261).

The **Laser In** (window section) represents the entrance of the laser beam. The laser window is a made of quartz with high transparency in all regions (from UV to IR). The quartz window is mounted on a rotatable flange which can be switched from the mass spectrometer to the PLD position. The background gas is added into the chamber using a high precision leak valve attached to the window flange.

The **Main Chamber** includes various experimental techniques, such as mass spectrometry, ion gun for secondary ions mass spectrometry (SIMS), emission spectroscopy, PLD capabilities, an RF- discharge, a Langmuir probe, and a detector for metastable species (see top UHV view in Figure 2.2). The stainless steel chamber of 50 cm diameter is pumped with a 1400 l/s turbo molecular pump (Pfeiffer TMU 1601P). The pressure is monitored using a Compact full range gauge (type PKR 251). Several quartz windows, welded on flanges are located on the top of the chamber, which allow an inside view of the chamber. The chamber can be baked out up to 250^0C.

Three gate valves allow the separation between the **Main Chamber**, **Transfer Cross** and **Laser In**, as well as the separation between the **Transfer Cross** and **Load- Lock**.
The sample manipulator system allows a micrometer movement of the sample. The sample manipulator consists of five stepper motors, corresponding to the X, Y, Z axis and rotary drives for theta and phi rotation. The movement of the stepper motors is automatically controlled in Labview and the precision of the movement is on the order of a few microns. The sample manipulator coordinates (X,Y, Z, theta, phi) were determined for each experimental position using a laser diode. The reproducibility positions was ensured using optical and mechanical limit switches.
The sample holder of the manipulator can be utilized either for PLD (thin film deposition) or ablation experiments (ablation of polymers, ceramic targets).
When used for film deposition, the substrate can be heated up to $\approx$ 1000 K or cooled down to liquid nitrogen temperature (77 K). The manipulator is equipped with cooling lines for liquid nitrogen cooling and various electrical feedthrough. The sample heating is done through a Ti coil placed below the substrate holder. The coil is in mechanical contact with, but electrically isolated from the heating plate, and the temperature is monitored by a K- type thermocouple.

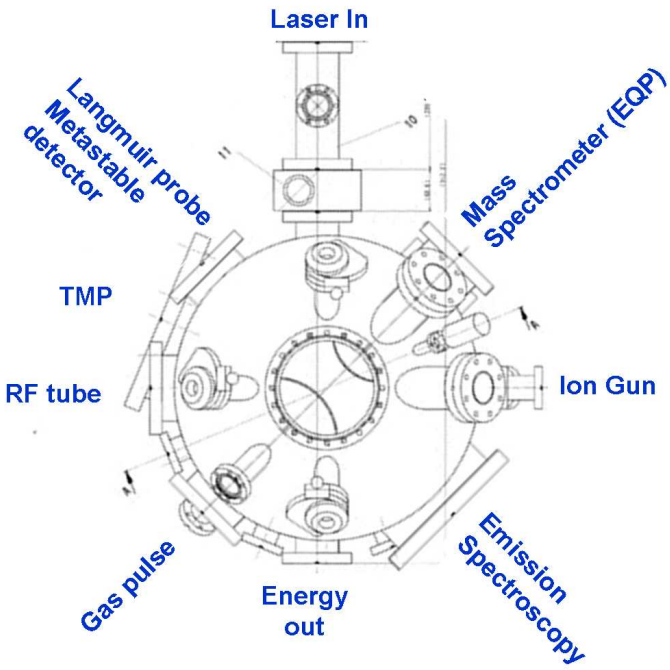

Figure 2.2: Schematic top view of the UHV chamber, showing the Laser In section, Mass Spectrometer, Ion Gun, Emission Spectroscopy, Energy Out, Gas Pulse, RF- Discharge, TMP (turbomolecular pump), Langmuir Probe and Metastable Detector.

The different setups of the UHV chamber are symmetrically placed at 45^0 with respect to each other, as shown in the sketch in Figure 2.2. The laser beam enters via the **Laser In** section and the laser energy is measured through **Energy Out**.

The Electrical Quadrupole (EQP)- mass and kinetic energy analyzer is placed at 45^0 with respect to the **Laser In**, in such a way that the expansion direction of the plume is on the axis of the mass spectrometer. The plume enters the spectrometer via an orifice with different diameter, e.g. 500 μm, 1 mm or 1 cm. The distance between the target and analyzer is variable due to a translation stage on which the mass spectrometer is placed. The mass spectrometry allows to detect the positive/negative ions and neutrals.

The ion gun is mounted at 45^0 with respect to the mass spectrometer, allowing to analyze the secondary beam originating from ion sputtering with the mass spectrometer (SIMS). As an ion source, Ar and O can be used. A Faraday can be used to measure the beam size of the Ion Gun.

The emission spectroscopy setup is placed at 90^0 with respect to the EQP in order to analyze the excited species in the plume at different distances from the target. The plume emission is imaged using a mirror system on a fiber optic to a spectrometer (Acton Research Corporation Spectra Pro-500) with an I-CCD camera (Princeton Instrument, 1024 $\times$ 256). The mirror is placed on a translation stage which can be translated along the axis of the plume expansion.

The pulsed gas source and RF discharge mounted at an angle of 45^0 with respect to each other are mainly applied for film deposition. The gas pulse is placed at a distance $\leq$ 1 cm from the ablation point of the target and the RF beam is aligned in such a way that the plasma beam can be directed towards the substrate surface during deposition. The pulsed gas source operates generally for a time of 400 μs, and the delay between the gas and the laser pulse is 400 μs. The pulse width, the repetition rate, and the delay between the gas and laser pulse are electronically controlled. The gas pulse is used at different laser frequencies, e.g. 1, 2, 5 and 10 Hz. The RF discharge can be operated using different gas, such as O_2, N_2O, NH_3, N_2, depending on the applications.

The metastable detector and Langmuir probe are both installed in a similar way as the mass spectrometer but on the left side of the chamber (45^0 with respect to the **Laser In**). The Langmuir probe is designed for ablation plume analysis of a target installed on a sample manipulator. The target system is installed on the bottom flange of the chamber and the movement is controlled as well by two stepper motors, corresponding to target translation and rotation. The system holder can have up to 5 targets, mounted on a carousel which can be rotated in order to select a particular target.

2.4 The quadrupole mass spectrometer (Hiden EQP)

2.4.1 Description and experimental notes.

The Hidden EQP is an ion energy analyzer combined with a quadrupole mass spectrometer. The EQP has a mass range from 1 to 510 amu and an ion energy analyzer in the range between -100 eV to 100 eV. The EQP has a differential pumping system using a turbo molecular pump (TMU 071P) maintaining an EQP pressure below 10^{-6} Pa in the analyzer. The pressure is monitored using a compact cold cathode gauge (type IKR 261).

The EQP can be used in two operating modes: Residual Gas Analysis (RGA) mode, mainly used for neutral analysis and SIMS, used for detection of the positive/negative ions.

A diagram of the mass spectrometer is shown in **Figure 2.3**.

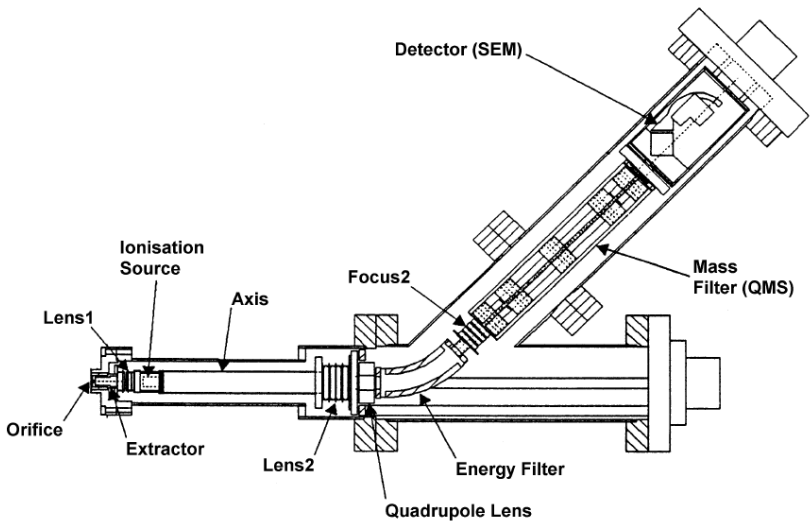

Figure 2.3: Diagram of the EQP mass spectrometer.

The main sections of the mass spectrometer, as identified in Figure 2.3 are:

Orifice represents the nozzle of the mass spectrometer.

The EQP sampling orifice is mounted in the front of the mass spectrometer and can be easily exchanged. A large nozzle diameter is used when high signal and detection sensitivity is desired. The largest nozzle, with a diameter of 1 cm, is mainly designed for SIMS, but we have it used as well for plasma analysis. When working with the largest nozzle, the laser fluence should be as low as possible, e.g. less than 0.8 Jcm^{-2} to avoid saturation of the detector [1]. The advantage

[1]Experimentally determined for the LCMO target

of using large orifices is the detection of species with low intensity, such as polyatomic species. Plasma analysis in a background gas is possible with a 1 mm and 0.5 mm nozzle only. When using the 1 cm orifice, a large amount of molecules enters the detection region and the pressure rises above 5 $\times 10^{-4}$ Pa (upper limit for optimum operating pressure of the SEM detector) for a background pressure of 0.1 Pa.

Extraction region: consists of two separate components: **extractor** and **lens 1**.
The extractor is the first electrode through which the species enter the mass spectrometer after passing the orifice. As the extraction region is placed before the ionization section, the extractor does not play a role for neutral detection, as they have no charge.

Note I: For PLD applications, when neutral species are detected a repelling voltage can be set on the extractor in order to avoid ions from the plume entering into the mass spectrometer. The voltage on the EQP extractor can be set between -100 eV and 100 eV, depending on the charge of the ions. The EQP electrode can be also used to probe the ions from the plume more efficiently. At a high repelling voltage additional effects may occur, e.g. artificial peaks in the energy spectra due the additional ionization between the cover plates and electrodes.

The species generated in the plasma can have a wide energy distribution, e.g. ranging from 1 eV up to 100 eV, or even higher. Therefore, an equal sampling of ions with a wide energy range is an important aspect for an accurate plasma characterization. Previous reports on the ion trajectory in the EQP system have shown that a large negative V_{ext} voltage results in a larger acceptance angle, because the positive ions entering the system are deflected more towards the optical axis [12].
The lens 1 refocuses the ion beam from the orifice into the exit aperture of the electron impact ion source. Tuning the lens 1 together with the lens 2 is important to maximize the ion signal. Experimental it was observed that tuning of the lens 1 increases the ion detection sensitivity at low energies.

Ionization region: Neutrals ionization region;
The ionization section acts as a field- free space for the ions, while for the neutral analysis the filaments are energized (see Figure 2.4). Neutrals entering the ion source are subjected to an electron bombardment generated by a tungsten filament with an energy of 70 eV. The ions are formed at the kinetic energy determined by the **cage** voltage, which can be set between 1- 10 eV.
Note II: The absolute kinetic energy of neutral the species is KE= $E_{measured}$- eV_{cage}.
The kinetic energy scan of N_2 neutral species measured at a static nitrogen background pressure

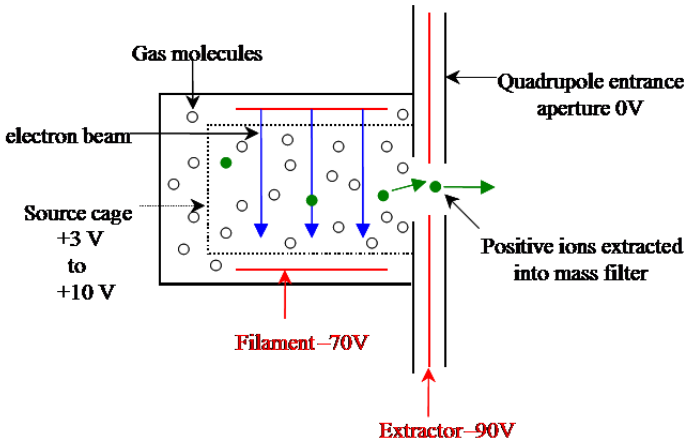

Figure 2.4: The ionization section of the QMS. The recommended operating cage voltage is between +3 V and +10 V

using different cage voltages are shown in Figure 2.5. As expected, the main energy peak is observed at the selected cage voltage, e.g. at 3 eV, 7 eV and 9 eV.

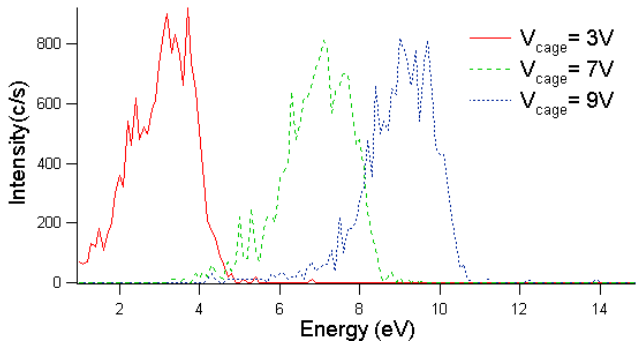

Figure 2.5: The measured energy distribution of the nitrogen neutrals ionized and accelerated at different cage voltages, e.g. 3 V, 7 V and 9V.

Deceleration region: The deceleration section consists of the **axis**, the **lens 2** and the **quadrupole lens**. This section is needed to decelerate the ions to an energy of about 40 eV. Only at this low kinetic energy ions can pass the 45° bend to the analyzer. The system of electrodes is designed as well to focus the ion beam before entering the mass energy filter.

The energy filter: Select the species according to the energy per charge ratio;
The energy analyzer filter is a 45^0 sector field analyzer, controlled by a series of variables. The electrodes controls the beam focusing, the beam astigmatism etc. The ions entering into the sector field are deflected according to their kinetic energy, so only ions with a defined kinetic

energy, e.g. 40 eV pass the bend. Considering an ion travelling along the x axis with an input energy E_i, the deflection on the y axis will be given by the expression:

$$S_y = \frac{1}{4} \cdot l^2 \cdot E_q \cdot \sqrt{\frac{q}{E}} \tag{2.1}$$

where l is the length of the sector field, E_q represents the sector field magnitude, q is the ion size and E is the input ion energy. Equation 2.1 shows that the deflection depends on the kinetic energy and is independent on the mass.

Typical kinetic energy distributions of the positive and negative ions are shown in Figure 2.6:

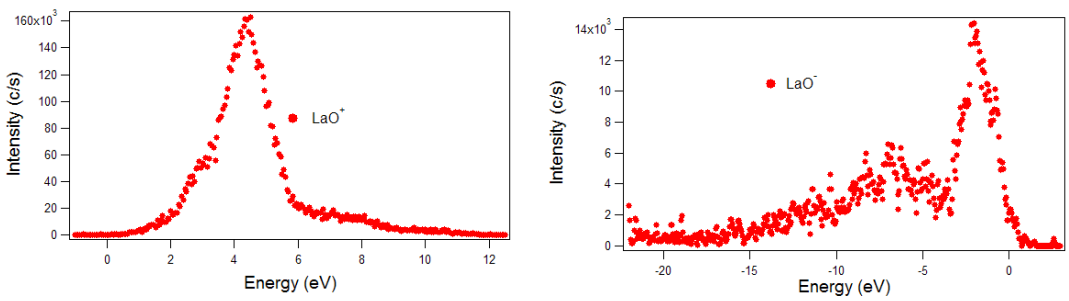

Figure 2.6: The measured energy distribution of the LaO positive ions (upper graph) and negative ions (lower graph) using an energy analyzer.

Note III: The detection of positive and negative ions is based on an electrostatic principle, therefore the detection efficiency is similar.

Note IV: The kinetic energy indicated on the X scale is proportional to the deflection voltage. A negative bias is applied for negatively charged species and a positive bias for the positively charged species. The absolute kinetic energy scale is -qV_{neg} or +qV_{pos}.

The mass filter: a focused beam with a defined energy will be separated based on the mass to charge ratio.

The ions enter the mass filter, which is a quadrupole mass spectrometer (see Figure 2.7). The quadrupole mass filter consists of four rods which generate a quadrupole electric field, induced by the superposition of AC and DC voltages. A pair of opposite rods will have a voltage $(U + V \times cos(\omega)t)$, and the other pair of rods an opposite voltage -$(U + V \times cos(\omega)t)$. Only ions with a specific mass to charge ratio will pass the mass filter and the rest will be removed. The low masses are removed by the RF field, while the high mass ions are removed by the DC voltage. By varying the U, V and/or the frequency ω, different component with different masses can be obtained.

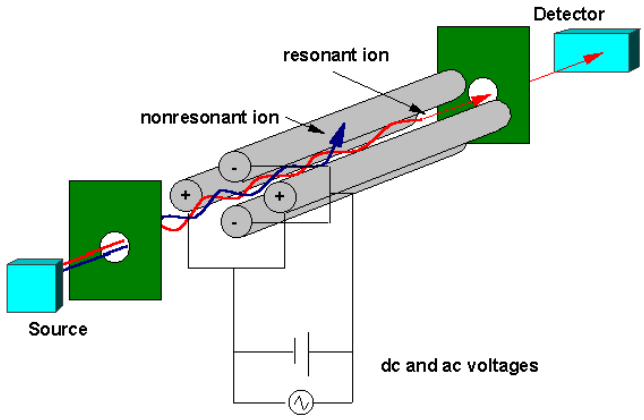

Figure 2.7: Schematic of a quadrupole mass filter.

Ion detection- SEM or Faraday cup: Ion counting, depending on the signal intensity. The detector counts the particles striking the detecting plates. When the intensity signal is below 5×10^6 c/s, the Secondary Electron Multiplier (SEM) can be used. When higher counting rates are detected, than a Faraday cup is used.

Note V: For PLD experiments, the SEM detector is commonly used. In general, the signal intensity depends on the amount of evaporated species, nozzle diameter, pumping speed in the vacuum chamber, plasma conditions and ablated material. If the mass spectra contains species with large and small intensities (e.g. Ca and LaMnO for ablation of LCMO target), the multiplier voltage can be reduced or increased, respectively. The minimum value which can be set is 2200 V, while the maximum is 3000 V. Counts lower than 500 c/s are mainly considered as background. Our experimental observations reveal that the Faraday cup gives a reasonable signal when the count rate is larger than 10^7 c/s.

2.4.2 Test of the sensitivity of the mass spectrometer on a NIST 610 sample

The detection sensitivity of the EQP spectrometer was tested using a NIST standard sample (NIST 610) which includes 61 elements. For some elements the nominal composition is specified (ppm) and for other elements no values are given. The mass spectra obatined by laser ablation at 193 nm using a laser fluence of 3 Jcm^{-2} (spot size 5 mm^2) is shown in Figure 2.8. The matrix elements have been omitted due to the high signal intensities.

The signal intensity of the elements with a concentration of between 400 ppm and 500 ppm, such as Ti, Fe, Co, Ni, Cu, Zn, Rb, Sr is quite high, and Au with a certified amount of 25 ppm was clearly detected specifically with an energy scan. Other intense lines with no quantification available are attributed to Li, Be, K, V, Ga, Mo, Cs, La, Sm, Gd, Lu, etc. (marked with □ in Figure 2.8).

The higher masses (mass ≥200 amu), such as U with a given concentration of ∼ 461 ppm could not be detected on the mass spectra and more investigations are required.

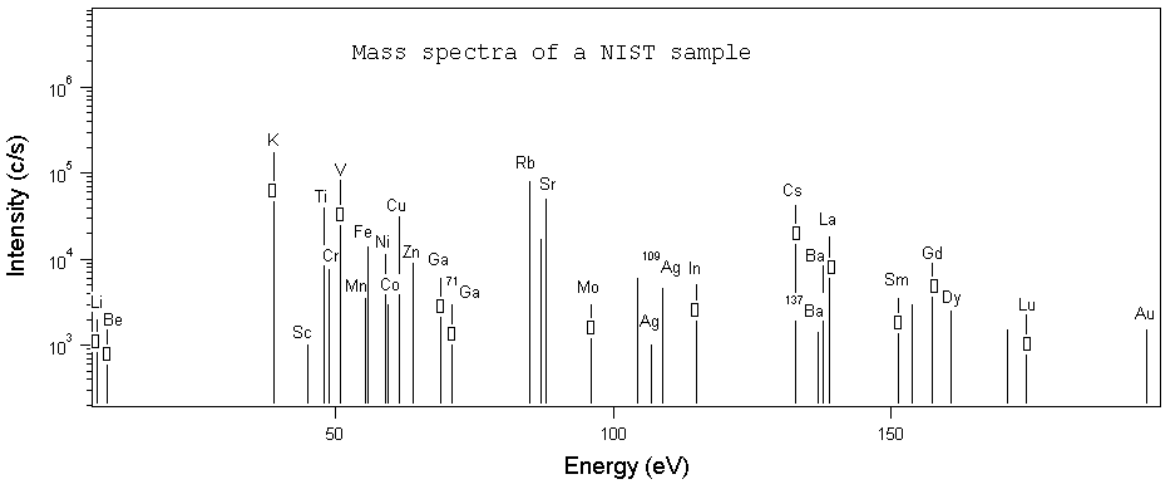

Figure 2.8: Mass spectra up to 200 amu of a NIST reference sample.

2.4.3 Time resolved mass and energy spectra

When pulsed plasmas are analyzed, the mass spectrometer is operated in the gated mode. Typical laser ablation events are measured within a time scale of few hundred microseconds. As shown in 2.9, a reference signal is used to trigger a variable delay generator which in turn generates a pulse with a specific width and delay which is sent to the mass spectrometer. The mass spectrometer acquires signal only when the gating pulse is "*on*", which is generally set to 200 μs. The laser signal measured with a photodiode and the output pulse generator are monitored on the oscilloscope.

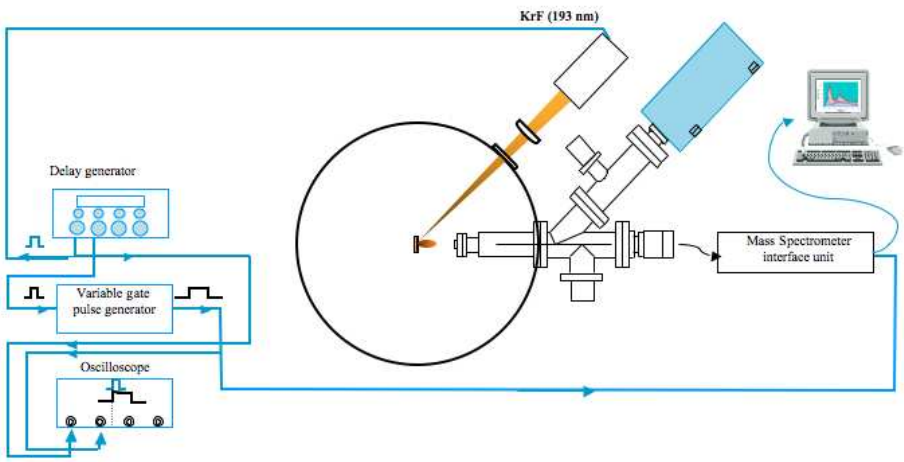

Figure 2.9: Scheme of the synchronization between the spectrometer and laser.

2.5 Plume imaging and emission spectroscopy setup at FORTH, Greece

The ablation of the $LiMn_2O_4$ (LMO) target was carried out with a 248 nm KrF excimer laser (Lambda- Physik LPX200, 34 ns) at a laser fluence of 2 Jcm^{-2}. The measurements were performed at high vacuum (base pressure of 10^{-4} Pa) and at 20 Pa of O_2 background.
A KrF ns excimer laser (λ = 248 nm, τ= 20 ns and ν =1 Hz) and a KrF fs excimer laser (λ =248 nm, τ= 500 fs and ν =1 Hz) were used for the ablation of the $La_{0.6}Ca_{0.4}MnO_3$ target (LCCO). The ns pulsed beam was focused on the target to a spot area of 1.5 mm^2, which corresponds to a laser fluence of 5 Jcm^{-2}. In the case of fs experiments, the laser spot on the target was 0.5 mm^2, resulting in a laser fluence of 3 Jcm^{-2}.
The emission spectroscopy and plume imaging setup was similar for the plasma analysis of the bulk materials, i.e. $LiMn_2O_4$ and $La_{0.6}Ca_{0.4}CoO_3$. The emission spectra were collected by focusing the plume emission onto a quartz fiber (at 1:1 magnification configuration) through an appropriate observation port on the chamber. The exit of the fiber was attached to the entrance slit of a spectrograph (TRIAX-320, Jobin Yvon-Spex) equipped with three holographic gratings, with 600, 1800 and 2400 lines/mm, providing a spectral resolutions of 0.4, 0.15 and 0.1 nm respectively. The emission was recorded with an intensified charged couple device (ICCD, DH520-18F, Andor technology) gated for an interval of tens of ns. The emission spectra were recorded in the range from 300 to 900 nm. The emission spectra were collected at different distances from the target by translating the fiber along the direction of the plume expansion. The spatial resolution was 0.5 mm. The temporal evolution of the plume was also studied for delay times from 120 to 2120 ns. The minimum delay time with respect to the laser pulse was 120 ns, imposed by the response of the electronics. Fast images of the plume were acquired by decoupling the camera, working in the time gated detection mode, from the spectrograph and focusing the optical emission onto the 1024$\times$ 256 diode array with a 1:1 magnification. Either the total emission was recorded, or just a fraction of the emission transmitted through a bandpass interference filter for selected species.

Chapter 3

Characterization techniques

The following chapter introduces the basic concepts lying behind the analytical techniques applied for the characterization of the thin manganite films. A wide range of techniques, including surface morphology analysis (AFM), crystallographic studies (XRD), elemental analysis (RBS, ERDA, PIXE), electronic analysis (XPS and XAS), and electrical characterization (Hall effect) will be described briefly.

3.1 Profilometry

Profilometry is commonly used to estimate step heights (and thus film thickness) and surface roughness. The principle consists of an electromagnetically sensing of the mechanical movement of a stylus as it traces the topography of a film step.
A Dektak 8000 profilometer with a tip size of 5 μm was used. The profilometry allows scanning of the films over a large scan length (1 cm in our case). Moreover, the estimated surface roughness by profilometry was found to be in agreement with the AFM measurements.

3.2 Atomic Force Microscope (AFM)

The principle of an atomic force microscope is similar to a stylus profiler, but the probe forces on the surface are much smaller. Smaller probes can be therefore used, and much higher resolution can be achieved. At the same time, the vertical expansion is limited, hence the method is useful for scans of low surface roughness. The AFM consists of a tip which makes soft physical contact with the sample (see Figure 3.1). As the tip approaches the sample surface, the strong repulsive forces will cause bending of the cantilever. The cantilever has a spring constant lower than the effective spring constant holding the atoms of the sample together. Scanning the tip across the surface, a topographic map of the sample surface can be obtained.
The surface morphology was analyzed using an Atomic Force Microscope from Park Instruments operating mainly in contact mode. Different scanning heads were used (5μm$\times$ 5μm, 20μm$\times$ 20μm and 50μm $\times$ 50μm), depending on the analyzed area of the sample.

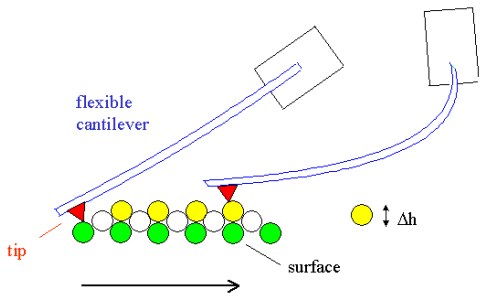

Figure 3.1: Schematic diagram of the AFM operating in contact mode.

3.3 X-ray Diffraction (XRD)

X-ray diffraction (XRD) was used to examine the phase purity, crystallographic quality, orientation, and lattice constants of the manganite thin films prepared by the PRCLA technique.

The structural quality of the films was analyzed with a Siemens (D5000) diffractometer, equipped with an Eulerian cradle for texture analysis, in a standard θ- 2θ configuration. The scans were performed using unfiltered Cu Kα radiation.
The powder samples were measured by X-ray diffraction using a Philips X'Pert PRO MPD T-T system equipped with a linear detector (X'Celerator).

3.4 Rutherford Back- Scattering (RBS)

The Rutherford Backscattering technique (RBS) is applied to determine the elemental composition of a layer. RBS is a non-destructive technique based on detection of the backscattered ions (typically He) which have undergone elastic scattering with the atomic nuclei of the sample. An ion with an initial energy E_0 and mass M_p will have after elastic scattering an energy E_1 (see Figure 3.2) given by the equation:

$$E_1 = \left[\frac{\sqrt{M_r^2 - M_p^2 sin^2\theta} + M_p cos\theta}{M_r + M_p} \right]^2 \times E_0 = K(\theta) \times E_0 \tag{3.1}$$

where M_r is the mass of the target atom, θ is the scattering angle and $K(\theta)$ the kinematic factor.

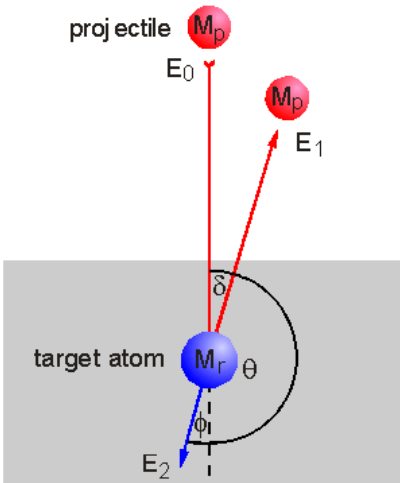

Figure 3.2: The principle of Rutherford Backscattering.

The cross section of the Coulomb scattering is given by the expression:

$$\sigma(\theta) = (\frac{ZrZ_pe^2}{4E_0})\frac{1}{sin^4(\theta/2)} \tag{3.2}$$

where Z_r and Z_r are the atomic number of the incident and target atom, respectively and E_0 is the energy of the incident atom.
The equations 3.1 and 3.2 reveal that the energy and angular distribution of the backscattered ions contain information about the target atoms.

Furthermore, as the projectile passes through the bulk material it looses energy through electronic excitations and ionization of target atoms. Knowledge of the rate of energy loss, dE/dx, of an ion travelling through a solid, allows to determine the thickness and composition of the sample.

In RBS a sampling depth of 1- 2 μm can be achieved, providing thus information about the bulk composition of the film, but RBS shows a poor resolution for heavy atoms, such as W, Ta, and Fe, and for relatively light atoms such as C, N and O. The accuracy for metals is approximately $\pm$ 5% and can reach 10 % for oxygen. This is the reason why ERDA is complementarily used for O content determination in some cases.

Experimental, a primary 2 MeV ^{4}He beam and a silicon surface barrier detector at 165 degree are used. The collected RBS data were simulated using the RUMP software. The measurements and data processing were performed at the PSI/ETH Laboratory for Ion Beam Physics [1].

3.5 Elastic Recoil Detection Analysis (ERDA)

In ERDA, the sample is irradiated with highly energetic heavy ions, such as Xe under grazing conditions, as it is shown in Figure 3.3. The energy and the number of the scattered atoms are measured at a fixed angle relative to the beam direction. The energy and time-of-flight with fixed flight path of the outscattered atoms of the sample are measured at the same time. The various masses are identified based on their kinetic energy, resulting in a two- dimensional plot with time versus energy.

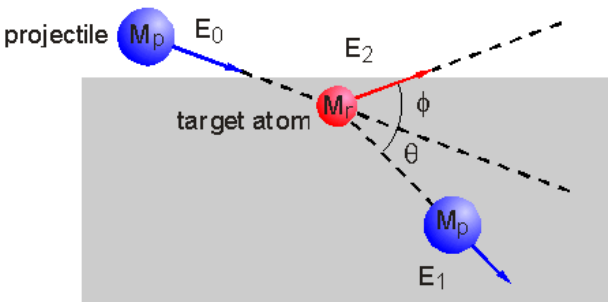

Figure 3.3: The principle of Elastic Recoil Detection Analysis (ERDA).

For the ERDA analysis a 12 MeV ^{127}I beam was used under 18^0 incidence angle. The scattered recoils were identified by the combination of a time-of-flight spectrometer with a gas ionization chamber

In ERDA the detection sensitivity is almost the same for all elements. The accuracy of the the oxygen content is much higher compared to RBS and a maximum error of 5% can be assumed.

[1] http://www.ipp.phys.ethz.ch/research/experiments/tandem/

3.6 Proton Induced X-Ray Emission (PIXE)

Proton Induced X- Ray Emission (PIXE) consists in the irradiation of the sample with high energy protons. The elemental composition of the sample is determined based on the X- ray emission of the excited atoms. Only X-rays with energy above 2 keV, i. e. from elements heavier than phosphorus, can be detected in air. The absorption of the X-rays depends on the composition and layer structure of the sample.
PIXE measurements were performed at the PSI/ETH Laboratory for Ion Beam Physics using a 3 MeV proton beam. Characteristic X-ray spectra were measured by a Si(Li) detector.
PIXE analysis was employed to determine the elemental ratio Fe/Mn in the $La_{0.6}Ca_{0.4}Mn_{0.8}Fe_{0.2}O_3$ films, as RBS could not resolve these masses. The evaluation of the Fe content was extracted from the ratio of the Fe/ Mn K- beta peak area. Since the K lines of Mn and Fe are very close in energy, an absorption correction has to be performed. This was verified by comparing the intensity ratios of the K-alpha and K-beta lines of Mn and Fe.

3.7 X-rays photoelectron spectroscopy (XPS)

The photoemission process consists in the ejection of an electron from the core level upon X ray photon irradiation (typically soft X- rays). A diagram of the X- ray Photoelectron Spectroscopy (XPS) process is shown in Figure 3.4. The kinetic energy (KE) of the emitted photoelectron can be estimated by equation 3.3:

$$KE(eV) = h\nu - BE(eV) - W \tag{3.3}$$

where $h\nu$ is the photon energy, BE(eV) is the binding energy of the electron and W is the spectrometer work function.
The most commonly used photon energies are 1253.5 eV (MgK_α) and 1486.6 eV (AlK_α). Experimentally, by measuring the kinetic energy of the photoelectron with a Kinetic Energy Analyzer (KEA), the binding energy of the electron can be determined. Therefore, it is possible to determine the elemental composition of the surface, the spatial distribution of the materials in three dimensions, and the valence state of the elements at the surface.
The mean free path (nm) of the electron is given by the Seah and Dench equation:

$$\lambda = \frac{A_i}{kE^2} + B\sqrt{(kE)} \tag{3.4}$$

where A_i and B_i are tabulated constants depending on the material type and E is the electron energy.
The corresponding sampling depth is:

$$\Lambda = \lambda \cdot cos(\theta) \tag{3.5}$$

where λ is the mean free path and θ is the emission angle. The maximum sampling depth can therefore be achieved at θ= 0, and around 95 percent of the electrons will emanate from a distance of 3λ. The probing depth of XPS spectroscopy varies between 1 and 10 nm.

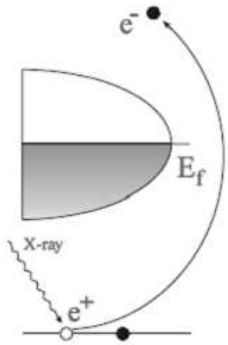

Figure 3.4: The XPS emission of an electron from a core level into vacuum.

In particular, XPS was applied to analyze the surface composition of the $La_{0.6}Ca_{0.4}Mn_{0.8}Fe_{0.2}O_3$ layers. The technique was successful applied for the identification of film impurities, such as Si and Ru, as well as for determination of the Mn and Fe oxidation states.

3.8 X-ray absorption spectroscopy (XAS)

The XAS technique provides information about valence states and electronic configuration of the elements in bulk, which is different to XPS, where a thin surface layer is probed.
The X- ray absorption principle, shown in Figure 3.5, illustrates the emission of a photoelectron from the core level to a level above the Fermi level. In X- ray absorption spectroscopy the probability that an incident X- ray photon will be absorbed by a sample is measured as a function of photon energy, which can be varied between 4 and 21 KeV. A typical XAS spectrum recorded over a large energy range is shown in Figure 3.6. Three different regions can be distinguished: XANES (X-Ray Absorption Near Edge Structure), NEXAFS (Near- Edge Absorption Fine Structure), EXAFS (Extended X-Ray Absorption Fine Structure).
The features in the pre-edge region are usually contributions from electron transitions from the core level to the higher unfilled or half-filled orbitals (e.g, s$\longrightarrow$p, or p$\longrightarrow$ d). In the XANES region, transitions of core electrons to non-bound levels occur. The transition probability gives rise to a sudden increase of absorption.

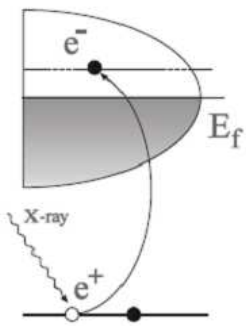

Figure 3.5: The XAS emission of an electron from a core level into an unoccupied level above the Fermi level.

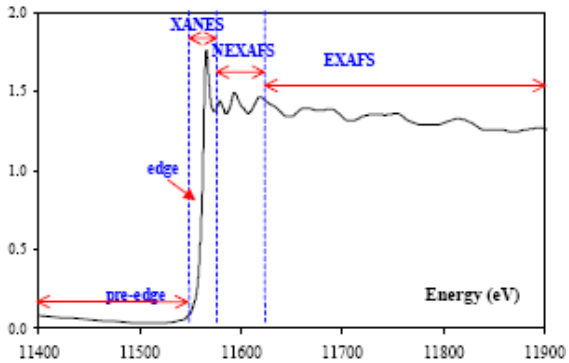

Figure 3.6: The typical XAS spectrum of a solid.

In NEXAFS, the ejected photoelectron have low kinetic energy and experience strong multiple scattering by the first and even higher coordinating shells.

In the EXAFS region, the photoelectrons have high kinetic energy and single scattering by the nearest neighboring atoms normally dominates.

The XANES technique has been used to analysis powders and thin films, and the results are included in the Chapter **Thin Films Manganite: Deposition and Characterization.**

Experimentally, XANES spectra at the K-edges were collected by Camelia Borca at the Swiss Light Source, at the new undulator microXAS beamline using the Si (1 1 1) double-crystal monochromator. The beam size at the sample position was 0.7 mm $\times$ 1 mm. The fluorescence mode (for thin films) as well as the transmission mode (for reference samples) has been used to acquire spectra at room temperature. The energy shifts between the various spectra were established by a careful comparison with spectra obtained from standard compounds.

XAS was applied for the analysis $La_{0.6}Ca_{0.4}Mn_{0.8}Fe_{0.2}O_3$ crystalline films. The changes in the core level binding energy of Fe and Mn were determined by comparison with the reference powder sample.

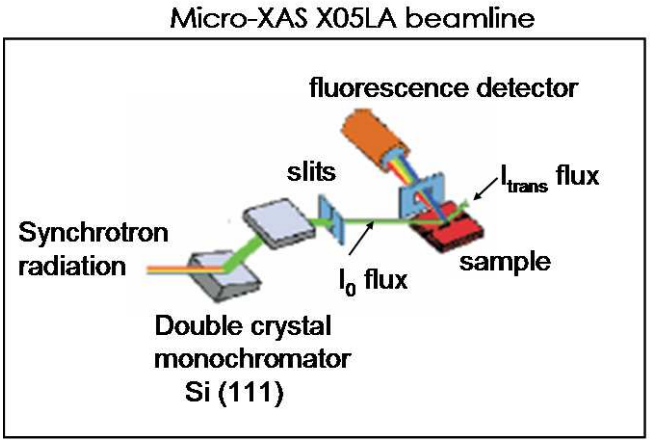

Figure 3.7: The diagram of the XAS setup.

3.9 Electrical characterization methods

For the electrical characterization of the manganite thin films two setups were used, i.e. a Hall effect measurement device (HEM 300) and a Physical Properties Measurements System (PPMS).

3.9.1 Physical Properties Measurements System (PPMS)

The PPMS machine is suitable for the electrical resistivity measurements of the thin films within a wide temperature range (2 K- 400 K) and magnetic field strengths range from 0T to 9T.
The technique for electrical resistivity measurement relies on the four point method, which is shown in Figure 3.8. A current is applied between the external contacts and the voltage reading is done between the internal contacts, as it is shown in Figure 3.8, left.

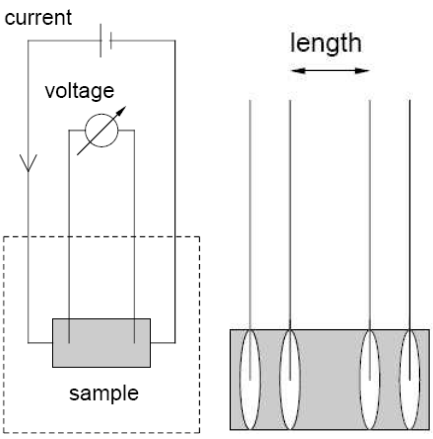

Figure 3.8: Schematic view of the four point circuit, left, and geometry of the contacts on the sample, right.

Thin gold wires have been connected to the surface of the sample in a geometry shown in Figure

3.8 using silver paste to ensure reliable contacts.
It is suggested that for a quantitative data analysis, applied mainly for bulk materials, the specimen resistivity can be calculated:

$$\rho_{spec}(\Omega cm) = \rho \cdot \frac{A}{l} \tag{3.6}$$

with l being the length of the sample enclosed by the voltage contacts, and A the cross section of the sample.
Our thin films have a square geometry, allowing to calculate the bulk resistivity as:

$$\rho_{spec}(\Omega cm) = R(\Omega) \times d(cm) \tag{3.7}$$

where R(Ω) is the resistance of the sample and d(nm) is the films thickness.
The manganite thin films have an electrical resistance at RT between 10 kΩ and 100 kΩ. As the resistance increases towards lower temperatures, the PPMS machine reaches the measuring limits, which is for our samples ∼7 MΩ.

3.9.2 The Hall effect

The resistivity in the Hall effect device is determined with the Van der Pauw method, in which the contacts are applied on the corner of the square sample. A main requirement is that the average diameters of the contacts, and sample thickness must be much smaller than the distance between the contacts.
Similar to the four point method, four wires are connected to the four ohmic contacts on the sample.
The schematic of a Van der Pauw configuration, used in the determination of the two characteristic resistances R_A and R_B, is shown in Figure 3.9 [2].
Firstly, the ohmic contact quality and sample uniformity are verified. Measurement consistency following current reversal requires that all measured resistances are positive and:

$$R_{21,34} = R_{12,43}\,;\, R_{43,12} = R_{34,21}\,;\, R_{32,41} = R_{23,14}\,;\, R_{14,23} = R_{41,32} \tag{3.8}$$

Moreover, the reciprocity theorem requires that:

$$R_{21,34} + R_{12,43} = R_{43,12} + R_{34,21}\,;\, R_{32,41} + R_{23,14} = R_{14,23} + R_{41,32} \tag{3.9}$$

The errors should be less than 3 %.
The sheet resistance R_S can then be determined from the two characteristic resistances:

$$R_A = (R_{21,34} + R_{12,43} + R_{43,12} + R_{34,21})/4; R_B = (R_{32,41} + R_{23,14} + R_{14,23} + R_{41,32})/4 \tag{3.10}$$

[2] http://www.eeel.nist.gov/812/meas.htm

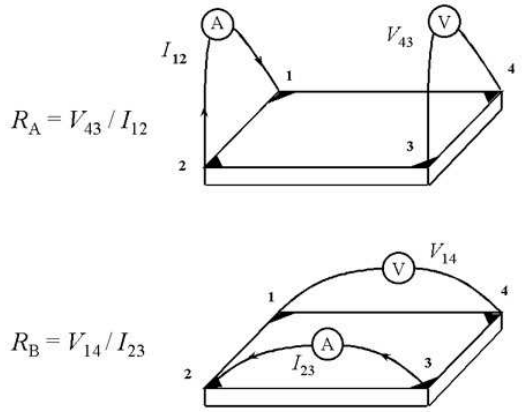

Figure 3.9: Schematic view of the Van der Pauw configuration used to determine the two characteristic resistances R_A and R_B.

using the van der Pauw equation:

$$exp(-\pi R_A/R_S) + exp(-\pi R_B/R_S) = 1 \tag{3.11}$$

If the conducting layer thickness d is known, then the bulk resistivity can be calculated as $\rho = R_S \times d$.

Chapter 4

Thin Manganite Films: Deposition and Characterization

[1]

In this chapter, we present the most important features of the epitaxial $La_{0.6}Ca_{0.4}Mn_{1-x}Fe_xO_3$ (x= 0, 0.2) thin films. The structure and morphology of the films are analyzed in relation to the growth parameters. The effect of Fe doping on the electronic and electrical properties of the $La_{0.6}Ca_{0.4}Mn_{1-x}Fe_xO_3$ (x=0, 0.2) films will be discussed.

[1]The following chapter has resulted in the following publications:

1. S. Canulescu, T. Lippert, H. Grimmer, A. Wokaun, R. Robert, D. Logvinovich, A. Weidenkaff, M.Döbeli, Structural characterization and magnetoresistance of manganates thin films and Fe-doped manganates thin films, Applied Surface Science 252, 4599- 4603, 2006.
2. S. Canulescu, Th. Lippert, A. Wokaun, R. Robert, D. Logvinovich, A.Weidenkaff, M. Döbeli, M. Schneider, Preparation of epitaxial $La_{0.6}Ca_{0.4}Mn_{1-x}Fe_xO_3$ (x= 0, 0.2) thin films: variation of the oxygen content, Progress in Solid State Chemistry 35, 241- 248, 2007.
3. S. Canulescu, Th. Lippert, A. Wokaun, M. Döbeli, A. Weidenkaff, R. Robert, D. Logvinovich, The effect of the fluence on the properties of La-Ca-Mn-O thin films prepared by pulsed laser deposition, Applied Surface Science 253, 8174–8178, 2007.
4. C. N. Borca, S. Canulescu, F. Loviat, D. Grolimund, T. Lippert, A. Wokaun, Analysis of the electronic configuration of the pulsed laser deposited $La_{0.7}Ca_{0.3}MnO_3$ thin films, Applied Surface Science 254, 1352–1355, 2007.
5. M.H. Aguirre, S. Canulescu, R. Robert, N. Homazava, D. Logvinovich, L. Bocher, T. Lippert, M. Döbeli and A. Weidenkaff, Structure, microstructure and high temperature transport properties of $La_{1-x}Ca_xMnO_{3-\delta}$ thin films and policrystalline bulk materials, to be published in Journal of Applied Physics.

4.1 Overview of the Manganite Materials

One of the most fashionable electric technologies, i.e. spintronics, make use of an electron's spin (with its orientation up or down), in addition to its charge, to store or transmit information. The giant magnetoresistance (GMR), which has been observed for the first time in 1988 in multilayers [13], was rapidly applied in reading heads for hard drives. In GMR materials, a weak magnetic field is applied to align the spin of electrons, inducing a change of 20 % in the electrical resistance of the material.

One decade later, a change of the bulk resistivity by several orders of magnitude was reported, and this became known as the "colossal magnetoresistance" effect (CMR). Von Helmholt et al. reported a magnetoresistance of about 60% in $La_{0.67}Ba_{0.33}MnO_3$[14], and M. McCormack et al. measured a magnetoresistance of the La-Ca-Mn-O layers that exceeded 99.92% at 77 K [2] [15].

The discovery of the CMR effect has fuelled a lot of enthusiasm in the research work, as well as from technological interest. During the attempts to understand the physics of the CMR, many interesting properties of the manganites have been discovered, such as charge ordering, phase separation, and half metallicity, and there is still a large interest in the manganites.

In particular, the mixed-valence perovskites $RE_{1-x}M_xMnO_3$ (RE= rare earth, M = Ca, Sr, Ba, Pb) are intensively studied, as large CMR values were reported. At low and large x values, the polycrystalline materials show antiferromagnetic (AF) insulating behaviour and for a value around x≈ 1/3 ferromagnetic (F) metallic behaviour [16], [17]. The research was further extended on layered manganites materials, such as $La_{2-2x}Sr_{1+2x}M_2O_7$ [18] and $SrMn_{1-x}Fe_xO_{3-\delta}$ (x= 1/3, 1/2, 2/3) [19]. The investigations were carried out on single crystals and thin films which have shown an even larger CMR effect.

A complete understanding of the CMR effect in manganites includes knowledge of the crystal structure, electronic, and transport properties, which are discussed below in detail.

4.1.1 Lattice features

The parent compound of the CMR manganites is the antiferromagnetic $LaMnO_3$ material, with an orthorhombic structure. The partial substitution of the trivalent La ions by divalent ions, such as Ca, Sr, Ba, results in the formation of CMR materials, with a $La_{1-x}M_xMnO_3$ composition. The crystal structure of the manganite materials is shown in Figure 4.1, in which a divalent or a trivalent ion, such as La^{3+} or Sr^{2+} occupies a 10- fold coordination site, while the Mn ions (with mixed valence Mn^{3+} and Mn^{4+}) occupy a 6- fold coordination site and are surrounded by oxygen octahedra.

[2] Here, the CMR is defined as $\Delta\rho/\rho_0$. In the cited paper, the definition $\Delta\rho/\rho_H$ is used and gives a value of 127 000%.

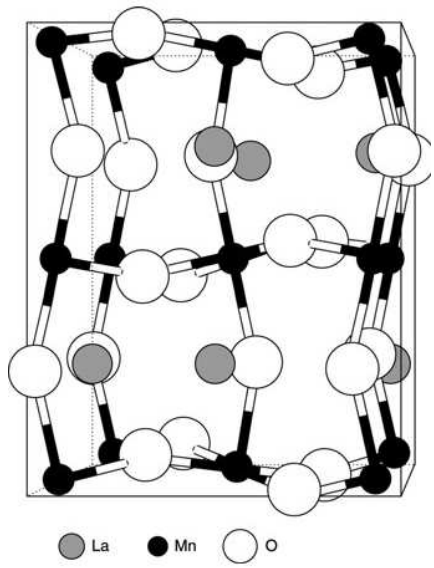

Figure 4.1: Crystallographic structure of $LaMnO_3$.

Divalent ion doping is governed by the tolerance factor which determines the stability of the perovskite structure. The tolerance factor is defined as:

$$t = (r_{A^{2+/3+}} - r_O)\sqrt{2}/(r_O - r_{Mn}) \tag{4.1}$$

The perovskite structure is stable when the tolerance factor ranges between 0.89 and 1.02, where t = 1 corresponds to the perfect cubic structure [20].

4.1.2 Electronic and electrical properties

Small or large cation doping of the perovskite structure induces tilting or buckling of the oxygen octahedra, respectively. In both cases, the Mn^{3+}- O^{2-}- Mn^{4+} angle deviates from 180 degree, inducing therefore a change in the electronic conduction. The hopping probability of the e_g electrons from Mn^{3+} to neighboring Mn^{4+} is given by the relation [21]:

$$t \propto d^{-3.5} \sin(\theta/2) \tag{4.2}$$

where d is the Mn- O bond length and θ is the bond angle. Relation 4.2 suggests that a change of the Mn-O-Mn bond angle (θ) results in a change of the electrical conductivity. The bulk resistivity is therefore determined by the elemental composition of the material.

The main consequence of divalent ion doping is the formation of Mn^{3+} and Mn^{4+} ions. The crystal field theory is used to explain the role of the manganese on the transport properties and CMR effect.

In the antiferromagnetic material $LaMnO_3$, the configuration of the outer electrons of the Mn^{3+} ions is $3d^{4+}$. The crystal field interaction induces a splitting of the 3d orbitals into two sets,

e_g and t_{2g} states, as shown in Figure 4.2. The electrons from the t_{2g} levels, lower in energy are more localized, while the e_g electrons are more delocalized, allowing a hopping from site to site. As an electron hops into an empty e_g orbital of the Mn^{4+} ion via the double exchange mechanism, it interacts with the crystal field, resulting in a distortion of the oxygen octahedra and thus lowering of the energy. The electron together with the crystal lattice forms a so-called lattice polaron, with larger mass and lower mobility than that of a free electron.

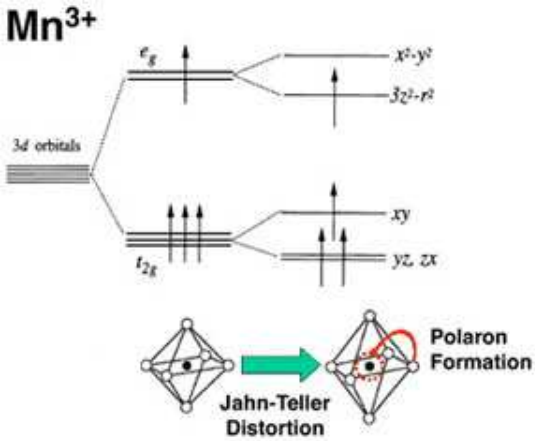

Figure 4.2: The splitting of the Mn 3d levels into e_g and t_{2g} levels and the resulting Jahn-Teller distortion.

The polaron conduction, e.g. lattice distortion accompanying the move of the charge carriers, is the main conduction mechanism of the manganites in the paramagnetic phase, e.g. $T > T_c$ [22]. According to polaron conduction, the bulk resistivity above the Curie temperature (T_c) is given by the equation:

$$\rho \sim T \exp(\frac{\rho_0}{k_b T}) \tag{4.3}$$

The ***double exchange interaction*** is used as a main mechanism to explain the CMR (colossal magnetoresistance) effect in manganites. A scheme of the double exchange mechanism (DE) is shown in Figure 4.3. According to the DE mechanism (introduced by Zener [23]), the e_g electrons can simultaneous jump from the Mn^{3+} ions to the Mn^{4+} ions through the intermediate of the oxygen ions. According to the hopping polaron mechanism (defined previously in equation 4.2) the transfer integral of e_g electrons is maximum for parallel alignment of the spin and minimum for antiparallel alignment of the spin, sugesting therefore a strong correlation between conductivity and ferromagnetism.

In the ferromagnetic phase ($T \leq T_c$), the resistivity exhibits a dependence on the temperature given by the expression:

$$\rho \approx \rho_0 + aT^2 \tag{4.4}$$

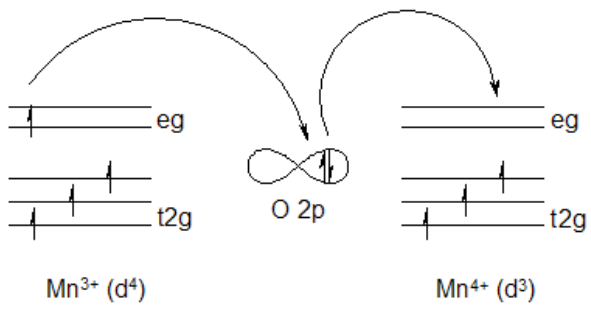

Figure 4.3: The schematic of the double exchange interaction.

4.2 LCMO thin films: Morphology and Crystalline quality

The properties of the manganites can vary considerably from polycrystalline to single crystalline ceramics and/or thin films. Larger magnetoresistance values have been reported for thin films compared to the bulk materials [24]. The magnetic properties of the manganites can be tuned from the paramagnetic to the ferromagnetic and antiferromagnetic phase according to the doping level of the divalent ions [25].

Pulsed Laser Deposition (PLD) is an established technique for the growth of oxide thin films, including high temperature superconductors [26], CMR materials [21] etc. PLD allows also the synthesis of layers with compressive/tensile strain, depending on the choice of substrate [27]. The CMR properties of the films depend also on the applied strain in films.

For the growth of oxide films, an oxidizing environment (N_2O or O_2) is applied for obtaining films with a desired oxygen content and crystal phase. One approach to improve the oxygen content in films was the development of Pulsed Reactive Crossed Beam Laser Ablation (PRCLA), where a synchronized reactive gas pulse interacts with the plasma plume close to the ablation point. The film quality is strongly dependent on the background pressure and on the target to substrate distance. Reports from a classical PLD system reveal that the plume length determines the morphology and microstructure of the growing films [28].

This chapter includes studies on the growth of the $La_{0.7}Ca_{0.3}MnO_3$ manganite thin films. Firstly, the influence of the experimental parameters, such as laser fluence, substrate- type and target to substrate distance, on the surface morphology and crystallinity of the manganite thin films will be discussed. Secondly, we study the effect of the post annealing treatments on the properties of the manganite films. The results will be correlated with the transport properties of the thin films, and especially with the colossal magnetoresistance.

4.2.1 Role of the growth parameters

4.2.1.1 Elemental composition studies

PLD is a technique which allows a stoichiometric transfer of the material, but sometimes an incongruent transfer in the PLD process has been reported [29]. Several factors may account for the incongruent transfer, such as laser parameters (laser fluence), interaction processes in the gas phase, preferential re- emission from the deposited films, or thermally- induced processes on the hot substrate. The laser fluence is an experimental parameter which determines the kinetic energy of the plume species and the amount of the evaporated material per pulse. High fluences used in the ablation process may induce deficiencies of the elements in the growing films due to the bombardment of the growing films with ions and atoms which may also contain high energy particles that can re-sputter material from the growing film. Incongruent transfer was for example reported during laser ablation of a FeSiGaRu target, using a fluence higher than 6 J cm^{-2}, due to the preferential sputtering of gallium [29].

We have therefore investigated the elemental composition of the thin films prepared from a target $La_{0.6}Ca_{0.4}MnO_3$ as a function of the laser fluence, ranging from 2 Jcm^{-2} to 8 Jcm^{-2} (see Figure 4.4). All films were grown on $SrTiO_3$ substrates. According to the RBS analysis, the composition of the films follows the same trend for laser fluences ranging from 2 Jcm^{-2} to 7 Jcm^{-2}. For the highest applied fluence (8 Jcm^{-2}) RBS analysis reveals a non- uniform elemental composition through the film. The composition determined by RBS analysis is the average composition over the films thickness. The RBS data indicates a slightly incongruent transfer of the material, e.g. the growing films are Ca and O deficient. Ca enrichment at the surface (and therefore depletion in bulk) has been previously reported during the growth of the La - Ca - Mn - O films and it was mainly attributed to a surface segregation process [30]. The deficiencies were observed at temperatures higher than 700^0 C, while in our studies the deficiencies are observed also at lower temperatures, e.g. between 600^0C and 650^0C.

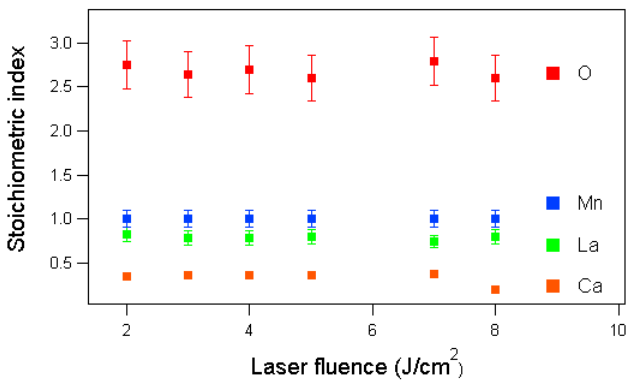

Figure 4.4: Composition of the $La_{0.6}Ca_{0.4}MnO_3$ films deposited at various laser fluences. The relative error is 5 percent.

As mentioned before, the laser fluence determines the amount of material ablated per laser pulse. The average growth rate (calculated as the ratio between films thickness and number of pulses) dependence on the laser fluence is shown in Figure 4.5. The data suggest thus the growth rate increases as expected with the laser fluence. An increase in the laser fluence from 2 Jcm^{-2} to 8 Jcm^{-2} corresponds to an increase of the growth rate from 0.012 Å/pulse to 2.15 Å/pulse (see Fig. 4.5), respectively.

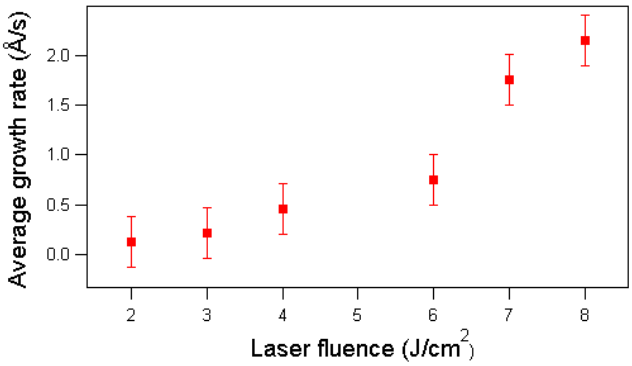

Figure 4.5: Average growth rate of the $La_{0.6}Ca_{0.4}MnO_3$ films versus laser fluence.

A comparison between the elemental composition of the powder/target material and thin films was carried out. EDX and LA- ICP- MS analysis reveals a nominal composition of the target of $La_{0.6}Ca_{0.4}MnO_3$, which is in agreement with the manufactures specifications (Praxair Surface Technology). The film composition, evaluated by both EDX and RBS/ERDA, analysis indicates a deviation in Ca and O content compared to the target reference system (see Table 4.1). Deficiencies of light elements, such as O and Ca, in the films grown by PLD may be attributed to the larger angular scattering of the light elements in the plume, as previously observed for Li in $LiMn_2O_4$ [31].

Table 4.1: Elemental composition of the powders and thin films measured by EDX and RBS/ERDA.

Element	Powder sample (EDX)	Thin films (EDX) ± 5 %	Thin films (RBS/ERDA) ± 5 %
La	0.630±0.050	0.770±0.050	0.74
Ca	0.365±0.040	0.2350±0.040	0.28
Mn	0.950±0.050	0.800±0.010	1
O	2.950±0.050	0.270±0.15	2.77

Furthermore, the grown films exhibit a variation in composition with depth, as observed by RBS (qualitative) and EDX (quantitative) analysis. The data in Table 4.2 show a variation in

composition by 10 % of the top surface layer compared to the interface layers. This may be attributed to changes of the target surface during ablation or to surface segregation phenomena at the surface of the films [30]. It has been suggested that the elements with low binding energies have a high probability to segregate at the surface. Ca exhibits the lowest binding energy among the elements in the target, and has therefore the highest probability to segregate at the surface. Previous reports in literature have shown that strain can lead to the formation of secondary phases at the interface with Ca excess [32]. Our results show that films with composition of $La_{0.7}Ca_{0.3}MnO_3$ are obtained from a target with a composition of $La_{0.6}Ca_{0.4}MnO_3$. In the forthcoming chapter we will use the resulting composition of $La_{0.7}Ca_{0.3}MnO_3$.

Table 4.2: EDX analysis of the near surface layer and interface layer of the thin films obtained from a target of $La_{0.6}Ca_{0.4}MnO_3$.

Element	Near Surface	Near Interface
La	0.690±0.050	0.770±0.050
Ca	0.3650±0.040	0.235±0.040
Mn	0.895±0.010	0.800±0.010
O	2.950±0.050	2.7±0.150

Any deviation from the target stoichiometry can affect dramatically the transport properties of the thin films. It was shown that the mixed Mn^{3+}/Mn^{4+} valence states in $La_{0.7}Ca_{0.3}MnO_3$ compound induce both ferromagnetism and metallic behavior in manganites and are responsible for the occurrence of the colossal magnetoresistance effect. A change in the Ca content induces a change in the Mn^{3+}/Mn^{4+} ratio, and thus different electrical characteristics, e.g. CMR and transition temperature. It it therefore necessary to establish the optimum deposition parameters for the growth of films that reveal CMR properties.

Another important aspect which influences the CMR properties is the oxygen content. The oxygen deficiency in films deposited at high temperature is less understood. Preferential resputtering or re- evaporation would induce the observed oxygen deficiencies in the films, but the oxygen content in the films can be controlled by different post deposition treatments in oxygen atmosphere, as described later in the thesis.

4.2.1.2 Strain in thin manganite films induced by different substrates

We studied the influence of the strain from different substrates, but also of the target-to-substrate distance on the microstructure, surface morphology, and transport properties of the films.
The surface morphology is analyzed by Atomic Force Microscope (AFM). The corresponding 2D and 3D images of the films grown on $LaAlO_3$ and $SrTiO_3$ substrates are shown in Figure 4.6 a) and b), respectively. The images show a scan area of 2×2 μm^2. The RMS roughness values for a film grown on LAO is 15 $\AA$, while for film grown on STO substrates a RMS value of 26 $\AA$ is obtained.

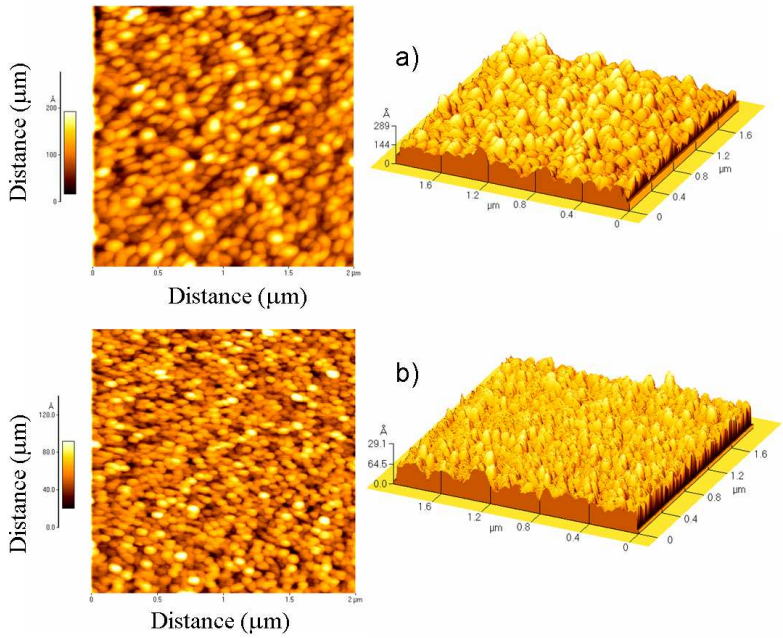

Figure 4.6: (2D) and (3D) AFM images of the LCMO films grown on (a) $LaAlO_3$ and (b) $SrTiO_3$ substrates.

The AFM scans reveal an island- like growth which is related to the epitaxial structure of the thin films. Apparently uniformly distributed round shaped grains of equal size are observed on both substrates. The films grown on the STO substrates exhibit larger grain densities compared to films grown on the LAO substrates. The surface morphology studies suggest an island like growth mode, which is explained by the high instantaneous flux produced during the ablation process which agglomerates in islands when arriving at the substrate. Island- like growth has also been previously reported in the literature for the growth of $La_{0.7}Sr_{0.3}MnO_3$ on different substrates, such as $LaAlO_3$, $SrTiO_3$, $NdGaO_3$ [33]. Smaller RMS values are obtained with the PRCLA technique compared with the literature reports. Zeng et. all [34] have reported a step flow growth of the LCMO films grown on a $NdGaO_3$ substrate due to the very similar lattice

parameter between the film and the substrate.

The films grow epitaxially on LAO and STO substrates. The lattice parameters of the LAO and STO substrates with cubic structure are a= 3.79078 $\AA$ and a= 3.9012 $\AA$, respectively. The lattice mismatch along the interface was found to be -0.028% for the LAO substrates and 0.003% for STO substrates. Tensile strain is therefore induced in the case of STO, while for LAO substrates a compressive strain results. The films thickness is around 190 nm.

The dependence of the bulk resistivity as a function of the temperature for LCMO thin films on LAO and STO as well as the magnetoresistance ratio are shown in Figure 4.7. The measurements were carried out with a Hall effect measurement system and the magnetoresistance ratio was calculated at a magnetic field of 0.5 T.

The magnetoresistance (MR) ratio is defined by relation:

$$MR = \frac{\rho(0) - \rho(H)}{\rho(0)} \times 100, \tag{4.5}$$

where $\rho(0)$ and ρ(H) are the resistivity of the material without and with magnetic field H, respectively.

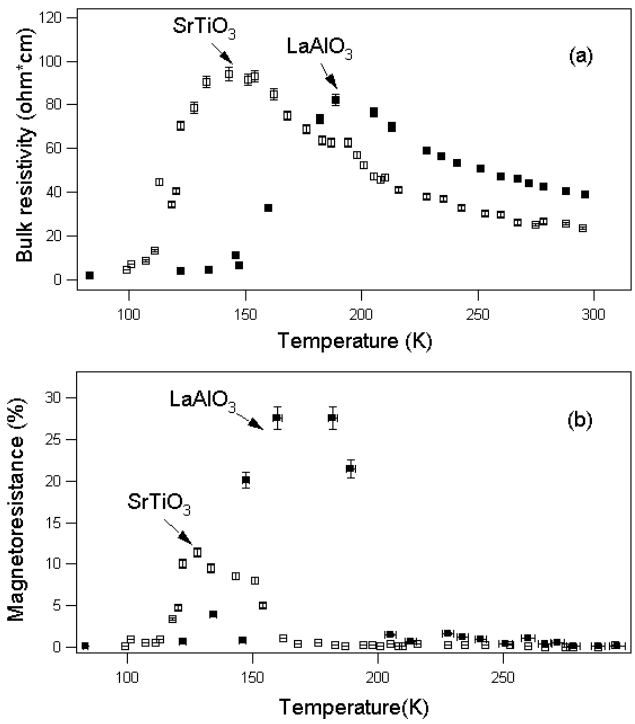

Figure 4.7: Bulk resistivity versus temperature for the films deposited on STO and LAO substrates (a) and the magnetoresistance $\Delta\rho/\rho$ ratio of the LCMO thin films (b).

With decreasing temperature, both films exhibit a transition from the insulator to the metallic conduction state. The films deposited on LAO substrates exhibit a transition temperature of 190 K, while the films grown on LAO exhibit a transition temperature of around 145 K.

The observations of the different transition temperature points are in agreement with previous literature reports, but the difference between the two transition temperatures is larger than previously reported [35]. The difference may be due to the different microstructure of the films. The magnetoresistance curves of the LCMO films grown on LAO and STO exhibit a maximum around the metal- insulator transition point and a magnetoresistance ratio of 15% (at 145 K) for STO and 30% (at 190 K) for LAO are obtained.

4.2.1.3 Thickness dependence on the target- to- substrate distance

Other experimental parameters, such as target- to- substrate distance (D_{T-S}) have also been varied to optimize the properties of the manganite films. The best target- to- substrate distance corresponds to a regime where the kinetic energy of the species arriving at the substrate allows a sufficient surface diffusion for an epitaxial growth.

At a given substrate temperature of 650^0C and a background pressure of 10^{-3} mbar (which are standard conditions for manganites), the crystallinity of the films was investigated as a function of the target to substrate distance (see Figure 4.8). The XRD diffraction patterns indicate that all films grown on STO (001) substrates are epitaxial (not shown here). The calculated FHWM of the (040) diffraction peaks have shown that the best epitaxial growth is obtained when the films are grown at a target to substrate distance between 4 and 5 cm. A broadener diffraction peak was obtained at 3 cm, suggesting that the films have a poor crystalline growth and that they may contain amorphous phases which are not detected by XRD. This can be attributed to the bombardment of the surface of the growing films by a nonthermalized flux of atoms and ions with high kinetic energies.

The RBS analysis show that the stoichiometry of the films does not change as a function of the target to substrate distance (D_{T-S}), and that the as- deposited films are oxygen deficient. The growing films present a slight variation of the composition in depth (around 10 %). A change of the target to substrate distance results also in a change of the films thickness. For 20 000 pulses and a fluence of 5.5 Jcm^2, the films thickness changes from 440 nm to 50 nm, for variations of the target to substrate distance from 3 cm up to 7 cm, respectively (see Figure 4.8).

The temperature dependence of the bulk resistivities of LCMO films deposited on $SrTiO_3$ substrates is shown in Figure 4.9. All films reveal an insulator- like behavior in the measured temperature range, between 100 K and 300 K. The films grown for distances between 3 and 5 cm exhibit a resistivity value at room temperature of 400 $\mu\Omega$cm (close to the bulk material), while the films grown at 7 cm have a bulk resistivity of 100 $\mu\Omega$cm . This suggests that the films grown at a target to substrate distance of 7 cm are strained (due to the film thickness of 50 nm), while for smaller distances (corresponding to thick layers with a thickness from 240 nm to 440 nm) the strain is released over the films thickness. The mismatch between the substrate and the film induces a tensile strain and therefore a compression of the unit cell in the out of

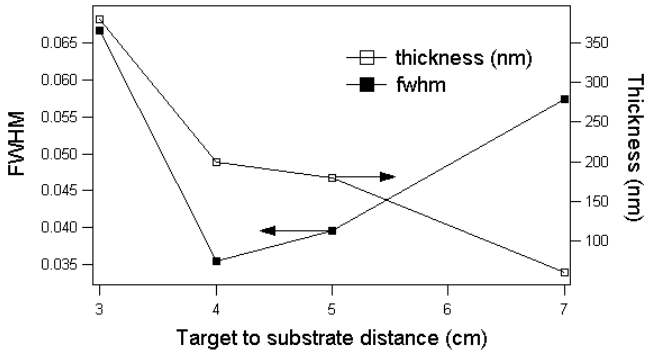

Figure 4.8: FWHM and films thickness as a function of the target to substrate distance.

plane direction. This leads to a reduction of the Mn - O - Mn angle and therefore increase of the electron hoping transfer integral and thus a decrease of the bulk resistivity [32].

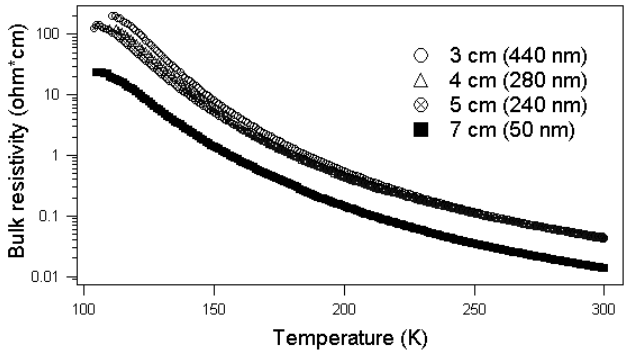

Figure 4.9: Electrical transport curves of the films deposited at different target to substrate distances.

The largest magnetoresistance (MR) values were obtained for films grown at a target to substrate distance of 4 cm (see Figure 4.10 upper graph). The MR ratio exhibits a maximum of ∼83% at the transition temperature (see Figure 4.10 lower graph). Maximum magnetoresistances at a temperature of 120 K of ∼32%, 56 %, 66% and 72% were obtained for films grown at 3 cm (380 nm), 4 cm (200 nm), 6 cm (65 nm) and 7 cm (60 cm), respectively. This suggests that the films grown at distances larger than 6 cm would be under strain influence. Larger CMR values obtained at 4 cm compared to 3 cm most probably are due to better epitaxial growth of the films.

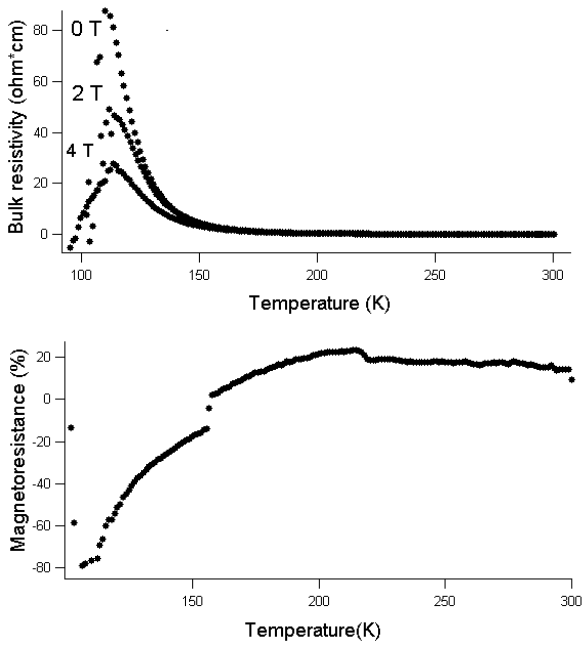

Figure 4.10: Resistivity versus temperature (upper graph) and the corresponding MR ratio (lower graph)of a films deposited 4 cm for a field of 4T.

Our studies reveal that the epitaxial quality of the growing film is also important for obtaining large CMR values. Furthermore, the tensile strain in thin films leads to an increase in the colossal magnetoresistance (CMR) effect.

4.2.2 Microstructure of $La_{0.7}Ca_{0.3}MnO_3$ epitaxial thin films

The strain induced in thin films due to the lattice to substrate mismatch may cause phase separation and inhomogeneities which yield electrical properties that are different from those of bulk materials or thicker films. The importance of lattice distortion on the electrical properties of the materials has been described before in chapter 1.2.1.3. In this chapter we study the growth of the $La_{0.7}Ca_{0.3}MnO_3$ thin films on $SrTiO_3$ substrates using detailed transmission electron microscopy studies (TEM), including high resolution electron imaging (HREM) and selected area electron diffraction (SAED). The measurements were performed by Myriam Aguirre (EMPA, Dübendorf, Switzerland).

The XRD diffraction pattern of the $La_{0.7}Ca_{0.3}MnO_3$ thin films grown on $SrTiO_3$ substrates is shown in Figure 4.11. The main peaks observed in θ- 2θ scans are (002) and/or (110) reflections from the film and (200) reflections from the substrate. The inset in Figure 4.11 shows an enlargement of the mentioned features. The double peaks observed in the diffraction pattern are due to the contributions from both K_{α_1} and K_{α_2} lines of the X- rays source.

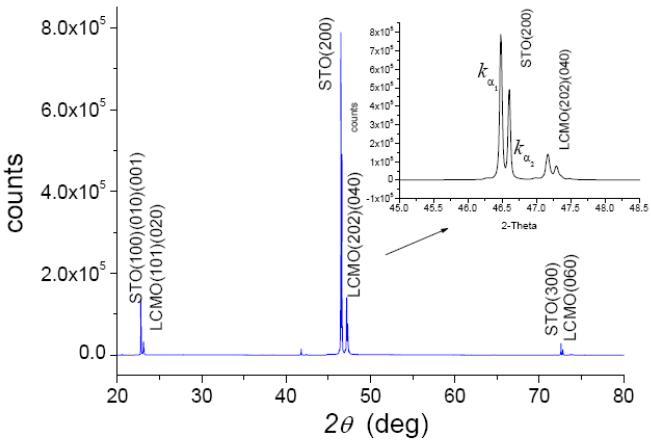

Figure 4.11: XRD patterns of the $La_{0.7}Ca_{0.3}MnO_3$ thin films grown on $SrTiO_3$ substrates.

The cubic Pm3m space group was used for indexing the $SrTiO_3$ substrate, (Code: 01-089-4934), with a = 0.3905 nm, and the orthorhombic space group Pnma was used for indexing the $La_{0.7}Ca_{0.3}MnO_3$ (LCMO) thin film. The X- rays diffraction pattern reveals an orthorhombic distortion, whose lattice parameters are in the following relations with the cubic structure: a$\approx$ $a_p\sqrt{2}$, b$\approx$ $2a_p$, c $\approx$ $a_p\sqrt{(2)}$, $a_p\approx$ 0.4 nm, where a_p is the lattice of the cubic lattice.

The low magnification TEM image of the cross- sectional structure of the LCMO layer grown on the $SrTiO_3$ substrate is shown in Figure 4.12 a. A thickness of the LCMO layer of 200 nm was estimated, which is in agreement with the profilometer measurements. The corresponding diffraction patterns of the substrate (zone axis [100]c assigned to the cubic structure) and film (monoclinic structure with the $P2_{1/c}$ space group) are shown in Figure 4.12 b) and c),

respectively.

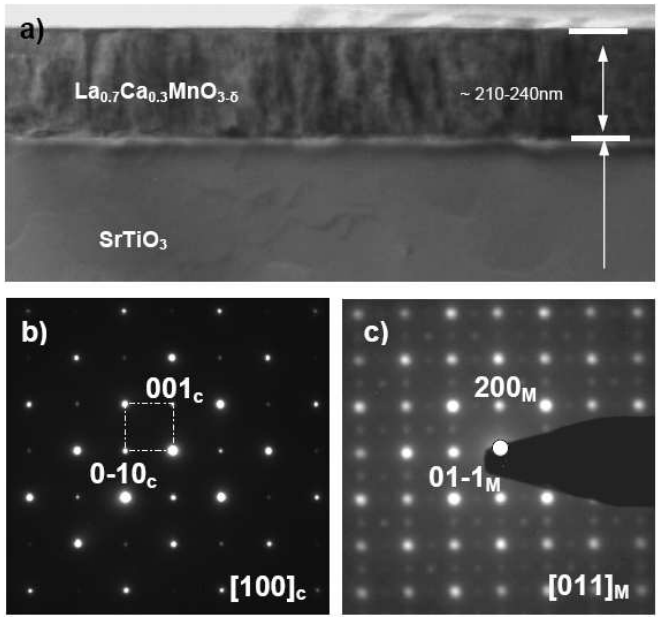

Figure 4.12: Cross section TEM image of LCMO/STO, b) $[100]_c$ STO SAED (selected area electron diffraction) pattern, c) $[011]_M$ LCMO SAED pattern.

Finally, a cross sectional HREM image of both, the LCMO film and $SrTiO_3$, substrate is shown in Figure 4.13. The HREM images of the film confirm the presence of twins in the perovskite layer. Different orientations of the c- axis denote the direction of the individual domains within the layer.

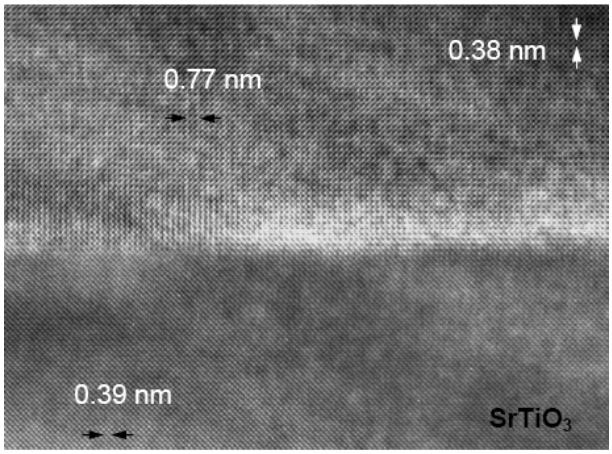

Figure 4.13: High resolution of the LCMO/STO interface in cross section geometry.

It has been suggested that the twin domains are not necessarily formed during the growth, but that the mixed domains can be formed during the cooling of the sample [32]. The formation of the domains is not completely understood at the moment, but a strong correlation between the

strain and domains was found. Previous reports in the literature have shown that for a 5 nm thick $La_{0.7}Ca_{0.3}MnO_3$ layer, only [001] domains are present. When the thickness of the layer is larger than 30 nm, both domains are formed, a consequence of the lattice relaxation. The ratio between the mixed [001]/[110] domains could not be determined, but the majority of the domains are [001].

The LCMO film exhibits an epitaxial growth with "cube-on-cube" on the $SrTiO_3$ substrate. Strain is observed despite the low lattice to substrate mismatch (0.028 %), by misfit dislocations at the interface, which are shown by the dark/white regions.

4.2.3 Effect of annealing on the thin film properties

Oxygen vacancies can affect dramatically the transport properties of the manganite thin films. One approach to improve the oxygen content in the films was the development of Pulsed Reactive Crossed Beam Laser Ablation (PRCLA), where a synchronized reactive gas pulse interacts with the plasma plume close to its origin [8]. Nevertheless, the as deposited films are oxygen deficient, resulting in films with reduced CMR values.

In this context, we have performed a systematic study on the effects of annealing treatments on the properties of the manganite films. The films were subjected to different treatments: i) cooling in O_2 background gas at 50 Pa, followed by an annealing at 400 ^{0}C (where oxygen diffusion is considerable) for 1 h, ii) moderate annealing in O_2 at 600^0 C between 1 and 4 hours, and iii) heavy annealing in an O_2 atmosphere at 900^0 C for 10 hrs at atmospheric pressure. A detailed comparison between the as deposited films and films with various treatments was carried out.

4.2.3.1 Morphological, compositional and electrical characterization

The thin films cooled in vacuum have a dark mirror- like appearance, while the films with high oxygen content appear dark- blue. The investigations were focused on the films grown on STO (100) substrates, which reveal the lowest lattice mismatch between substrate and film. Our studies show that substrates heated in an oxygen atmosphere have a different aspect compared to substrates heated in vacuum. In our experiments, some STO substrates were heated in low oxygen atmosphere (8×10^{-2} Pa) and kept for 1 hour before deposition. Strontium titanate has a cubic structure with a lattice constant of 3.905 $\mathring{A}$. The STO(100) surface can be terminated with a Sr- O plane, or Ti- O plane, and for not specially treated substrates with a mixed surface. The morphology of LCMO films deposited on $SrTiO_3$ depends on whether the substrate was heated or not in an oxygen atmosphere prior deposition.

Figure 4.14 shows AFM scans of LCMO films deposited on STO substrates heated in vacuum and oxygen atmosphere. When the $SrTiO_3$ substrates are heated in vacuum the resulting films have a flat surface, and no clear pattern can be detected. Annealing in an oxygen atmosphere at 700^{0}C results in a terrace like- structure of the $SrTiO_3$ substrate and therefore of the growing films. We can therefore conclude that treatments of the substrates prior deposition has a pronounced influence on the surface morphology of the growing films.

The composition of the LCMO layers determined by RBS/ERDA analysis is shown in Table 4.3. The data reveals as expected an increase of the oxygen content of the films which were cooled in an oxygen atmosphere compared with the films that were cooled in vacuum.

As expected, an increase of the oxygen content in the films results in an improvement of the electrical properties of the films. The plots of the $\ln(\rho/T)$ versus $T^{-1}(K^{-1})$ for the films cooled

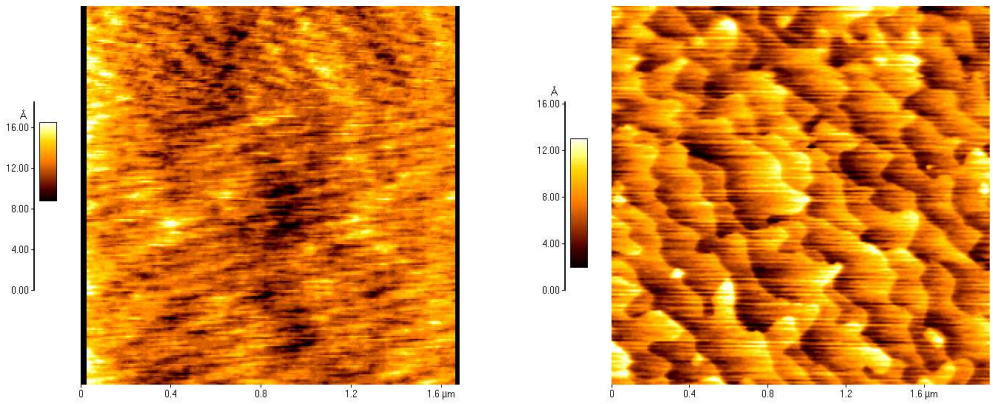

Figure 4.14: AFM images of the LCMO films grown on $SrTiO_3$ substrates which were heated in vacuum (left) and in an oxygen atmosphere (right).

Table 4.3: Elemental composition of the films after post deposition treatments.

Elemental composition	Post deposition treatments
$La_{0.75\pm0.03}Ca_{0.25\pm0.01}Mn_{0.88\pm0.03}O_{2.75\pm0.14}$	Cooling in vacuum
$La_{0.7\pm0.03}Ca_{0.3\pm0.01}Mn_{0.88\pm0.03}O_{2.85\pm0.14}$	Cooling in O_2 atmosphere

in vacuum and oxygen are shown in Figure 4.15. The activation energy, E_a, obtained from the slope of the linear dependence is 135 meV for the as deposited films and 128 meV for the films cooled in an oxygen atmosphere. An increase in the oxygen content results in films with a smaller activation energy and increased CMR values.

When the cooling is performed in the presence of an oxygen atmosphere, the MR value increases considerably. The changes in the presence of an applied magnetic field of the bulk resistivity of the film cooled in oxygen is shown in Figure 4.16. At zero field, the films exhibit an insulating

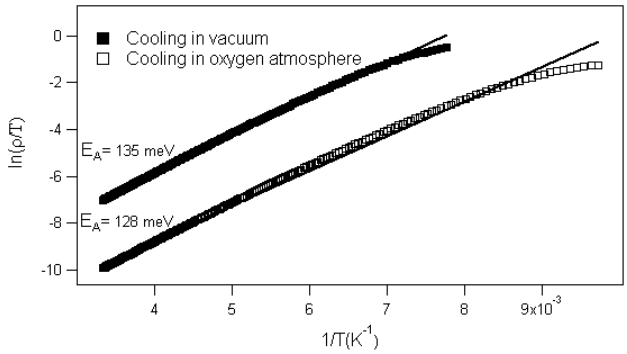

Figure 4.15: Plots of $\ln(\rho/T)$ vs $T^{-1}(K^{-1})$ for the $La_{0.7}Ca_{0.3}MnO_3$ thin films for fast and slow cooling.

behavior, while at 5T a transition from the insulating to the metal state is induced.

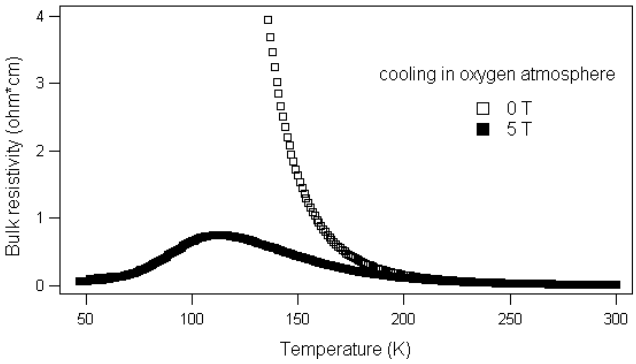

Figure 4.16: Temperature dependence of the resistivity for a film cooled in O_2 atmosphere at applied magnetic fields of 0 and 5 T, respectively.

Heavy annealing (e.g. 900 ^{0}C for 10 h and 1 bar O_2 atmosphere) can improve the transport properties of the thin films even further. Figure 4.17 shows the temperature dependence of the resistivity for the heavily annealed LCMO films at magnetic fields of 0T, 0.5T, 1T, 2T and 5T. The transition temperature point shifts by 4K towards higher temperatures upon annealing. An increase in the oxygen content can induce changes in the transport properties of the films similar to the ones resulting from an externally applied pressure. The external pressure induces a lattice contraction which favors the electron transfer probability in the Mn- Mn network, resulting in a shift of the transition temperature to higher values.
The maximum magnetoresistance versus magnetic field H (plotted in the inset of the Figure 4.17) reaches 90% at a magnetic field of 5 T.

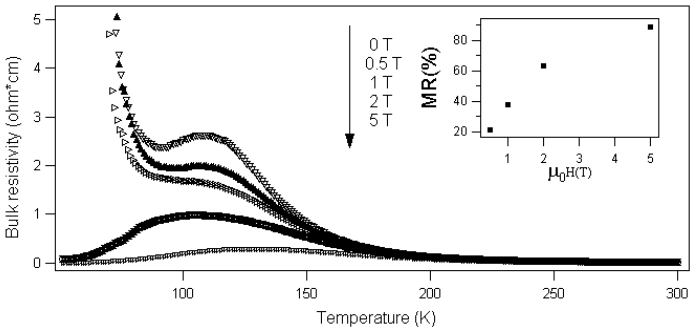

Figure 4.17: Temperature dependence of the bulk resistivity for a LCMO film heavy annealed at the applied fields of 0 and 5 T, respectively. Inset: The maximum MR at different magnetic fields.

4.2.3.2 Study of the Mn oxidation states in $La_{0.7}Ca_{0.3}MnO_3$ films

As reported before, post- deposition annealing is critical for obtaining large magnetoresistance values. The oxygen content influences the oxidation state of the Mn in the unit cell. It is therefore important to establish a correlation between the Mn^{3+}/Mn^{4+} ratio and the oxygen content which determines the electron transfer in the double exchange mechanism.

In this work, photoemission spectroscopy techniques have been utilized to study the electronic configuration of the manganite thin films as a function of the oxygen content. The surface composition of the $La_{0.7}Ca_{0.3}MnO_3$ manganite thin films was analyzed using X- ray photoelectron spectroscopy (XPS), while the bulk electronic configuration was determined by X -ray absorption spectroscopy (XAS). A comparison between the as deposited and O_2 annealed thin films was performed.

The XPS measurements were performed without prior surface cleaning treatments. XANES spectra at the Mn K-edges were collected in the fluorescence mode (for thin films) and in the transmission mode (for reference samples). X- ray photoelectron spectroscopy analysis did not show major differences between the surface composition of the samples annealed for 1 h and the samples annealed for 4 h. Therefore, only the term annealed films (samples with thermal treatment) and as-deposited films (samples without post deposition thermal treatment) is used. The samples thickness, measured with the profilometer, was around 250 nm.

The XPS survey spectra (shown in Figure 4.18) show the main peaks assigned to the film, i.e. La 3d, Mn 2p, O 1s, Ca 2s, Ca 2p, La 4d, Mn 3s, as well as an intense C 1s peaks which is due to the surface contaminations.

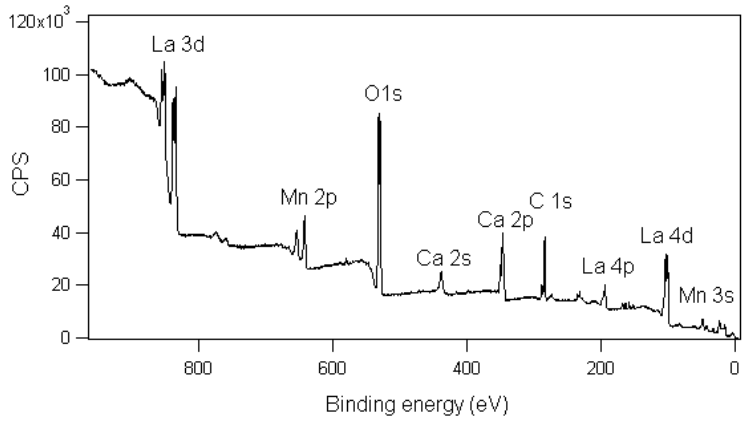

Figure 4.18: Survey spectra of the annealed $La_{0.7}Ca_{0.3}Mn_3$ thin film.

The O1s core levels of the as deposited/ annealed films reveal the presence of two oxygen species at the surface (see Fig. 4.19). The O1s peak at lower binding energy (528.7 eV- 529 eV) can be assigned to the O^{2-} in the perovskite structure [36], while the peak at the higher binding energy (531.5 eV) can be assigned to the surface contaminants. Similar observations have been reported

previously for $La_{0.6}Ca_{0.4}CoO_3$ and have been attributed to $CaCO_3$ species at the surface [37]. The interpretation of the O 1s peaks at the surface of the thin films is difficult due to the surface contaminants. The O 1s peaks, influenced by the stoichiometry of the LCMO perovskite, can be due to the signal from contributions of the Mn- O layer, Ca/La- O containing layer or a mixture of both [38]. A shift of the O1s peaks towards lower binding energy is observed upon annealing.

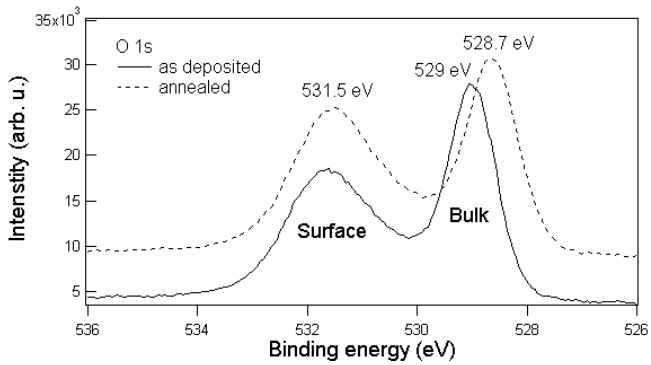

Figure 4.19: O1s core level spectra of the $La_{0.7}Ca_{0.3}Mn_3$ thin films.

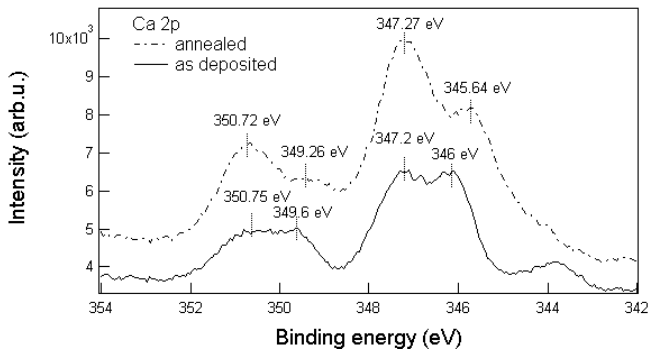

Figure 4.20: The Ca 2p signals of the as deposited and annealed $La_{0.7}Ca_{0.3}MnO_3$ films.

The XPS signal of the Ca 2p core levels, shown in Fig. 4.20, results from two different contributions, e.g. surface contaminants and film. The Ca $2p_{3/2}$ peak has a binding energy of 346 eV (349.26 eV for $Ca2p_{1/2}$) and shifts by 0.36 eV toward lower binding energy after annealing. The binding energy of the Ca 2p component in the $La_{0.7}Ca_{0.3}MnO_3$ thin films is 0.6 eV lower than that observed for $La_{0.9}Ca_{0.1}MnO_3$ [39]. The peak at 347.2 eV can be assigned to the $CaCO_3$ surface species, which is in agreement with the binding energy (BE) of the O1s peak at 531.5 eV.

The XPS spectra of the $La3d_{5/2}$ peaks for the as- deposited and annealed films are shown in Fig. 4.21. The La 3d photoelectron signal exhibits a double splitting, one due to the spin- orbit interaction (component M in Fig. 4.21) and an additional split due to the transfer of an electron from the oxygen ligands to the empty La 4f level (component labelled S in the same figure) [40]. The main peak (M) of the La 3d5/2 core level is located at 833.7 eV and the satellite line (S) is

at 838 eV. The La 3d peaks have a similar behavior as the O species, e.g. shift towards lower binding energy values upon annealing.

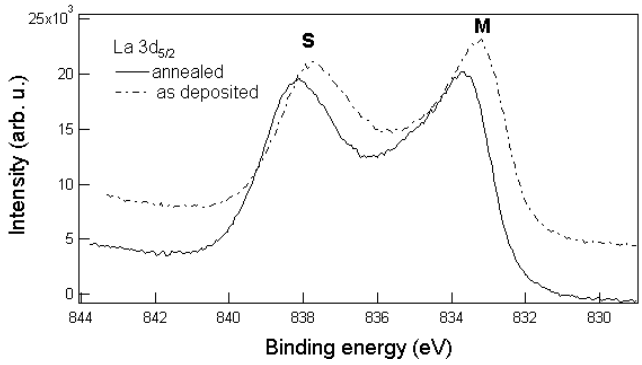

Figure 4.21: The La $3d_{5/2}$ core level of the as-deposited and annealed $La_{0.7}Ca_{0.3}Mn_3$ films.

In manganite thin films, the Mn^{3+}/Mn^{4+} ratio depends strongly on the oxygen content and is determining the CMR values. The average Mn valence in the uppermost atomic layers can be determined from the Mn core levels. The Mn $2p_{3/2}$ peaks are broad (not shown here) and consist of signals from the Mn^{3+} and Mn^{4+} ions. The different oxidation states of Mn exhibit different values, e.g. BE (MnO_2)= 642.6 eV and BE (Mn_2O_3)= 641.9 eV. As the peaks are not well resolved, fitting of the Mn 2p signal cannot be done accurately.
It has been shown that by using the multiplet splitting values of the Mn 3s core level, the Mn average valence can be estimated quantitatively [40]. The Mn 3s core level of the transition metals exhibit an exchange splitting due to the interaction between the 3s hole created by the X- ray photoelectron emission process and 3d electrons of the Mn ion (see Figure 4.22). The parallel or antiparallel alignment results in a splitting of the Mn 3s signal into two peaks. The difference in binding energy of the two peaks is called exchange splitting, and can be accurately used to quantitatively estimate the Mn valence state.

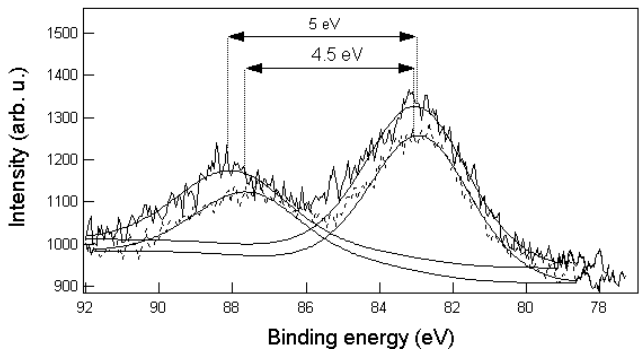

Figure 4.22: Mn 3s multiplet splitting of the as-deposited films (continuous line) and annealed at 0.5 mbar O_2 atmosphere (dash-dot line) fitted with Gaussian functions.

Table 4.4: Multiplet splitting values of the Mn 3s core level.

Material	Stoichiometry (RBS/ERDA)	ΔE_s(eV)
$La_{0.6}Ca_{0.4}MnO_3$	$La_{0.75}Ca_{0.25}Mn_{0.88}O_{2.75}$	5 eV
$La_{0.6}Ca_{0.4}MnO_3$	$La_{0.75}Ca_{0.25}Mn_{0.8}O_{2.85}$	5 eV
MnO_2	-	4.5 eV
Mn_2O_3	-	5.5 eV

The exchange splitting values obtained from the fitting are summarized in Table 4.4. The film stoichiometry determined from RBS/ERDA measurements (included in the same table) reveals a slight increase of the oxygen content upon annealing. The exchange splitting values of the standard samples MnO_2 and Mn_2O_3 are also given. For the as deposited films an exchange splitting value of 5 eV is obtained, indicating that the Mn average valence is in between Mn^{3+} and Mn^{4+}. Annealing in an oxygen atmosphere for 1h results in a decrease of the exchange splitting value to 4.7 eV and after 4 h annealing the splitting decreases to 4.5 eV. This suggests that postdeposition annealing induces a strong oxidation of the manganite surface, and that a layer containing Mn^{4+} species is formed at the surface.

The XPS spectra reveal that all species exhibit the same trend, e.g. shift towards lower binding energy upon annealing, which can be interpreted as an enhancement of the surface metallicity. It is important to determine if the increase in the oxidation state of the Mn species is a surface effect or also occurs in the bulk. For the X- ray absorption measurements on the thin films only the fluorescence detection mode was employed, with an X-ray penetration depth of 8-10 μm, i.e. the complete film and part of the $[(LaAlO_3)O_3(Sr_2AlTaO_6)_{0.7}]$ (100) (LSAT) substrate. For a given film thickness, this technique probes therefore 250 nm of the bulk electronic structure.

Figure 4.23 shows the Mn K edge spectra of $LaMnO_3$ and $SrMnO_3$ reference compounds in comparison with those of the annealed $La_{0.7}Ca_{0.3}MnO_3$ (red line) and as-deposited (blue line) thin films. After normalization, an energy shift of the main edge can be observed (as indicated by the arrows in Fig. 4.23 which shows the peak position of the first derivative for the corresponding spectrum).

The energy shift towards higher energy reveals that the Mn oxidation state changes from +3 in the as-deposited films to +3.4 in the annealed films. A similar energy shift was obtained previously on powder precipitates upon annealing in O_2 atmosphere and it is consistent with Mn^{4+} (t_{2g}^3) configuration sites [41]. A pre-edge feature around 6540 eV, located approximately 15- 20 eV below the main K-edge crest of manganese can be observed in Fig. 4.23. The pre-edge feature is related to electronic transitions from the 1s core levels to the empty 3d levels which are hybridized with 4p levels through the Mn ligands (thus probing the density of the lowest unoccupied states). The discrepancies in energy position and relative areas between the pre-

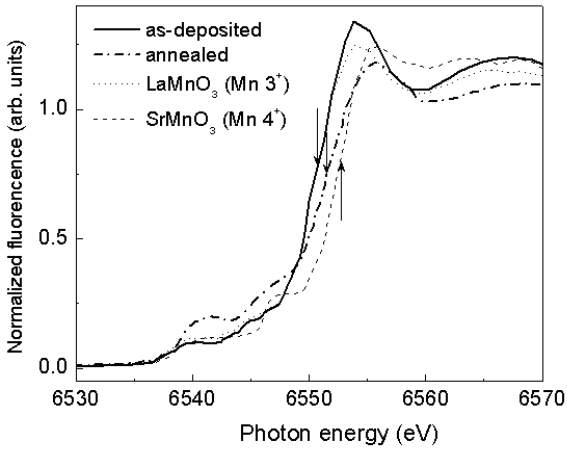

Figure 4.23: Normalized Mn-K main edges of $LaMnO_3$ (Mn^{3+})(thin dotted line) and $SrMnO_3$ (Mn^{4+}) (thin dashed line) reference compounds versus the annealed $La_{0.7}Ca_{0.3}MnO_3$(dash dot line) and as-deposited (continuous line) thin films. The arrows indicate the positions of the main edges.

edges of the two films can be attributed to variations in the effective number of 3d electrons in the excited-state configurations. The pre- edge area enhancement after O_2 annealing is due to an increased hybridization between the Mn d/p bands above the Fermi energy, which is supported by the increased fraction of Mn^{4+} (t_{2g}^3) states.

In conclusion, using two complementary electron spectroscopy techniques, surface changes in oxidation states (XPS) can be separated form the bulk contributions (XAS). After O_2 annealing, the films surface has changed, containing mostly Mn^{4+} ions and probably a higher oxygen content, while in bulk the presence of a mixture of Mn^{3+} and Mn^{4+} valence states can be observed. An increase in the Mn^{4+} carriers leads to a increase in the carrier concentration and hence decrease of the bulk resistivity. This favors the hopping of electrons in the Mn^{3+}-O^{2-}-Mn^{4+} network and increases of magnetoresistance.

4.3 Fe doped $La_{0.7}Ca_{0.3}Mn_{1-x}Fe_xO_3$ (x=0.2) thin films

4.3.1 Motivation

In the previous sections we have been reported how PRCLA has been applied to grow high-quality LCMO thin films on single crystalline substrates. Large magnetoresistance values could be obtained by cooling/ annealing in oxygen atmosphere. The conduction mechanism in hole-doped systems is mainly determined by the double exchange interaction. The double exchange (DE) mechanism has often been discussed in the context of properties for CMR materials. Divalent ion doping of the perovskite structure induces the formation of the Mn^{4+} ions which enables the e_g electron of a Mn^{3+} ion to hop to the neighboring Mn^{4+} ion via the DE, which mediates ferromagnetism and conduction. The physical properties of the materials are also sensitive to lattice changes induced by doping in the La site. Any deviation from the ideal cubic perovskite structure can lead to either a reduction in the Mn - O - Mn bond angle from 180^0 or a change in the bond length. Both changes affect as well the DE interaction, but only a few studies have been carried out for LCMO doping at the Mn sites.

A secondary mechanism suggested for a qualitative explanation of the CMR effect consists in a strong electron- phonon coupling arising from a Jahn- Teller splitting of the Mn 3d levels [42]. The distortion of the oxygen octahedra, determined by the presence of the Mn^{3+} Jahn-Teller ions in the perovskite structure, leads to a localization of the carriers in the form of small polarons in the paramagnetic phase. Ahn et al. [43] have shown that Fe doping (<20%) on the Mn site in the ferromagnetic x= 0.37 and the antiferromagnetic x= 0.53 phases of the $La_{1-x}Ca_xMnO_3$ powders leads to a suppression of the ferromagnetism and conduction.

Our aim is to probe the role of the Mn^{3+} Jahn- Teller ions on the CMR properties of the manganites, by replacing some of the Mn ions by Fe ions (20%) and to prepare the first single crystalline materials in the form of thin films, where Mn has been partially exchanged.

4.3.2 Characterization of the $La_{0.7}Ca_{0.3}Mn_{0.8}Fe_{0.2}O_3$ the thin films

An AFM scan of a $La_{0.7}Ca_{0.3}Mn_{0.8}Fe_{0.2}O_3$ (LCMFO) films grown by PRCLA using a N_2O gas pulse are shown in Figure 4.24. An RMS roughness of 9 $\AA$ was measured for a scan area of 2× 2μm^2. The surface topography of the films consists of small grains with an average size of ∼ 50 nm, suggesting an island growth mode on the $LaAlO_3$ (LAO) substrate. As expected, the surface morphology of the LCMFO films is similar to the one of the LCMO films.

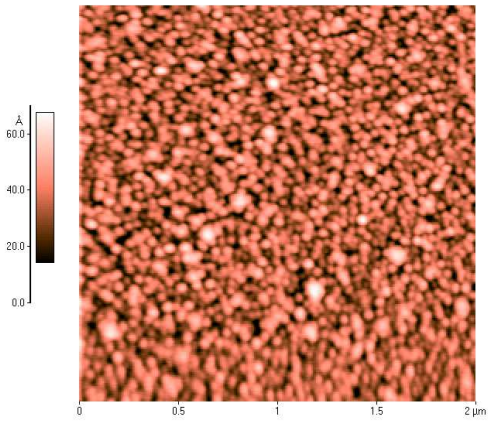

Figure 4.24: Surface morphology of the LCMFO/LAO film deposited with N_2O gas pulse.

The x-ray θ-2θ scans show that the Fe doped LCMO thin films on LAO substrates are single crystalline (see Figure 4.25). The presence of the reflections from a pseudocubic unit cell (corresponding to the Kα1, Kα2 and Kβ) of the film and substrate reveal a high quality epitaxial growth. The lattice parameters of the pseudocubic unit cell are described by the relations a_{ps}≈a ≈b≈ c. The lattice parameter of the LCMFO films determined form the XRD data is 3.890 Å, which is close to the lattice parameters of the undoped LCMO films, e.g. 3.897 Å. This suggests that the substitution of Fe in the Mn sites does not induce significant structural changes in the perovskite structure. Our observations are in agreement with previous literature reports [44] and can be explained by their similar ionic radii, of Fe^{3+}= 0.645 $\AA$ and Mn^{3+}= 0.64 $\AA$ (considering an average valence 3+ of Fe).

In order to determine the main valence state of Fe and its magnetic environment, Mössbauer spectroscopy measurements were carried for the Fe doped films with a thickness of 300 nm. The measurements were performed by Peter Schaaf, Zweites Physikalisches Institut, Universität Göttingen, Germany.

The results are summarized in Table 4.5 where the term "surface" refers to a probing depth of the film of 150 nm, while the term bulk corresponds to a probing depth larger than 150 nm. The Mössbauer measurements reveal the presence of both Fe^{2+} and Fe^{3+} valence states at

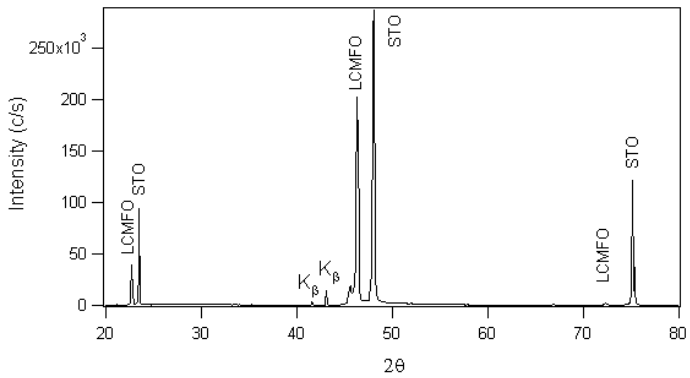

Figure 4.25: XRD scans of the LCMFO films prepared on $LaAlO_3$(100) substrate

the "surface", while in the bulk only Fe^{3+} is detected (4% is within the error bars). However, Fe is found mainly in an oxidation state of 3+. The low amount of Fe doping (20%) did not allow an accurate fitting of the Mössbauer spectra. It could therefore not be determined if Fe is coupled ferromagnetically or antiferromagnetically to the Mn- O lattice. Fe was found in an amount of 43% (or 35% in bulk) in a phase whose magnetic character could not be determined (ferromagnetic or antiferromagnetic phase). Intensive Mössbauer investigations for larger Fe doping have shown that the magnetic moments of Fe^{3+} are coupled antiferromagnetically to the ferromagnetic Mn–O lattice [45].

Table 4.5: Mössbauer results on $La_{0.7}Ca_{0.3}Mn_{0.8}Fe_{0.2}O_3$ films.

	Probing depth	Fe^{3+}[%]	Fe^{2+}[%]	Phase (*)[%]
$La_{0.7}Ca_{0.3}Mn_{0.8}Fe_{0.2}O_3$	"Surface"(150 nm)	32	25	43
on $LaAlO_3$	"Bulk"(>150 nm)	61	4	35

(*) Fe can be found in a ferromagnetic or antiferromagnetic phase.

The elemental composition of the $La_{0.7}Ca_{0.3}Mn_{0.8}Fe_{0.2}O_3$ films was investigated using three complementary methods, i.e. RBS, ERDA and PIXE. The RBS method can provide an accurate information about the La, Ca, Mn and Fe content with an error of 3 %, while ERDA is used to determine the oxygen content with the same accuracy. The elemental composition of the LCMO films and Fe doped LCMO films, obtained from RBS/ERDA analysis, is summarized in Table 4.6. Comparing the stoichiometry of the undoped and Fe- doped LCMO samples reveals the same oxygen content in the films (see Table 4.6). We can conclude that the Fe ion substitutes the Mn in the perovskite structure without affecting the oxygen content. Furthermore, we observe high oxygen deficiencies in the growing films for both LCMO and Fe doped LCMO films.

A quantitative separation of Mn from Fe was not possible due to the low mass resolution of RBS. The PIXE technique was therefore employed to determine the Fe content in the films. The Photon Induced X- ray Emission (PIXE) spectra of the films are shown in Figure 4.26. The

Table 4.6: Stoichiometry evaluation of the $La_{0.7}Ca_{0.3}Mn_{0.8}Fe_{0.2}O_3$ thin films.

Target	Film stoichiometry (RBS/ERDA)
$La_{0.6}Ca_{0.4}MnO_3$	$La_{0.72}Ca_{0.28}Mn_{0.85}O_{2.5}$
$La_{0.7}Ca_{0.3}Mn_{0.8}Fe_{0.2}O_3$	$La_{0.6}Ca_{0.25}Mn_{0.8}Fe_{0.2}O_{2.5}$

spectra reveal the presence of a Fe K_β peak assigned to the $La_{0.7}Ca_{0.3}Mn_{0.8}Fe_{0.2}O_3$ films (case b), while in the case of the $La_{0.7}Ca_{0.3}MnO_3$ films no peak is observed. The estimated Fe/Mn ratio from the K_β (%) peak area is 25 % (±3%) for LCMFO films and is smaller than 1.4 % (which is in the measurements errors) for the undoped samples. The PIXE analysis indicates that a congruent transfer of Fe (20 ±3%) is achieved by PRCLA.

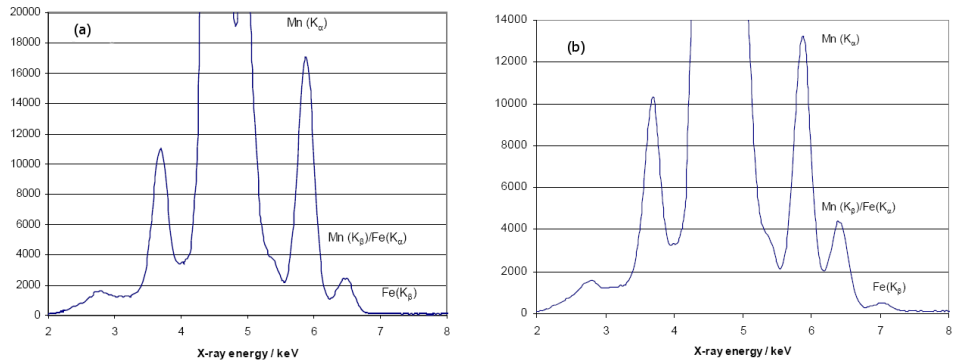

Figure 4.26: PIXE spectra of the LCMO films (a) and Fe doped LCMO films (b).

Electrical characterization studies were performed on Fe doped LCMO samples to study the influence of Fe on the transport properties of the LCMO films, especially on the CMR effect.
Fe doping in the Mn sites induces several changes on the transport properties:
i) With Fe doping, the bulk resistivity of the manganite thin films increases dramatically. The ratio of bulk resistivity of x= 0.2 with respect to x= 0 is:

$$\frac{\rho(x=0.2)}{\rho(x=0)} \sim 9 \tag{4.6}$$

Fe doping induces therefore an increase by almost one order of magnitude (at room temperature) of the bulk resistivity.
ii) The activation energy increases. As discussed before, the activation energy can be determined from the polaron conduction equation. A fitting of ln(ρ/T) vs 1000/T(K^{-1}) for the $La_{0.7}Ca_{0.3}Mn_{1-x}Fe_xO_3$ samples with x=0 and 0.2 is shown in Figure 4.27. The activation energy obtained from the linear fits is inserted in the same figure. The Fe doping in the LCMO compounds induces an increase of the activation energy from 100 meV for LCMO samples to 154 meV for the LCMFO samples. The increase in the activation energy suggests that the hopping mechanism is reduced.

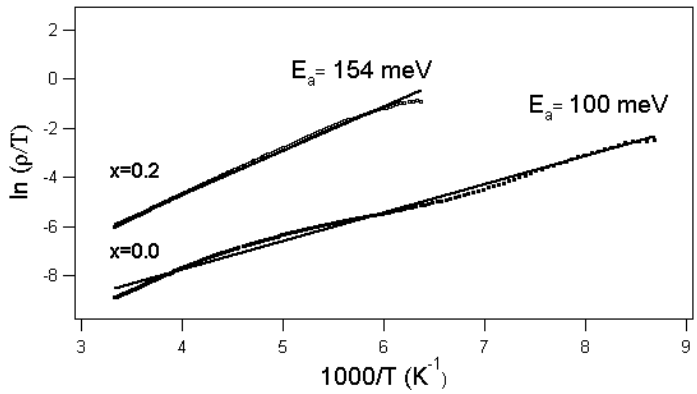

Figure 4.27: Plots of ln(ρ/T) vs 1000/T(K^{-1}) for $La_{0.7}Ca_{0.3}Mn_{1-x}Fe_xO_3$ samples with x=0 and 0.2.

iii) The CMR effect is considerable reduced. The bulk resistivity dependence on the temperature at 0 T and 5 T of the Fe- LCMO sample is shown in Figure 4.28. The films exhibit an insulator-metal transition at a transition temperature of T_p= 136 K. No change in the bulk resistivity is observed at 5T, suggesting the absence of CMR effect after Fe doping.

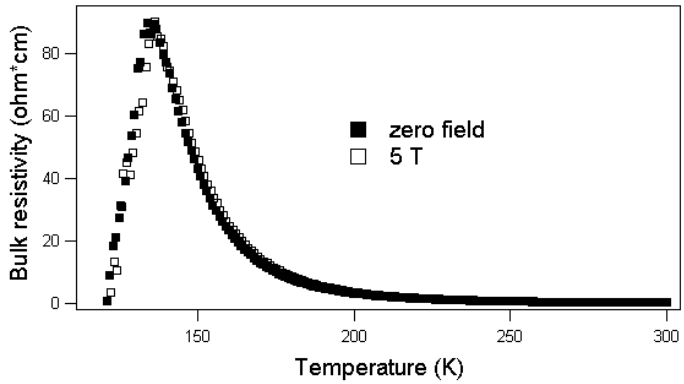

Figure 4.28: Resistivity of the $La_{0.7}Ca_{0.3}Mn_{0.8}Fe_{0.2}O_3$ films with and without magnetic field as a function of temperature.

Fe is found invariably in the valence state +3 (mainly), and a direct substitution of Mn^{3+} by Fe $^{3+}$ is most probable. Each Fe^{3+} ion that substitutes an Mn^{3+} ion will perturb the long order ferromagnetic interaction, weakening therefore the double exchange mechanism, and as a consequence reducing the CMR effect. It is therefore important to study the electronic configuration of the Mn and Fe system and correlate the results with the finding on the transport properties of the films.

4.3.3 Electronic properties of the Fe (20%) doped $La_{0.7}Ca_{0.3}MnO_3$ thin films

The motivation behind this work is to study the Mn- d configuration changes in the $La_{0.7}Ca_{0.3}Mn_{1-x}Fe_xO_3$ (x=0, 0.2) compound. Near edge and X-ray absorption spectroscopy measurements were used to probe the configuration of Mn and Fe, as well as changes in the chemical state of the elements.

A comparison between the Mn K edge spectra of the $La_{0.7}Ca_{0.3}Mn_{1-x}Fe_xO_3$ films, with (x=0, 0.2), is given in Figure 4.29. No change in the main K edge position is observed in $La_{0.7}Ca_{0.3}Mn_{1-x}Fe_xO_3$ (x=0, 0.2), suggesting that the predominant Mn valence does not change upon Fe doping. The main difference between the annealed and not annealed films consists in the intensity drop of the main feature at the Mn K-edge. The feature can be associated with disorder induced in the perovskite lattice due to the high oxygen deficiencies and different valence states of Fe and Mn.

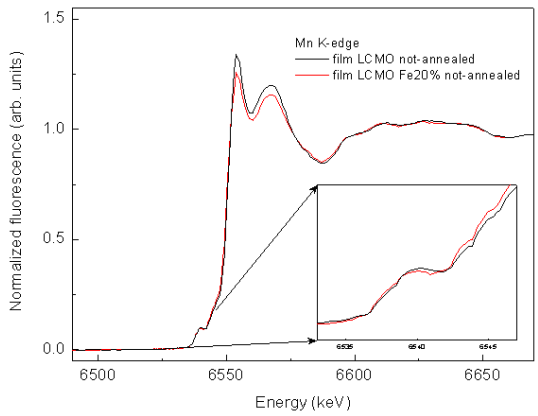

Figure 4.29: Normalized Mn-K main edges of the as deposited $La_{0.7}Ca_{0.3}Mn_{1-x}Fe_xO_3$ (x=0, 0.2) films grown on $[(LaAlO_3)O_3(Sr_2AlTaO_6)_{0.7}]$ (100) (LSAT) substrates. The inset shows the Mn-K pre edges of the same films.

The Mn K-edge spectra of the annealed $La_{0.7}Ca_{0.3}Mn_{1-x}Fe_xO_3$ (x=0, 0.2) films is shown in Figure 4.30.

After annealing, the main line of the LCMO and Fe doped LCMO reveals the same intensity, but a change in the pre- edge features is observed. The pre- edge region is related with transitions into final d- states, e.g. electronic transitions from 1s into empty d states or hybridized d/p states [19]. The Mn pre-edge features reveal an increase in the a_1 feature intensity relative to the a_2 feature. Simple crystal field theory suggests an association of the first feature (a_1) with the e_g majority spin states and of the feature at higher energy (a_2) with t_{2g} and e_g spin states. The increase in the a_1 feature with respect to the a_2 feature reveals an increased localization of

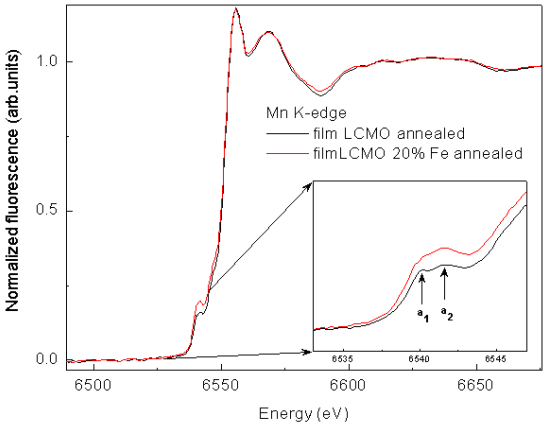

Figure 4.30: Normalized Mn-K main edges of $La_{0.7}Ca_{0.3}Mn_{1-x}Fe_xO_3$ (x=0, 0.2) not-annealed thin films grown on LSAT substrates. Inset: enlargement of the Mn-K pre edge region.

the Mn 3d- orbitals after Fe substitution for the annealed films.

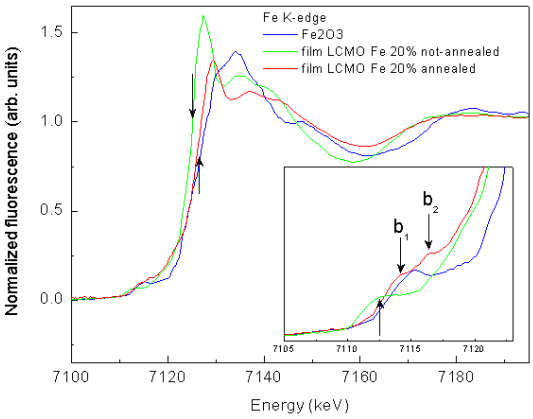

Figure 4.31: Normalized Fe-K edges of Fe_2O_3 (Fe^{3+}) versus those of the $La_{0.7}Ca_{0.3}Mn_{1-x}Fe_xO_3$ (x=0, 0.2) annealed and not-annealed films. The arrows indicate the positions of the edges. The inset shows an enlargement of the Fe-K pre edges features.

The lattice disorder observed in the as deposited films can be related to the high oxygen deficiencies. The Fe K- edge region was probed using the Near Edge X- ray Absorption Spectroscopy (NEXAS) technique in order to determine the Fe valence state in the bulk and the density of the unoccupied states. For comparison, a Fe_2O_3 powder (Fe^{3+}) reference compound is shown together with the Fe K - edge spectra of the annealed and not-annealed LCMFO films in Figure 4.31. The position of the inflection point, indicated by an arrow was determined as the point where the slope is maximum. The edge region indicates that the average valence of Fe is lower than 3+,which is in agreement with the Mössbauer and XPS measurements. The bimodal distribution of the pre-edge (features b_1 and b_2) in the annealed films compared with the not-annealed

films gives some evidence of Fe- site localization effects, but it is not possible at the moment to associate these features with specific d-states.

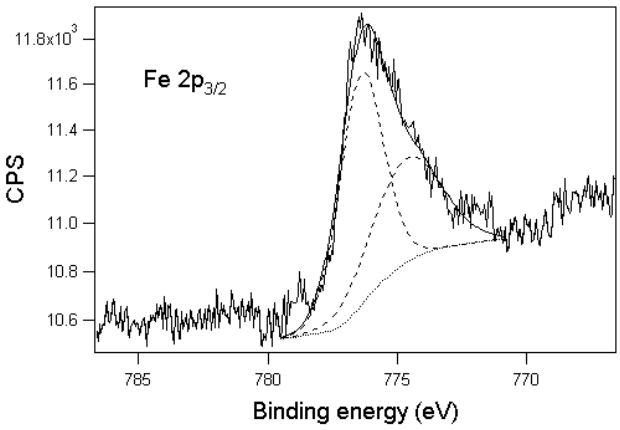

Figure 4.32: Fe $2p_{3/2}$ XPS peaks for the as deposited $La_{0.7}Ca_{0.3}Mn_{0.8}Fe_{0.2}O_3$ films. The fitting curves inserted in the graph reveal the presence of Fe^{2+} and Fe^{3+} valence states.

Mössbauer measurements reveal that Fe can have both 2+ and 3+ valence states. Furthermore, XPS investigations have shown that Fe $2p_{3/2}$ peaks can be fitted with two functions, as shown in Figure 4.32, which shows that the Fe $2p_{3/2}$ XPS spectra consists of two peaks that can be assigned to the 2+ and 3+ valence states.

As mentioned before, we observed an increase of the polaron activation energy and increase of the Mn ion orbitals localization upon Fe doping in the LCMO films. Our results have also to be related to the literature data. Calculations of the electronic band in Fe doped compounds have shown that the top of the Fe e_g band is almost located at the bottom of the Mn e_g band, just with an overlap of less than 3%. The Fe ions do not favor the hopping of the carriers towards Mn $^{4+}$ ions, acting therefore as trap centers [43].

In conclusion, the substitution of the Mn Jahn- Teller ions with Fe non- Jahn Teller ions suppress of the double exchange interaction and reduces therefore the CMR ratio, suggesting the importance of the Mn^{3+} Jahn- Teller ions on the magnetoresistance effect.

4.4 Conclusions

Part I

The double exchange interaction is the main mechanism responsible for the CMR effect, where an exchange of electrons occurs between neighboring Mn centers bridged by oxygen (Mn^{3+}- O^{2-}- Mn^{4+}. High oxygen deficiencies in the as deposited films lead to a dramatic reduction of the CMR ratio. An increase in the oxygen content, possible by annealing treatments and/ or controlled cooling, has mainly two consequences:

i) A change of the Mn^{3+}/Mn^{3+} ratio, a higher oxygen content which induces a higher amount of Mn^{4+} ions. More Mn^{3+}- O^{2-}- Mn^{4+} networks are available in the perovskite lattice, which favors conduction and ferromagnetism. As a result, the CMR ratio increases considerable.

ii) The increase in the oxygen content results in a contraction of the perovskite lattice similar to an applied external pressure. The electron transfer probability is therefore favored and this leads to an increase of the transition temperature and a decrease of the bulk resistivity.

Part II

In the Fe- doped LCMO samples a direct substitution of Mn^{3+} by Fe $^{3+}$ occurs. The as deposited films contain Fe^{2+} and Fe^{3+} ions randomly distributed in the perovskite structure inducing therefore disorder. Upon annealing, Fe is found invariably in the valence state of 3+.

The effects of Fe doping can be summarized in the following way:

i) The Mn 3d orbital localize upon Fe substitution in Mn sites (according to the XAS measurement), suggesting that the Fe ions acts as trapping centers which block the conduction of e_g electrons.

ii) The activation energy of the polarons and the bulk resistivity increases. This is probably due to the non availability of the Mn^{3+} Jahn- Teller ions for the conduction mechanism.

iii) The double exchange interaction is partially suppressed and the CMR effect is considerable reduced.

iv) Each Fe^{3+} ion that substitutes an Mn^{3+} ion will perturb the long order ferromagnetic interaction. The type of interaction between Mn^{4+} ions and Fe^{3+}, i.e. in the Fe^{3+}- O^{2-}- Mn^{4+} structural unit, could not be determined from the Mössbauer measurements. Previous literature studies (for higher Fe doping) have shown that the mentioned network has an antiferromagnetic character. Fe doping induces therefore the incorporation of antiferromagnetic phases in the ferromagnetic network, but the magnetic character has to be studied further.

Chapter 5

Characterization of the Plume Induced by Laser Ablation of a Manganite Target by mass spectrometry

[1]

This chapter includes a study on the plume produced by laser ablation of a $La_{0.6}Ca_{0.4}MnO_3$ target in vacuum and in the presence of a reactive gas pulse of N_2O. The ablation yield and kinetic energy of the plume species were measured using a kinetic energy analyzer coupled with a quadrupole mass spectrometer. The plume composition and angular distribution of the ablated species was firstly investigated in vacuum, at a pressure lower than 10^{-7} mbar. The influence of the reactive gas pulse crossing the ablation plume on the composition and formation of diatomic species will be discussed in detail.

[1]Part of the data included in this chapter has resulted in the following publication:

S. Canulescu, Th. Lippert, A. Wokaun, Mass and kinetic energy distribution of the species generated by laser ablation of $La_{0.6}Ca_{0.4}MnO_3$, Applied Physics A: Materials Science & Processing.

5.1 Studies of the plume in vacuum

5.1.1 Overview

Laser ablation is often used for deposition of materials with a complex stoichiometry, such as manganite materials [46], glass materials [47], etc. In particular, Pulsed Reactive Crossed Beam Laser Ablation (PRCLA) was successful employed for the deposition of multilayered structure with periodicity (A–B–C–B), such as $TiC_xN_{1-x}/VC_xN_{1-x}/ZrC_xN_{1-x}/\ VC_xN_{1-x})_n$ [48]. Willmott et al. have shown that using PRCLA growth of thin films in a wide composition range can be achieved by fast translation of a target rod containing two or more different compositional regions [49].

It is well known that particles with high kinetic energy may be generated during the laser ablation process. The energy distribution of the ablated species is mainly affected in PRCLA by the secondary interactions close to the target. The energetic particles arriving at the substrate have enough energy together with energy from the heated substrate to allow epitaxial film growth. When the kinetic energy of the species is too high, then detrimental effects are observed, especially re- sputtering of the growing films [50].

Measurements of the kinetic energy distribution of the ablated species arriving at the substrate is therefore a key parameter for the growth process. A proper control of films growth requires knowledge of the plume composition, angular distribution, as well as the energy distribution of the ablated species.

In this section, we report on a study of the plasma generated by laser ablation in vacuum from a $La_{0.6}Ca_{0.4}MnO_3$ target. A kinetic energy analyzer coupled with a quadrupole mass spectrometer allows measurements of the kinetic energy distribution of the ablated species.

5.1.2 Experimental setup

The experiments were carried out using a quadrupole mass spectrometer from Hiden Analytical (EQP 500) with a mass ranging from 1 to 500 amu. The kinetic energy of the species was measured using an electrostatic energy analyzer whose settings were tuned to allow a kinetic energy (KE) analysis of the particles with the selected mass to charge ratio. The differential pumping system of the EQP maintains a pressure in the analysis chamber of 5×10^{-8} mbar, while the pressure in the ablation chamber was set in a range from 1×10^{-7} mbar to 10^{-3} mbar. The neutral species entering the cage section of the mass spectrometer were ionized using a 70 eV dual filament electron impact ionization source, while the positive species were detected with the ionizer switched off. During the neutral detection, the EQP extractor was set to a voltage

of 50 V, in order to repel all ions with kinetic energies higher than 50 eV [2].
During the measurements, the nozzle of the mass spectrometer was located at a distance of 10 cm from the target.

5.1.3 Plume composition in vacuum: wavelength dependence

The laser wavelength is a key parameter in the ablation process. For a given material, the penetration depth depends directly on the laser wavelength. The irradiation wavelength affects also the size and density of particulates in the growing films. Studies on the growth of high- T_c superconductors have shown that smoother surfaces are obtained when UV lasers are employed compared to IR lasers [51]. This can be associated with the stronger absorption of the UV light by the photofragments compared to the IR light, and it depends on the laser energy per pulse. The absorption processes of UV photons induces a higher plume temperature and fragmentation into smaller fragments, including ions and neutrals. The resulting films have smaller particulates and therefore a smoother surface.
In this section, we study the influence of the different UV photon energies ranging from 6.7 eV (193 nm, ArF excimer laser) to 4.65 eV (266 nm, Nd- YAG laser) and 4.03 eV (308 nm, XeCl excimer laser) on the plume composition. The dependence of the mass distribution of the ablated species on the laser wavelength will be discussed.
The mass distributions of the ionic and neutral species generated by laser ablation of the La - Ca - Mn - O target using three different wavelengths. i.e. 193 nm, 266 nm and 308 nm are shown in Figure 5.1. The laser fluence was set at 1 Jcm^{-2} . The ablation plume of the manganite target consists of ionic and neutral atoms, such as La, Ca, Mn, CaO, LaO, as well as ionic polyatomic species, such as LaMnO and Mn_2 (for 266 nm laser irradiation). The polyatomic species most probably originate from secondary interactions between the plume species. Doubly charged species, La^{++} and Ca^{++}, are present in small amounts in the mass spectra recorded for 193 nm and 266 nm irradiation.
The mass spectra of the plume species generated by laser ablation at 266 nm consists of a large amount of positive oxygen ions and polyatomic species, as shown Figure 5.1. The polyatomic species are probably formed by secondary interactions due to the presence of a large amount of positively charged oxygen ions in the ablation plume.
Comparing the relative intensity of the ablation yield at different wavelengths shows that LaO is the second most abundant species. One question that arises is the origin of the LaO diatomic species in the ablation plume. One possible source is i) a direct ejection of the diatomic species from the target, and ii) the formation of the diatomic species in the gas phase.

[2]The value was determined experimentally, depending on the energy distribution of the ions. For the given fluence, the energy of the ions extends up to 40- 50 eV.

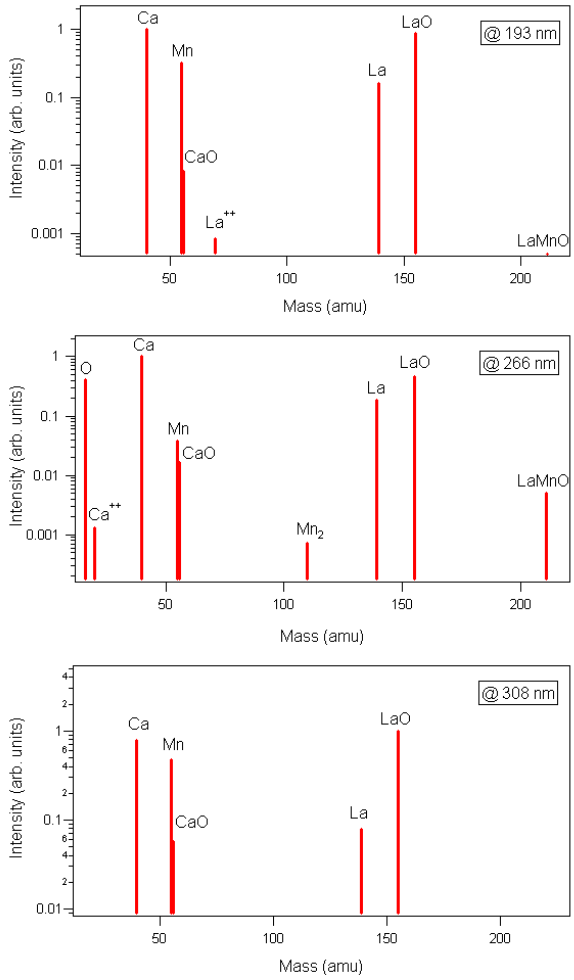

Figure 5.1: The mass distribution of the ionic species generated by 193 nm, 266 nm and 308 nm laser ablation of a LCMO target, using a laser fluence of 1 Jcm^{-2}.

The first mechanism could explain why only one diatomic species, i.e. LaO, is detected in a large amount for all wavelengths. LaO has the highest dissociation energy of the three diatomic species (8.2 eV), followed by MnO (4.13 eV) and CaO (4.11 eV). The photon energies corresponding to the irradiation at 308 nm (4.02 eV) is smaller than the dissociation energy of MnO, thus decomposition would be less favorable. However, decreasing the photon energy no MnO species are observed. This suggests that the detection of the diatomic species in the plume cannot be completely related to the photon energy.

The large amount of LaO species in the mass spectra may be related to the high bond stability of the LaO molecules and large oxidation potential. The oxidation of the plume species in the gas phase may play as well an important role. It has been suggested that oxidation of the La and Ca atoms occurs readily, while the oxidation of Mn atoms is less favorable [52]. However, the enthalpy of formation of the diatomic species is generally given for standard thermodynamical conditions, which are very different from the plasma conditions. It is therefore difficult to

quantitatively estimate the oxidation of the La, Ca, Mn species in gas phase (plasma) based on the enthalpy values, and a more complex model is required.
A comparison between the ablation yield induced by laser irradiation at different laser wavelengths is summarized in Table 5.1. The data reveal that the ionic yield generated at 193 nm is larger compared to 266 nm and 308 nm irradiation. This suggests that for larger photon energies, more ionic species are produced. The first ionization potential of the target components: La, Ca, Mn are at 5.58 eV, 6.13 eV and 7.43 eV, respectively. The ArF laser photons (6.7 eV) provide therefore enough energy to ionize most of the plume species with a single photon, resulting in a higher yield of ions compared to 266 nm and 308 nm irradiation, as summarized in Table 5.1.

Table 5.1: The ion to neutral ratios for different irradiation wavelengths, e.g. 193 nm, 266 nm and 308 nm, using a laser fluence of 1 Jcm^{-2}.

Species	193 nm (6.7 eV)	266 nm (4.7 eV)	308 nm (4.02 eV)
La^+/La	6.9	0. 8	0.9
Ca^+/Ca	14.9	10.4	8.7
Mn^+/Mn	0.5	0.1	1.8
LaO^+/LaO	3.5	2.7	1.8

In the case of Mn, the M^+/M ratio increases with the irradiation wavelength. The M^+/M ratio is smaller for the Mn species compared to the other metal species, which is consistent with the highest ionization potential of Mn, suggesting that the ionization is possible by multiphoton ionization, but also that 308 nm irradiation forms the highest yield of Mn^+. This may be to a two photon process (8.04 eV) with an energy close to the ionization potential of Mn, compared to the 13.4 eV and 9.4 eV to 193 nm and 266 nm irradiation. For all irradiation wavelengths the intensities reveal the same trend (La>LaO>Ca>Mn), while no clear trend is observed for the neutrals. It is noteworthy to mention that for 193 nm irradiation, the diatomic LaO reveals the highest intensity.

5.1.4 Laser fluence dependence on the ionic/ neutral yield.

By increasing the laser fluence the ablation yield increases as well, e.g. by a factor of two with increasing laser fluence from 0.8 Jcm^2 to 1.2 Jcm^2. The mass spectrum of the positive ions induced by laser irradiation at 193 nm using a higher laser fluence, i.e. 1.5 Jcm^{-2} is shown in Figure 5.2. Irradiation at a higher laser fluence induces a large intensity of positive oxygen ions, as well as polyatomic species such as LaMnO and Ca_2O.

The high signal intensity allows also the detection of the main isotopes of the plume components. The Ca species posses the most abundant isotopes from the plume components: 100 % at 39.96 amu, 0.65 at 41.95 amu, 2.12 % at 43.95 amu, 0.18 % at 47.95 amu. The different isotopes were also detected for La species. The measured isotope ratios are in agreement with the expected theoretical values.

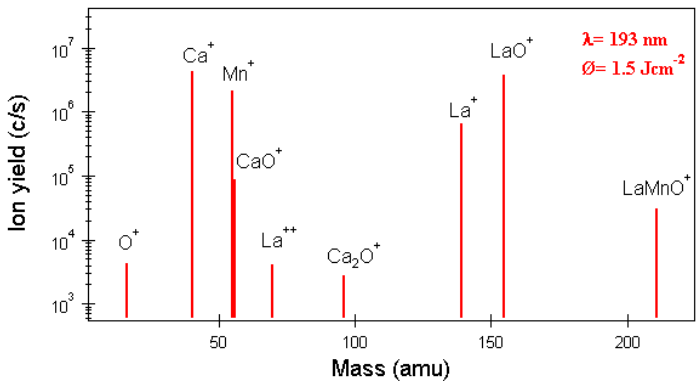

Figure 5.2: The mass distribution of the ionic species generated by laser ablation of the LCMO target using a laser fluence of 1.5 Jcm^{-2}.

The dependence of the yield of Ca ions and neutrals on the laser fluence is shown in Figure 5.4. The measured ionic yield is in general one order of magnitude larger than the neutral yield, without considering the formation efficiency of Ca ions in the electron impact ionization source, therefore a quantitative comparison between the ionic and neutral yield is not directly possible. It may be possible to conclude that more neutrals are present in the plume at the detection point. To allow a direct comparison, the intensities of both neutrals and ions were normalized, while the intensity was determined by integrating the measured kinetic energy distribution spectra (KED). An example of integrating area is shown in Figure 5.3.

The plots shown in Figure 5.4 reveal that the neutral yield increases much faster than the ionic yield and increases linear with the laser fluence. The ionic yield of the Ca species presents two regions: in the first region, a slow increase up to a fluence of $\sim$ 0.8 Jcm^{-2}, while above this fluence a faster increase of the ionic intensity is observed. The linear extrapolation of the measured intensity of the Ca ions and neutrals shows the existence of a threshold fluence of

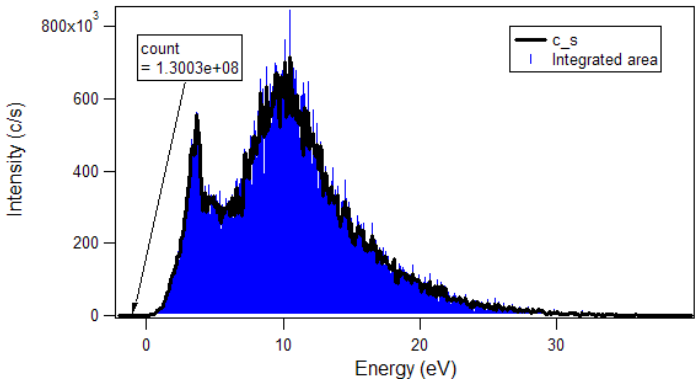

Figure 5.3: Integrated area in counts of the Ca ions generated by laser ablation at 193 nm and a fluence of 0.8 Jcm^2.

ablation between 0.2- 0.3 Jcm^2. Similar threshold values were observed for the other plume species, i.e. La, Mn and LaO. Our mass spectrometry data are in agreement with a previous report on ablation experiments analyzed by emission spectroscopy [53].

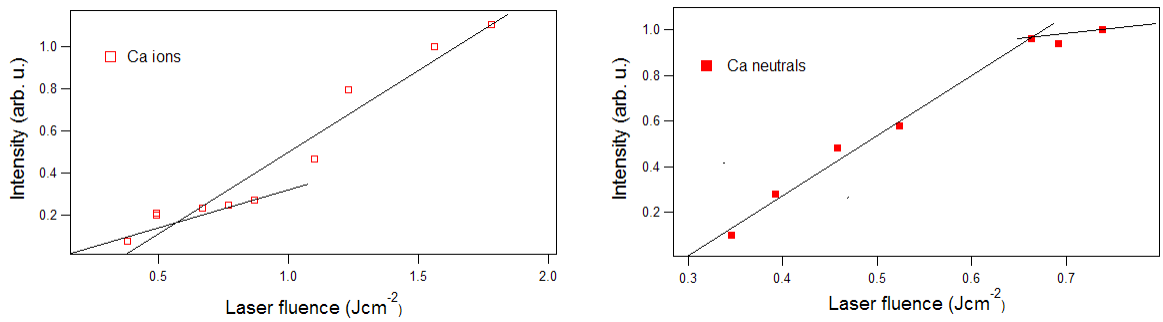

Figure 5.4: The dependence of the signal intensities of the ionic and neutral Ca species as a function of the laser fluence at a wavelength of 193 nm.

The existence an ablation threshold can be attributed to the thermal evaporation processes due to the laser- target interaction. The photon energy is converted into thermal energy, resulting in heating of the material. The induced temperature can exceed the melting temperature of the target, causing evaporation and therefore ejection of the ablated species. As the laser fluence increases, the amount of ablated materials increases as well. Above a certain laser fluence, the secondary interactions between the plume and the laser light can lead to an increase in the ionization degree of the plume. Higher temperatures in the target may result in a higher ionization degree as well. The increase of the ionic yield above 0.8 Jcm^{-2} can be therefore related to a transition from a weakly ionized vapor phase to a plasma.

5.1.5 Kinetic energy distribution of the ablated species

5.1.5.1 Theoretical aspects

The kinetic energy and angular distribution of the ablated species are the main parameters which determine the plume characteristics. In vacuum, the kinetic energy of the species was found to vary between few eV up to $\sim$ 80 eV, observed even for ns ablation [54]. In the case of the doubly and triply charged C species, generated from a graphite target, the mean energy distribution was found to be around 160 eV and 240 eV, respectively [55]. Furthermore, kinetic energies of species up to 100 eV were reported during laser ablation of Si, Ge and Cu targets. The kinetic energy was found to vary almost linear with the ion charge.

Several methods were used to determine the kinetic energy distributions of the ejected species, e.g. mass spectroscopy, ion probes, etc. In Time of Flight Mass Spectrometry (TOF- MS), the energy spectra can be derived from the TOF curves [56].

In this section, the kinetic energy of the species produced by laser ablation of a manganite target was measured using an electrostatic energy analyzer coupled with a quadrupole mass spectrometer (EEA- QMS). According to this principle, the plume species are deflected according to the energy per charge ratio (ϵ/q) and then are selected based on the mass to charge ratio (q/t). The method provides a direct measurement of the kinetic energy distribution for a given mass.

The distribution of the plume species is very often reported in the literature as a function of velocity, e. g. f(v). We will derive the distribution of the ablated species as a function of the kinetic energy, e. g. f(ϵ), which is the fitting parameter in our study.

Is it well known that a large amount of particles are emitted during the ablation process. The large number of collisions between the plume species creates a flux which expands along the normal to the target surface. The flux possesses a common velocity, often refereed as a center of mass velocity (COM), e.g. u_{CM}.

The density of the ablated species at any point (x, y, z) and any time (t) are commonly described by a shifted Maxwell Boltzmann distribution [57]:

$$n(x_i,t)dxdydzdt \approx t^{-3} \cdot exp\{\frac{m}{2k_BT_0}[(\frac{x}{t})^2 + (\frac{y}{t})^2 + (\frac{z}{t} - u_{cm})^2]\}dxdydzdt \tag{5.1}$$

where m is the mass of the particle, k_B is the Boltzmann constant, u is the stream velocity and T_0 is the local temperature in equilibration [57].

Furthermore, an elliptical Maxwell Boltzmann distribution was proposed to describe the plume as an ellipsoidal gas cloud, where the fitting parameters are angle dependent [57]:

$$n(x_i,t)dxdydzdt \approx t^{-3} \cdot exp\{\frac{m}{2k_BT_{xy}}[(\frac{x}{t})^2 + (\frac{y}{t})^2] - \frac{m}{2k_BT_z}[(\frac{z}{t} - u_{cm})^2]\}dxdydzdt \tag{5.2}$$

where T_{xy} and T_z are called the transversal and longitudinal temperatures (elliptical temperatures).

As the distance to the QMS detector is large (d= 10 cm) and the detection area is small (nozzle diameter $\sim$ 1 mm), we consider that only the particles with a velocity v_z (along the normal to the target) entering the analyzer will be detected. The density of the cloud, n(z,t), can be therefore defined as:

$$n(z,t) \approx t^{-3} \exp\left[\frac{m}{2k_B T_z}\left(\frac{z}{t} - u_{cm}\right)^2\right] \tag{5.3}$$

Following a previous suggested model [58], the number of particles detected in between t and t+ dt, possessing an energy range between E and E+dE will be given by the equation:

$$N(E)dE \propto n(z,t)v_z dt \tag{5.4}$$

From the equations 5.3 and 5.4 the following equation results:

$$N(E) = C\sqrt{E}exp\left[-\frac{m}{2k_b T_x}(v_z - u_{cm})^2\right]dE \tag{5.5}$$

The number of particles entering the detection area with a energy E_z can be described by the equation :

$$N(E) = \int C\sqrt{E_z}exp[-\frac{E_z + E_{cm} - (4E_z E_{cm})^{1/2}}{k_b T_z}]dE \tag{5.6}$$

where $E_{cm}=\frac{mu_{cm}^2}{2}$ is COM kinetic energy and $k_B T_z$ is the translational temperature.

Fitting of the energy distribution curve allows an estimation of the COM kinetic energy and translation temperature along the normal of the target surface.

5.1.5.2 Results and discussions

Figure 5.5 shows the measured kinetic energy of the Mn and LaO positive ions emitted by laser ablation at 193 nm, using a laser fluence of $\sim$ 1 Jcm^{-2}. The solid curves are the Maxwell- Boltzmann fittings of the experimental data using equation 5.6. From the fits of the experimental curves the effective temperature $k_B T_z$, the COM velocity u_{cm}, as well as the most probable energy E_p (corresponding the maximum peak position) were determined. The resulting parameters are summarized in Table 5.1.5.2.

The results summarized in Table 5.1.5.2 show that the ions have a larger stream velocities compared to the neutrals. In vacuum, the ionic species exhibit a stream velocity between 2.5$\times$10^3 m/s and 1$\times$10^4 m/s, while the neutral species vary between (2.4- 4.4)$\times$10^3 m/s. The oxygen species are among the fastest species from the plume.

The most probable kinetic energy (E_p) corresponding to the main peak of the distribution varies between 5 eV and 10 eV.

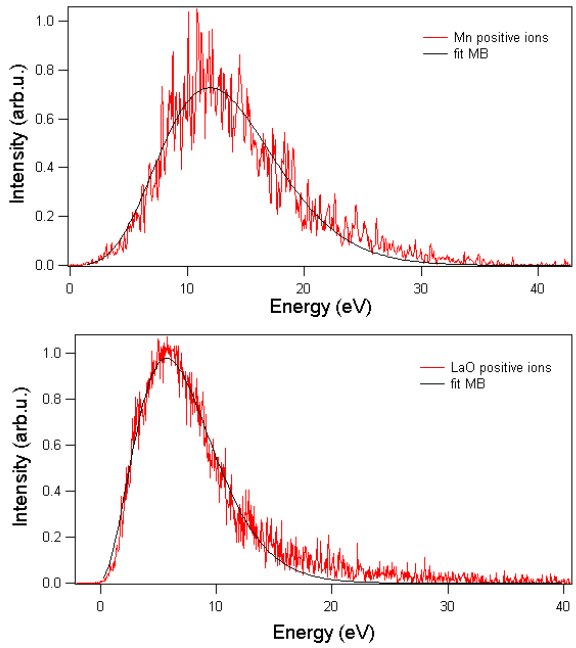

Figure 5.5: Kinetic energy distribution of Mn^+ and LaO^+ ions emitted by 193 nm laser irradiation of the La- Ca- Mn- O target. The solid curves represent Maxwell Boltzmann fits of the experimental data.

The temperature values obtained from the fits of the kinetic energy distributions are in the range of (1- 1.2) $\times$ 10^4 K for the ionic species, and (2- 3) $\times$ 10^3 K for the neutral species. Our values are in agreement with previous studies at a comparable fluence, where the temperature parameters were derived from TOF curves from a La- Ca- Mn- O target irradiated at 355 nm [52]. The temperature of the neutral species is lower than of the ionic species, suggesting that the neutral species are originating mainly from a thermal equilibrium process, such as thermal evaporation. The temperature of the ionic species is probably influenced by a non- thermal process such as photoabsorption in the plume.

The electron temperature and electron density of the expanding ablation plume can be estimated following the Phipps model [59]:

$$T_e(K) = 2.98 \times 10^4 A^{1/8}(Z+1)^{-3/8} \times Z^{3/4}(\lambda)^{1/2}\tau^{-1/4}F^{1/2} \tag{5.7}$$

and

$$n_e(cm^{-3}) = 3.96 \times 10^{11} A^{5/16} Z^{1/8}(Z+1)^{-9/16} \times \tau^{-5/8}\lambda^{-3/4}F^{1/4} \tag{5.8}$$

where A is the atomic weight (amu), Z is the average ion charge, $\lambda(cm)$ is the wavelength, τ(s) is the pulse duration, and F (Jcm^{-2}) is the laser fluence.

Using F= 1 Jcm^{-2}, Z= 1, λ= 193 nm, τ= 30 ns in the equations 5.7 and 5.8 we obtain an

Table 5.2: Parameters obtained from the Maxwell- Boltzmann fitting of the kinetic energy distributions. The parameters $k_B T_z(eV)$, u(m/s) and E_p(eV) denotes the temperature along the expansion direction (z), the corresponding velocity (stream velocity) and most probable energy, respectively.

Species	Ions			Neutrals		
	$k_B T_z(eV)$	u(m/s)	E_p(eV)	$k_B T_z(eV)$	u(m/s)	E_p(eV)
La	0.9	2.5×10^3	5.7	0.2	2.6×10^3	5
Ca	0.9	6.7×10^3	9.8	2.2	4.4×10^3	4
Mn	1	6.2×10^3	12	0.3	4.2×10^3	5
LaO	1.1	2.5×10^3	5.7	0.3	2.4×10^3	4.4
O	0.6	1×10^4	10	-	-	

electron density n_e= (1.25- 2.54)$\times10^{20}$ cm^{-3} and electron temperature T_e= (0.31- 0.37) eV. Our values are comparable with those reported in the literature for similar conditions [50], [58]. Following a previously suggested model [50], we will estimate theoretically the corresponding average energy of the ablated species. The calculated values predict mainly the plume characteristic near the target surface. Considering that the plume expands adiabatically in vacuum and that the energy is carried mainly by heavy ions, the average energy of these ions ($\bar{E}$) was estimated by the equation:

$$\bar{E} = 3.33(Z+1)kT_e \tag{5.9}$$

For Z=1 and T_e= (0.31- 0.37) eV, the average energy $\bar{E}$ was found to vary between 2 and 2.5 eV. The obtained values are much smaller than the measured values of the kinetic energies. The discrepancy can be attributed to the non- homogeneity of the beam profile as well as to the geometrical configuration [58]. In the theoretical model, it is assumed that the laser beam has normal incidence at the target, while in our studies the beam has a 45^0 incidence. Variations in the laser energy during the measurement can affect as well the measured signal.

5.1.6 Angular distribution of the plume species

5.1.6.1 Plume angular distribution studies using a mass spectrometer

The angular distribution of the ablated species is essential for film deposition as it determines the kinetic energy of the species arriving at the substrate. Here we report the spatial distribution of the species emitted by ablation at 193 nm using a laser fluence of Φ= 1 Jcm^{-2}. The ablation yield was measured at different detection angles by rotating the sample to different angles with respect to the axis of the mass spectrometer, without correcting the change of fluence due to the change of the spot size on the target. The angular distributions of the La and Ca positive ions and neutrals are shown in Figure 5.7. As expected, both ionic and neutral species are strongly forward directed along the normal of the target surface. The plots indicate that the ions have a larger angular spread compared to the neutrals.

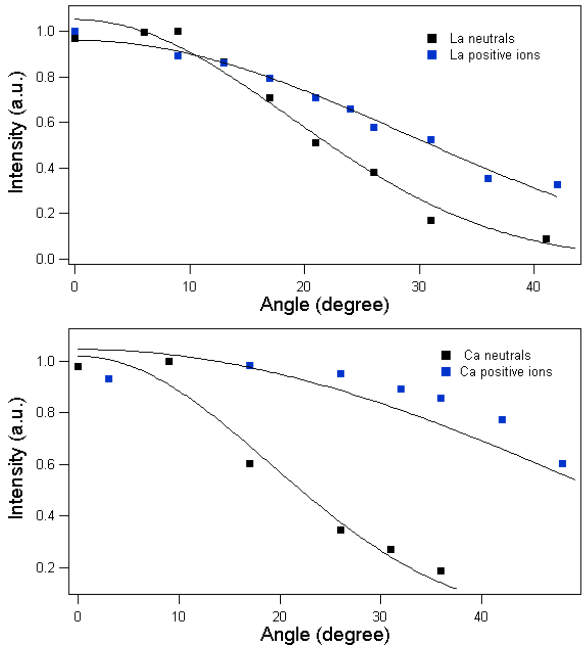

Figure 5.6: Angular distributions of the La and Ca species induced by 193 nm laser ablation in vacuum from the La- Ca- Mn- O target. The solid lines represents the fits with the function $\cos^n$(t).

According to the free expansion jet model, the angular distribution of the plume species can be fitted according to the $\cos^n(\theta)$, where n is a sharpness parameter [52]. Fitting of the plots shown in the Figure 5.7 gives n= 4 for ions and n= 9 for neutrals, which confirms the wider angular spread of ions compared to neutrals.

Similar trends were observed for the rest of the plume species, i.e. Mn, LaO, O etc. The angular distributions of all ionic and neutral species detected during laser ablation at 193 nm are shown in Figure 5.7. In the case of the ionic species the intensity of the La species decreases much

faster compared to the rest of the plume species. This may be due to a decrease in the laser energy during the measurements or a preferred reaction with oxygen to form LaO as indicated by the angle dependence of the LaO neutrals, i.e. detection of high intensities even at large angles.

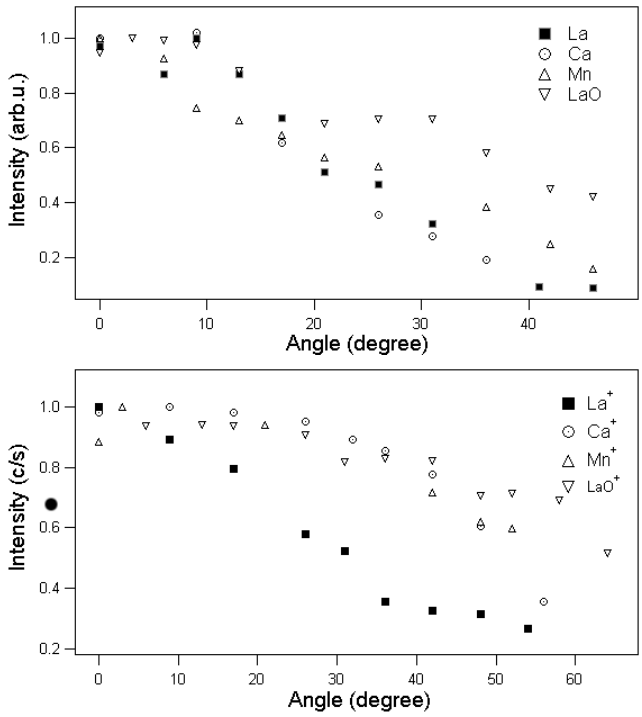

Figure 5.7: Angular distribution of the neutrals and ions emitted during laser ablation of the manganite target at 193 nm, at a laser fluence of 1 Jcm^{-2}.

Our studies reveal a different trend compared to a previously published reports on the angular distribution of the plume species from a manganite target [52], where neutrals are found to be much broader in comparison to ionic species. The difference between the experiments was the wavelength, e.g. 193 nm in our case and 355 nm for the reported data. The origin is not yet clear.

Our studies reveal that a large amount of ionic species is formed by irradiation at 193 nm. It has been suggested that ions are accelerated within the plume by the electrostatic forces created by the electron depletion and the negatively charged target. A higher degree of ionization in the plume could also increase the repulsive electrostatic forces, resulting in a broader angular distribution of the ions.

The dependence of the main energy distribution of the Ca^+ species as a function of the detection angle is shown in Figure 5.8. A maximum energy of around 10 eV is observed along the normal to the target surface and decreases very fast by 20 % at a detection angle of 8 degrees.

For a target to substrate distance of 4 cm (commonly used for PLD) and a typical substrate

area of 1 cm^2 an angular spread of the plume of 7 degrees is necessary. This shows clearly that ions with a more pronounced difference of kinetic energies arrive at the substrate, i.e. with 10 eV in the center and $\sim$ 8.6 eV at the edges (see Inset in Figure 5.8).

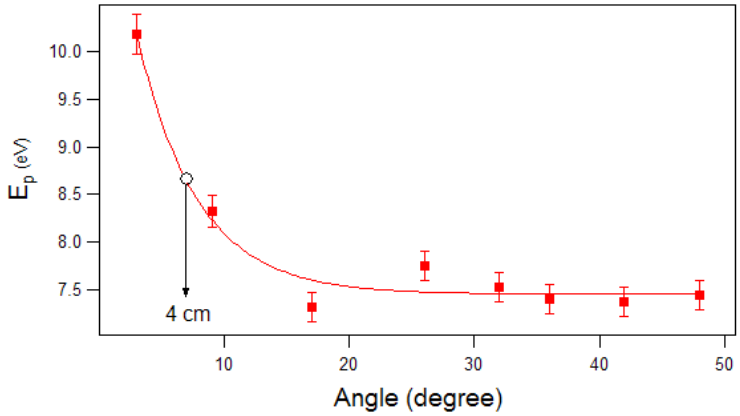

Figure 5.8: Angular dependence of the kinetic energy of the Ca ionic species induced by ablation at 193 nm, using a laser fluence of 1 Jcm^{-2}. The arrow indicates the angular spread corresponding to a typical target to substrate distance of 4 cm.

5.1.6.2 Plasma analysis by a Langmuir probe

Another way to determine the angular distribution of the ionic species is the application of a Langmuir probe. The signal obtained with the Langmuir probe represents a contribution from all ionic species in the plume.

The measurements were carried out using an ArF excimer laser , λ= 193 nm, with a laser fluence of ~3 J/cm^{-2}. The LCMO target was ablated in vacuum at a pressure of 5× 10^{-6} Pa. The angular distribution of the ionic species was monitored by biasing the probe at a voltage of -40 V and integrating the signal over 55 pulses. Similar to the mass spectrometry measurements, the target was rotated to different angles with respect to the Langmuir probe and no corrections of the laser fluence due to the change of the laser spot were performed.

The average signal of the ionic species of the plume determined by a Langmuir probe at different detection angles is shown in Figure 5.9 (a). At normal incidence (0 degree), the signal has the highest peak intensity, while at larger angles the intensity decreases and the peak becomes broadener. The angular distribution of the ionic signal as a function of detection angle is shown in Figure 5.9 (b). Fitting of the angular dependence with a $\cos^n(\theta)$ function gives a value of the coefficient, n= 5.

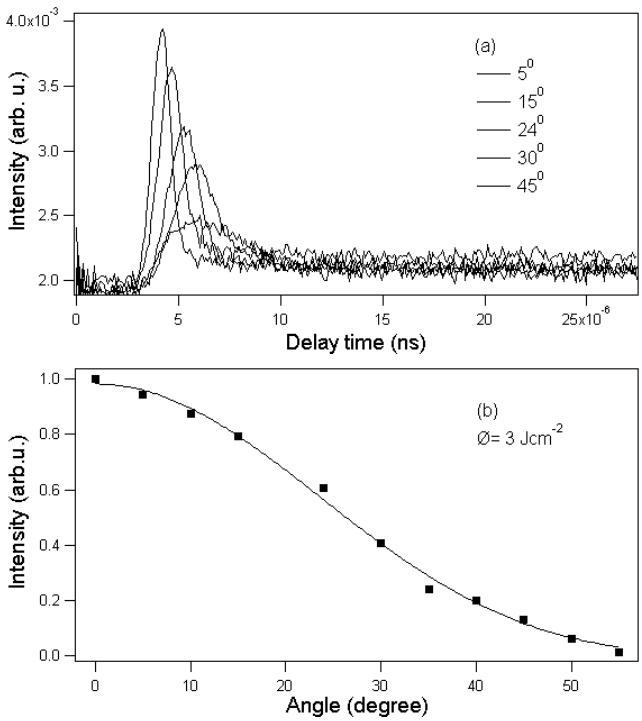

Figure 5.9: Time of Flight (TOF) of the ions detected at different angles with respect to the surface normal (a), and the angular distribution of the ionic species determined from the integrated signal as different detection angles (b). The irradiation wavelength was 193 nm and the laser fluence ~3 J/cm^{-2}.

The average normalized signal detected with the mass spectrometer, which represents an average over the analyzed ionic species La, Ca, Mn, LaO) was plotted versus the average signal of the ions detected with the Langmuir probe (see Figure 5.10).
As it can be observed, the angular distribution of the ionic species measured by the two methods follows the same trend until a detection angle of $\sim$ 20 degrees, while for larger angles the signal measured with the Langmuir probe decays much faster. This may be attributed to the higher detection sensitivity of the mass spectrometer compared to the Langmuir probe.

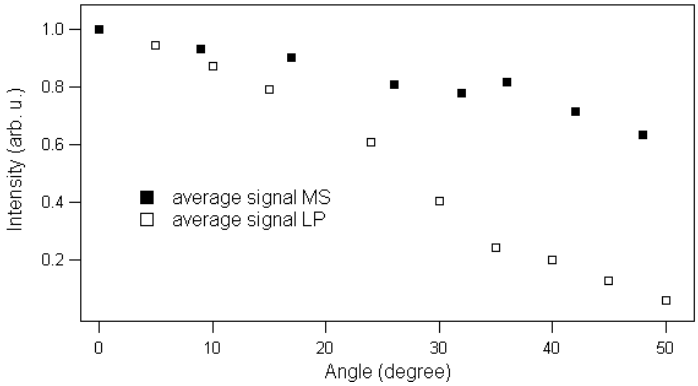

Figure 5.10: Comparison between the angular distribution of the species detected using a Langmuir probe (LP) and with the mass spectrometer (MS).

5.2 Interaction between the ablation plume and a N_2O reactive gas pulse

5.2.1 Introduction

For some materials, including manganites, the composition of the films differs from the bulk composition, i.e. the growing films exhibit large oxygen deficiencies. Several methods have been employed to reduce the oxygen deficiencies in the growing films, e.g. by supplying a high oxygen background pressure in the ablation chamber [60] or by using a RF discharge during growth [2]. Another approach to improve the oxygen content in the films was the development of Pulsed Reactive Crossed Beam Laser Ablation (PRCLA), where a synchronized reactive gas pulse interacts with the plasma plume close to its origin. The PRCLA geometry provides a high probability of reactive scattering of the laser plume and the oxidizing source. This allows in situ film analysis during and after deposition using reflection high-energy electron diffraction (RHEED) [61].
In previous plasma studies on Mn_2O_3 and $La_{0.67}Sr_{0.33}MnO_3$ targets using emission spectroscopy, a larger amount of Mn oxides has been detected when N_2O was supplied as background gas compared to O_2 [62]. This confirms that N_2O is a stronger oxidant than O_2 under plasma conditions. Laser ablation was found to be a suitable technique for the deposition of manganite films with a complex stoichiometry [63].
We have studied the influence of a reactive gas pulse of N_2O which crosses the ablation plume, close to the ablation spot, on the plume composition and formation of diatomic species. The kinetic energies of the positive/negative ions and neutrals were measured using the kinetic energy analyzer (KED). The role of oxygen and oxide species in the laser ablation process and film growth will be also discussed.

5.2.2 Mass distribution of the plume species

The mass spectra of the ionic and neutral species produced by laser ablation of the LCMO target in the presence of the reactive N_2O gas pulse are shown in Figure 5.11. No signals from N_2 species, which are formed during decomposition of N_2O into O and N_2 were detected, suggesting that this volatile species are removed by pumping. There have also been no traces of nitrogen detected in the growing films. Reactive collisions between the plasma plume and the supersonic gas pulse result in the formation of various additional neutral species (compared with the experiments in vacuum- see Figure 5.1), such as O, MnO and O_2.

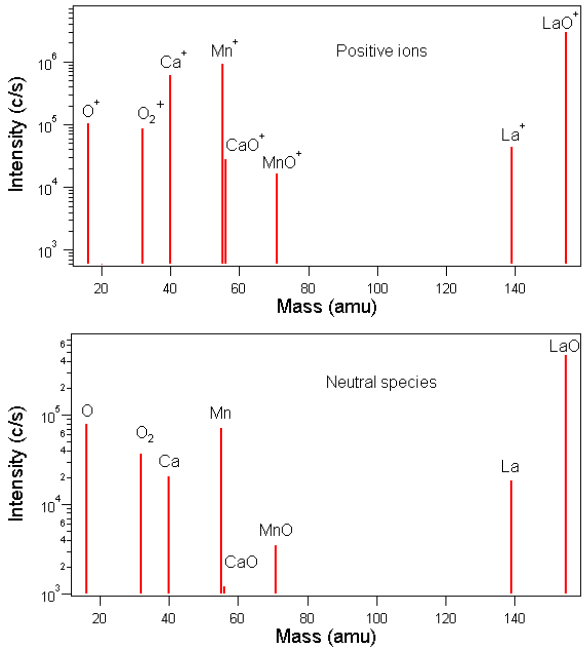

Figure 5.11: Mass distribution of the neutrals and ions generated by laser ablation of a $La_{0.6}Ca_{0.4}MnO_3$ target in a N_2O gas pulse using an irradiation wavelength of 266 nm and a laser fluence of 0.5 Jcm^{-2}.

It is noteworthy to mention that the detection of $LaMnO^+$ is only possible when the plume is directed towards the entrance nozzle of the mass spectrometer, as in the case of analysis in vacuum (see Figure 5.12 b). For the experiments with the gas pulse, the axis of the mass spectrometer is placed in between the ablation plume and gas pulse (see Figure 5.12 a), i.e. at the preferred position of the substrate in PRCLA. The very low intensity of $LaMnO^+$ suggests that the heavy species have a narrow angular distribution with a low signal intensity at larger angles or low intensities for PRCLA conditions compare to vacuum conditions. The distribution of the ablated species is similar to literature reports [52], but in the case of experiments in vacuum no polyatomic species such as La_2O_3, Ca_2O, MnO_2 were detected.

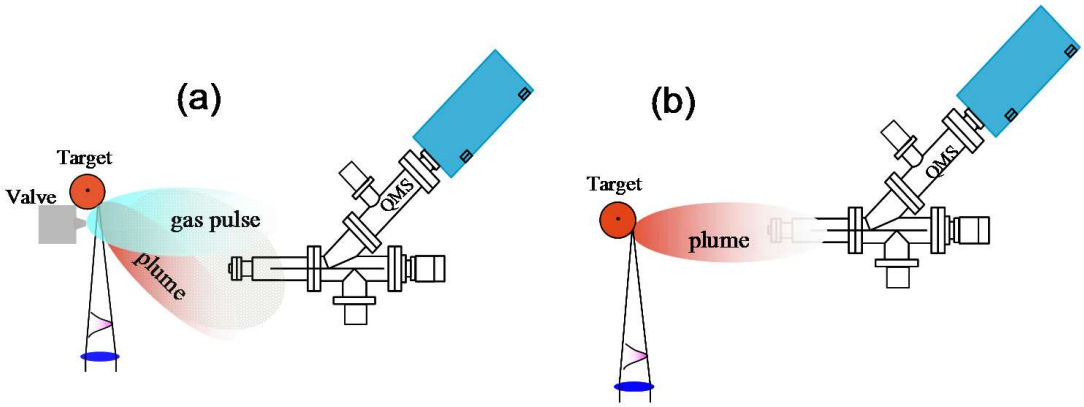

Figure 5.12: Off- axis configuration of the mass spectrometer, allowing detection of the species generated by collisions with gas pulse particles (a) and on- axis configuration of the mass spectrometer, allowing detection of the particles along the plume expansion (b).

5.2.3 Formation of O^+, O^- species

The oxygen species in the plume (positive ions, negative ions and neutrals) were studied in detail to gain a more detail insight about PRCLA, which results in a higher oxygen content in the growing films. The generation of the reactive atomic oxygen through the collisional dissociation of the N_2O molecules ($N_2O \longrightarrow N_2 + O$) requires an energy of 2.51 eV which is two times lower than for the dissociation of O_2 [62]. The N_2O is therefore more efficient in producing atomic oxygen species compared to O_2.

The translational energy of the positive and negative O ions was measured by positive, respective negative bias tuning of the electrostatic energy analyzer lenses. The kinetic energy distribution of the O^- species is much broader than that of the O^+ species, as shown in Figure 5.13 (on a logarithmic scale). The main energy distribution of the O^+ species is 3 eV, and 1.5 eV for O^- species. It is interesting that the tail of the energy distribution of the negative ions extends up to 30 eV. The negative O^- ions are the most intense plume species when the N_2O gas pulse is applied. The large amount of O^- ions suggests that it may be necessary to consider the role of negative oxygen ions for the film growth during PRCLA, i.e. they may be related to the increased oxygen content in films for PRCLA grown films compared with PLD. It is also important for these studies to analyze the formation mechanisms of O^- in more detail, which is not yet understood.

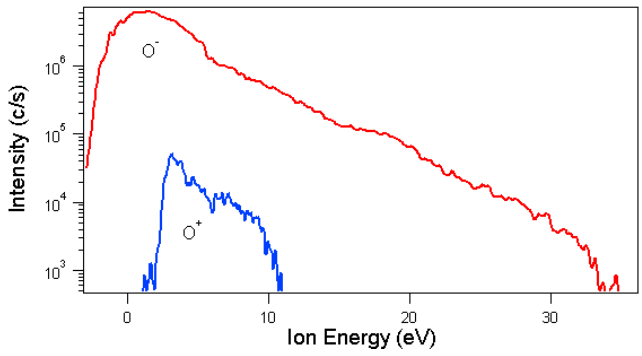

Figure 5.13: Kinetic energy spectra of O^+ and O^- in the presence of a N_2O gas pulse (τ= 400 μs and 200 kPa pressure), induced by 266 nm laser irradiation at a laser fluence of 0.5 Jcm^{-2}.

5.2.4 Formation of positive diatomic species

When the La, Ca, Mn species in the plasma interact with the N_2O gas pulse, metal oxides species are formed during collisions with N_2O and the reactive oxygen species, such as O, O^+, O^-, O_2. The formation of excited diatomic species in the gas phase has been previously observed using optical emission spectroscopy [53].

The most important aspect for the mass spectrometry analysis of the plume using PRCLA conditions is detection of the MnO diatomic species, which have not been observed for experiments without the gas pulse. The energy distributions of the MnO^+ ionic species measured at a background pressure of 0.1 Pa pressure during PRCLA are shown in Figure 5.14. The main energy peak distribution decreases by 0.5 eV in PRCLA compared to the classical PLD, confirming an increase of the gas phase scattering during PRCLA. The formation of the MnO diatomic species in PRCLA is therefore favored due to the increased number of collisions but also due to a more efficient generation of atomic oxygen by decomposition of N_2O gas pulse.

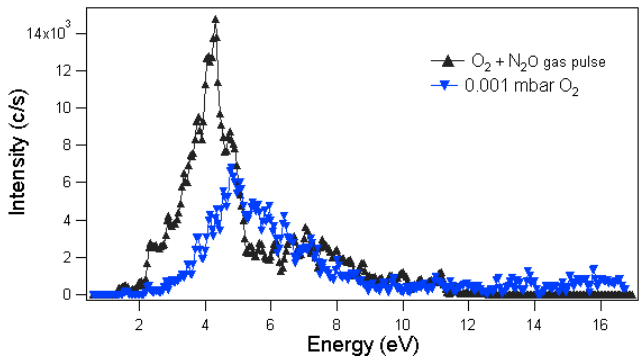

Figure 5.14: Translation energy of the MnO^+ diatomic species at a static O_2 pressure of 10^{-3} mbar and PRCLA.

The LaO^+ signal intensity increases by more than one order of magnitude compared with the

experiments in vacuum, while at a given laser fluence of 0.5 Jcm^{-2}, the intensities of CaO^+ and MnO^+ increase by 5 orders of magnitude. The origin of the different increase for LaO and CaO, MnO is not clear. The diatomic species are favorably formed during interactions between plume species and the gas pulse, e.g. by reactions of the metal species with the oxygen species formed during the dissociation of N_2O molecules:

1. $N_2O \longrightarrow N_2 + O$
2. $M^+ + O \longrightarrow MO^+$

Figure 5.15 shows the translational energy curves of the La/LaO (top) and Ca/CaO (bottom) positively charged species. The measured kinetic energy distributions of the positively charged diatomic ions reveal a main energy distribution in the low energy region (2- 4 eV), as well as a smaller contribution at higher energies, i.e. around 6- 8 eV.

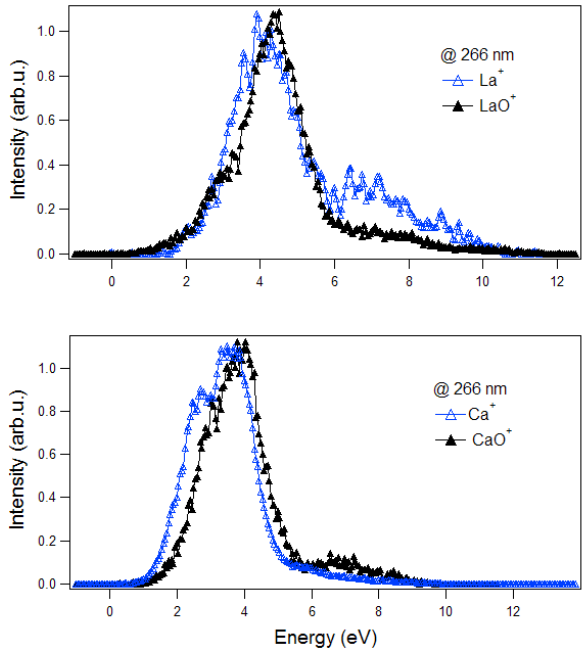

Figure 5.15: Kinetic energy distribution of La^+/LaO^+ and Ca^+/CaO^+ diatomic species measured in PRCLA setup.

5.2.5 Formation of negative diatomic species

Another important aspect in our studies is the detection of various negative ions, such as O^-, O_2^-, CaO^-, MnO^- and LaO^-. The negative ions are only rarely discussed in the literature. One example is the presence of negatively charged particles emitted by laser ablation from sodium trisilicate glass using the TOF mass spectrometry technique [64].

To our knowledge, no reports have been published on negative ion emission during irradiation of a manganite target. In general, the intensity of the negative species is lower than for the positive species, with the exception of the negative $O^-$and O^{2-} ions, which are formed in high yield during interaction of the plume with the N_2O gas pulse. The measured kinetic energy spectra of all detected negative ions are shown in Figure 5.16 , reveal a main distribution ranging between 1 eV and 2 eV. It is noteworthy to mention that the intensity of the O^{2-} species is up to three orders of magnitude higher than for the other species.

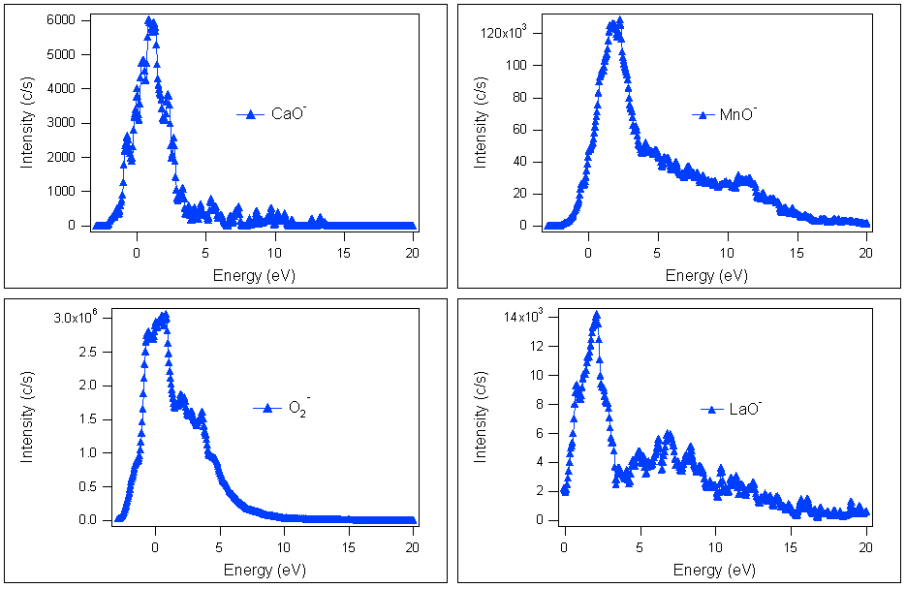

Figure 5.16: Kinetic energy distribution of the diatomic negatively charged species.

The negative ions are among the slower ions in the plume, even slower than the neutrals. This may be related to the formation mechanisms in the plume, or electrostatic forces within the plume or from the target. The role of negative ions in the process of thin films growth is also not clear at the moment, but PRCLA, where more negative ions are produced, has yielded better results in terms of oxygen content for oxide materials. It is therefore reasonable to assume that the negative ions are also important for thin film growth and oxygen content of the films.

5.2.6 Discussion

The negative species are among the slower species in the plume and are mainly formed in the presence of the gas pulse. The diatomic (positive, negative) MnO and CaO species are favorably formed in the gas phase by reactions with oxygen species generated from the N_2O gas pulse. The high amount of O^-/O^{2-} species, generated by reactive scattering with the N_2O gas pulse, suggests that they may be an important aspect in the film growth, but also fundamentally in PLD, where also plume species collide with gas molecules.
A comparison between the kinetic energy of the species emitted by laser ablation in vacuum and in the presence of the gas pulse has been carried out and the main energy values derived from the kinetic energy distributions are summarized in Table 5.3.

Table 5.3: The main energy values of the species generated by laser irradiation at 266 nm in the presence of the N_2O gas pulse.

	Vacuum (p< 10^{-7} mbar)		Gas pulse		
Species	M^+	M	M^+	M^-	M
La	5.2 eV	2.3 eV	4.1 eV	-/-	2.3 eV
Ca	4.2 eV	2 eV	3.3 eV	-/-	2 eV
Mn	5 eV	2.6 eV	3.5 eV	-/-	2.1 eV
O	16 eV	-/-	3 eV	1 eV	-/-
O_2	-	1 eV	3 eV	1 eV	1 eV
LaO	5.1 eV	3 eV	4.3 eV	1.8 eV	2 eV
CaO	-/-	-/-	3.7 eV	1 eV	1.6 eV
MnO	-/-	-/-	4.2 eV	1.8 eV	1.7 eV

The graphical expression of the kinetic energy dependence on the atomic mass of the detected species in the plume are shown in Figure 5.16.

The maximum energy distribution of the ablated species were derived from the measured kinetic energy spectra in vacuum and in the presence of the N_2O gas pulse. The main observations are:
(a) In vacuum, the ionic species are faster than the neutral species. The kinetic energy of the ionic species varies between 4 and 5 eV (with the exception of O^+ with a main kinetic energy at 16 eV), while the neutral species have kinetic energies between 1 and 3 eV.
(b) In the presence of the reactive gas pulse, the ionic plume species are considerable slowed down by 2 to 3 eV (oxygen decreases from 16 eV to 3.4 eV).
(c) The negative species are among the slower species in the plume and are mainly formed in the presence of the gas pulse.

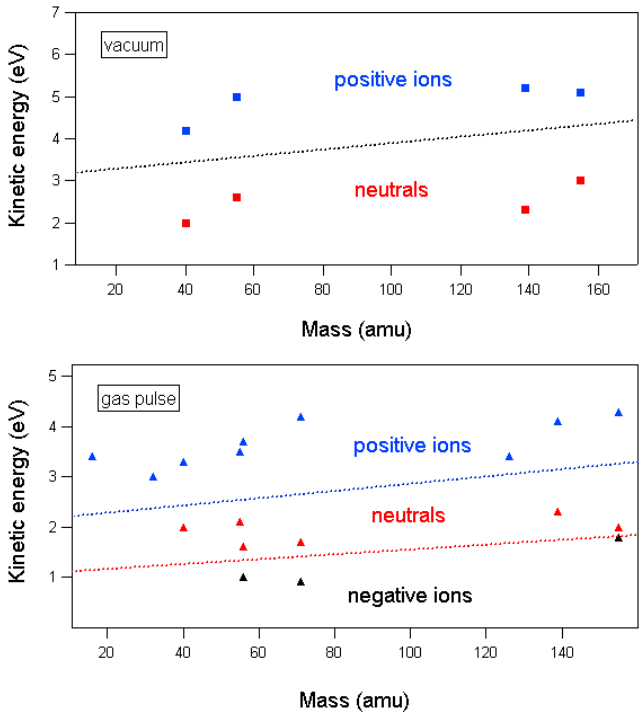

Figure 5.17: Kinetic energy dependence on the atomic mass of the ablated species.

(d) The diatomic (positive, negative) MnO and CaO species are favorably formed in the gas phase by reactions with oxygen species generated from the N_2O gas pulse.

5.3 Conclusions

The plume composition and energy distribution of the species emitted by laser ablation of the $La_{0.6}Ca_{0.4}MnO_3$ target at different irradiation wavelengths were investigated. Both vacuum and gas pulse conditions were analyzed.

Our studies reveal that the irradiation wavelength influences the ionization degree of the plume, i.e. for higher photon energies a larger degree of ionization of the plume is observed. In vacuum, ejection of metal ions, such as La^+, Ca^+, Mn^+, O^+, as well as diatomic LaO^+ were observed. The large intensity signal of the LaO^+ species can be attributed to the high bond dissociation of the diatomic molecules as well as the high oxidation potential. The plasma temperature and electron density were determined using a hydrodynamical model for the plume. The temperature of the neutral species was lower than for ionic species, for which the most probable kinetic energies vary between 5 and 10 eV. The angular distribution studies have shown that for vacuum conditions the ions exhibit a wider angular distribution compared to the neutral species.

When a reactive N_2O gas pulse crosses the laser plume close to its origin, a considerable increase of the oxide species is observed. Various diatomic positive species such as LaO, MnO, and CaO are detected. Another important aspect is the oxidation of Mn species, which is more efficient in PRCLA compared to classical PLD using a comparable overall deposition pressure.

The negatively charged species, MO^- and $O^-/O_2{}^-$, which are preferentially formed in the plume during interactions with the N_2O gas pulse, are among the slowest species in the plume. The high amount of $O^-/O_2{}^-$ species generated by reactive scattering with the N_2O gas pulse suggests that they may be an important aspect in the films growth, but also fundamentally in PLD, where also plume species collide with gas molecules.

Chapter 6

Alternative spectroscopic methods for plume characterization.

Changes in the composition of a $La_{0.6}Ca_{0.4}MnO_3$ target to $La_{0.6}Ca_{0.4}MnO_3$ thin films were observed. One possible reason is a different behavior of light elements in the plume. Therefore $LiMn_2O_4$, which is a material of interest for re- chargeable lithium batteries, has been selected, where Mn and O are still present, but a really light element was added, e.g. Li. This chapter includes studies on plasma spectroscopy using two complementary spectroscopic methods: plume imaging and optical emission spectroscopy. Both methods provide information of the spatial and temporal characteristics of the excited species in the plume. The methods will be employed for studying the plume expansion of Li species emitted by laser ablation of a $LiMn_2O_4$ target. A comparison between the plume dynamics induced by ns and fs laser ablation of a $La_{0.6}Co_{0.4}O_3$ target will be also discussed, because for fs ablation a deficiency in one element, i.e. Co was detected.

[1]

[1]Part of the data included in this chapter has resulted in the following publication:

S. Canulescu, E. Papadopoulou, D. Anglos, Th. Lippert, A. Wokaun, Plume expansion during laser ablation of $LiMn_2O_4$ target, Journal of Applied Physics.

S. Canulescu, E. Papadopoulou, D. Anglos, Th. Lippert, A. Wokaun, Plume emission induced by fs and ns laser ablation of $La_{0.6}Ca_{0.4}O_3$ target: Comparisons between plume dynamics- in progress

6.1 Study of the plume expansion during laser ablation of $LiMn_2O_4$

6.1.1 Introduction

Lithium manganese oxides can be considered attractive cathode materials in Li- ion batteries due to several advantages compared to $LiCoO_2$ and $LiNiO_2$, such as low cost and availability [65]. Recent studies have shown the potential of $LiMn_2O_4$ and $LiMnO_2$ materials in rechargeable lithium batteries [66]. Due to their high energy density Li- batteries can be used as a rechargeable power source in mobile phones, digital cameras, and other small electronic devices.

It has been suggested that high quality $LiMn_2O_4$ thin films can be obtained by Pulsed Laser Deposition (PLD) although the Li content is questionable [67], [31]. Several investigations have also shown a Li deficiency for other Li containing films, such as $LiNbO_3$ [67]. Perea et al. [68] reported that the plume induced by laser ablation of $LiNbO_3$ consists of a wider distribution of Li atoms in the plume than observed for Nb atoms. They also observed a delayed emission of Li atoms in the plume, which may also explain the low Li content observed in the film composition, but whether these observations are also relevant for the deposition of $LiMn_2O_4$ have not been analyzed yet [68].

Previous studies on $LiMn_2O_4$ films revealed a low Li content in the deposited films compared with the target material [31]. Films grown in vacuum conditions are highly Li and O deficient, while the best transfer is obtained at an oxygen pressure of 20 Pa. Nevertheless, the Li deficiency could not be overcome completely, but strong indications have been found that preferential re-sputtering of Li from the growing films occurs at low background pressures by the species with high kinetic energy [69]. Even under the best conditions it was not possible to achieve a congruent Li transfer, a lithium deficiencies larger than 5% remaining. Therefore additional origins for Li deficiency must exist. Our approach to understand the additional origin of the Li- deficiency is the detailed analysis of the PLD process, and especially the plasma.

Several spectroscopic methods using an ion probe [70], mass spectrometry [71], emission spectroscopy [53] and plume imaging [72] were employed to investigate plume dynamics during the PLD process. Briefly, the PLD process consists of three main steps: (i) interaction of the laser beam with the bulk target, (ii) plasma formation, heating, and initial three- dimensional isothermal expansion, and (iii) adiabatic expansion and deposition of thin films. The first two processes occur during the laser pulse, while the last process initiates after the laser pulse.

The free expansion of the plume in vacuum can be described as adiabatic. When the background pressure increases, the plume behaviour changes dramatically depending on both gas pressure and type [70]. Several effects on the plume expansion were observed: the increased collisions between background gas molecules and plume species induce a shock front formation, plume

confinement, and stopping compared with vacuum propagation [10].

A simplified model of plume expansion in oxygen atmosphere has been proposed by Arnold et al. [73] in which the plume is described using two main coordinates, e.g. spatial and temporal. The initial stage of a plume is similar to an inertial expansion into vacuum, while the later expansion can be described by point- blast model with [9].

We study the dynamics of the plume induced by laser ablation of $LiMn_2O_4$ both in vacuum and in an oxygen background gas, at a pressure which has been shown to yield the lowest Li deficiency. The temporal and spatial plume evolution is investigated using time resolved emission spectroscopy and plume imaging. The combination of these two methods in particular will help to elucidate mechanisms that lead to Li deficiency in the deposited $LiMn_2O_4$ films.

6.1.2 Optical emission spectroscopy studies

An overall emission spectrum corresponding to the ablation of the $LiMn_2O_4$ target using a 248 nm laser is shown in Figure 6.1. The most intense lines of Li I (at 610 nm and 670 nm, respectively) dominate the entire emission spectrum, followed by the Mn I, Mn II and O I species. No Li II were observed in the recorded region because of the low intensity. Other intense peaks, observed at wavelengths above 700 nm are second order diffraction peaks. No emission arising from diatomic species, such as MnO (558.5 nm), were observed in the entire emission spectrum recorded from 300 to 900 nm.

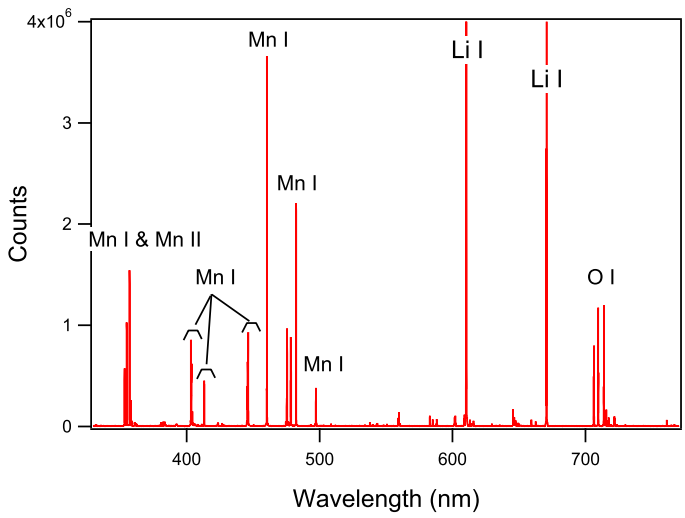

Figure 6.1: Optical emission spectra generated from laser ablation in vacuum of the $LiMn_2O_4$ target, using a KrF excimer laser (fluence 2 Jcm^{-2}) as an irradiation source.

The emission lines of Mn I and Mn II species with wavelengths in the range of 340- 350 nm were investigated in detail (see Table 6.1). Emission from the ablation plume in the presence of 20 Pa O_2 oxygen is compared to the plume emission in vacuum: the emission intensities corresponding to Li I, Mn I, Mn II species, recorded at different delay times, are shown in Figure 6.2. The maximum intensity is attained in vacuum at earlier times, e.g. in the time interval from 250 to 350 ns. In background gas the maximum intensity can be detected between 400 and 500 ns, indicating that the plume species are slowed down by collisions with the gas molecules. The emission intensity profiles become sharper because of plume confinement induced by the background gas. The maximum of the Mn^+ (Mn II) species is observed prior to the neutral Mn species in both environments, suggesting different velocities of the species.

The temporal evolution of neutral and ionic emission lines were analyzed at various distances from the target in order to derive the velocities of these species. Plots of the distance versus time allow an estimation of the average velocity of the species. Figure 6.3 (a) and (b) shows the plots corresponding to Li I and Mn II plume species, respectively, in vacuum and in the presence

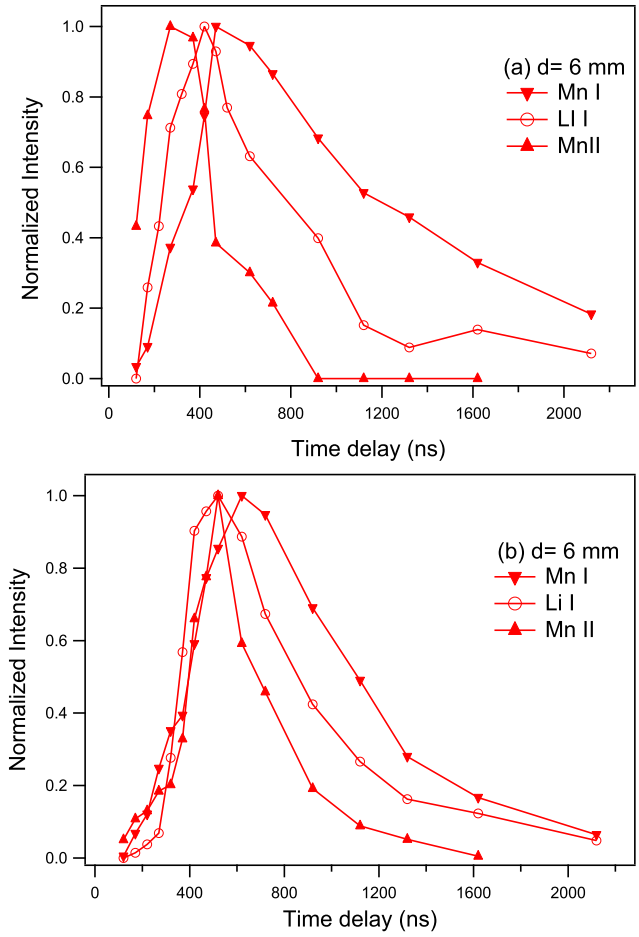

Figure 6.2: Normalized emission intensity distribution from Mn I, Mn II and Li I species recorded at 6 cm from the target surface in (a) vacuum and (b) at 20 Pa O_2, using a laser fluence of 2 Jcm^{-2}.

of 20 Pa O_2 pressure. The velocities of the Li I and Mn II in vacuum are 2.1 ($\pm$0.02) $\times$ 10^4 m/s and 2 ($\pm$0.02) $\times$ 10^4 m/s, respectively, while the Mn I species revealed a velocity of 1.9 ($\pm$0.02) $\times$ 10^4 m/s (not shown).

In vacuum, the emission intensity of Mn II species decays at around 5 mm from the target surface in vacuum, while in the case of Li I species the intensity decay is observed at much larger distances, i.e. around 12 mm from the target. Similar decays at around 5 mm from the target were observed for the Mn I and O I species (not shown here). The radiative lifetimes of the analyzed excited species (included in Table 6.1) reveal that the Li species (670 nm emission wavelength) exhibit radiative lifetimes 3 to 4 times longer than the Mn species. However, the emission intensity arising from Li species can be detected at delay times larger than 820 ns, while for Mn I and Mn II species the intensity decay at delay times $<$ 420 ns. The observed Li emission signal at larger distances and delay times can therefore not just be explained by the differences in lifetimes. This suggests that different mechanisms are involved in the emission

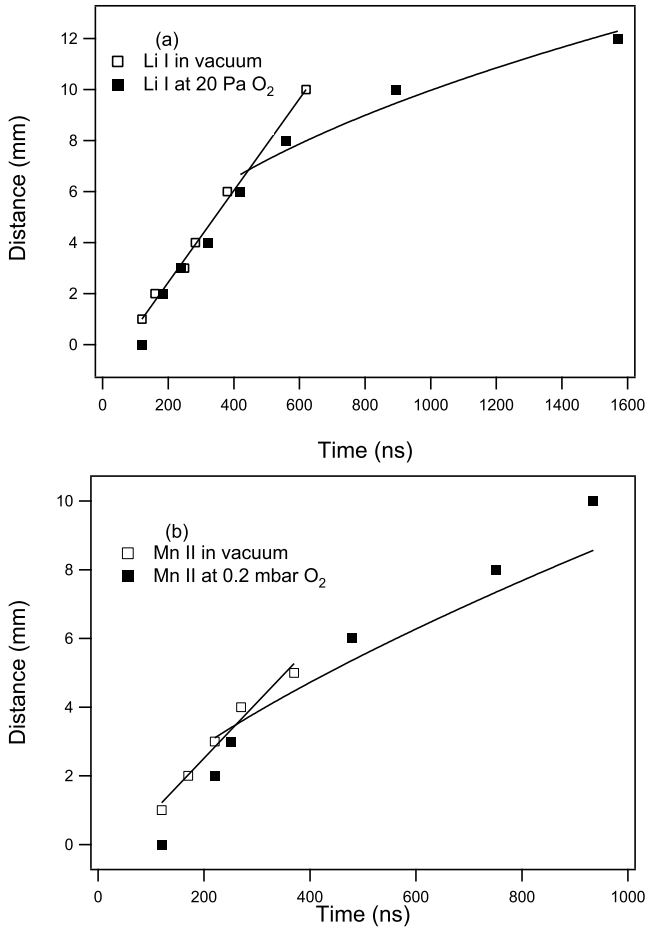

Figure 6.3: Distance versus time dependence of the Li I (a) and Mn II species (b), respectively, in vacuum and at 20 Pa O_2 pressure. The fittings corresponding to the free flight in vacuum (straight line) and plume expansion in gas (based on the shock wave model) are shown. Laser fluence was 2 Jcm^{-2}.

and expansion of the Li I species in vacuum.

The emission intensities of the species maintained over a larger time/distance scale, can be attributed to the additional collision induced excitation processes with oxygen background molecules (see Figure 6.3). A considerable increase in intensity is observed for the Mn species. The emission intensity behavior can be divided into two regions: a first region can be fitted using a linear function, while the attenuated region due the gas collisions can be fitted using the shock wave model. Both liner and SKW fitting are shown in Figure 6.3. Because the emission intensity decays to the noise level at distances larger than 1 cm, fitting with the shock wave model (SKW) cannot be accurately done due to the limited number of measurements points.

The Li and Mn velocities in background gas were calculated from the initial linear expansion and are compiled in Table 6.1. The main difference in the velocities between the vacuum and collision- free expansion is observed for Li, which exhibits a lower velocity in the presence of a background gas.

Table 6.1: The calculated velocities of the species obtained from emission spectroscopy.

Species	Wavelength (nm)	Radiative Lifetime (ns)	Velocity Vacuum ($\times 10^4$ m/s)	Velocity 20 Pa O_2 (Collision- Free Expansion) ($\times 10^4$ m/s)
Li I	670	27	2.1 ($\pm$0.02)	2($\pm$0.02)
Mn I	355	5	1.9 ($\pm$0.01)	1.1 ($\pm$0.01)
MnII	340	10	2($\pm$0.02)	2 ($\pm$0.02)

6.1.3 Time resolved imaging of the $LiMn_2O_4$ plume

Vacuum

Time resolved plume imaging gives additional information about internal dynamics of the plume and allows plume emission detection over a large scale [**?**]. Figure 6.4 illustrates i- ICCD images of the plume resulting from the ablation of the $LiMn_2O_4$ target at a residual pressure of 10^{-4} Pa. Gain was appropriately adjusted to compensate for the emission intensity reduction at greater distances or times during measurements. The total optical emission was filtered to allow detection of single species from the plume. The optical emission of the filtered images for (a) Li I (b) Mn I and (c) Mn II are shown in Figure 6.4, with the delay time indicated in each picture. The first row shows the filtered emission (670 nm) corresponding to Li I, the second row the Mn I species and the third row the emission from Mn II.

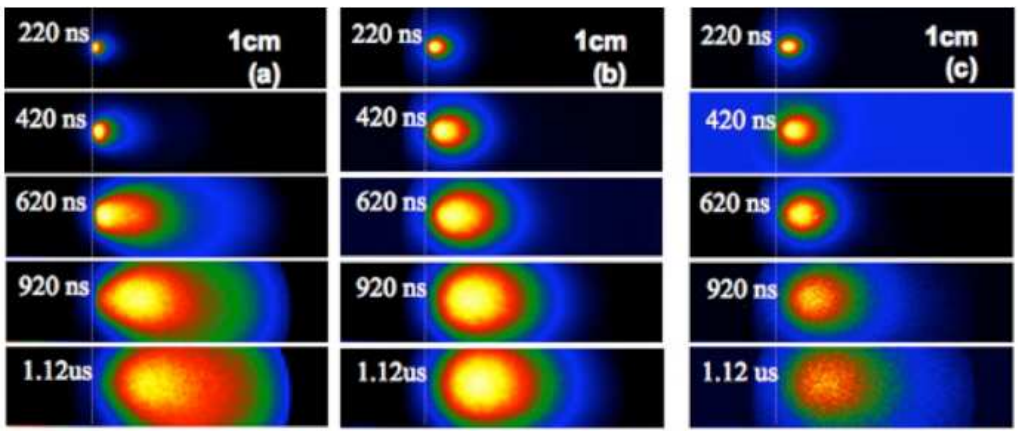

Figure 6.4: ICCD images of the emission of the plume induced by ablation of the $LiMn_2O_4$ target in vacuum. The images were filtered using appropriate band width filters, allowing detection of single species such as (a) Li I, (b) Mn I and (c) Mn II. Each image is normalized to maximum intensity. The laser fluence was set at 2 Jcm^{-2}. The target position is indicated by the dashed lines.

A description of band filters used for the plume imaging experiments, together with the emission

lines investigated with the plume imaging method are given in Table 6.2.

Table 6.2: Optical emission lines of the manganese and lithium species with emission signal relative intensity and dielectric filters used for plume imaging experiments shown above.

Wavelength	Configuration	Relative Intensity	Filters
Lithium neutrals (Li I)			
670.68	$1s^2 2p \longrightarrow 1s^2 2s$	360	FHWM of 10.21 nm centered at 670.7 nm
Manganese neutrals (MnI)			
354.78	$3d^6(^3H)4p \longrightarrow 3d^6(^3G)4s$	1300	FHWM
354.78	$3d^6(^3H)4p \longrightarrow 3d^6(^3G)4s$	1100	of 10.04 nm
354.78	$3d^6(^3H)4p \longrightarrow 3d^6(^3G)4s$	900	centered at 354 nm
Manganese ions (MnII)			
344.19	$3d^5(^6S)4p \longrightarrow 3d^6$	720	FHWM
346.03	$3d^5(^6S)4p \longrightarrow 3d^6$	320	of 10.04 nm
347.40	$3d^5(^6S)4p \longrightarrow 3d^6$	360	centered at 341 nm

In the first few hundred nanoseconds, e.g. 420 ns, a hemispherical expansion of the plume is observed for all species (see Figure 6.4). After 620 ns different dynamics of the plume species can be observed. The plume emission corresponding to Mn I and Mn II maintain the same hemispherical shape, and the intensity decays considerable after 1200 ns.

Significant emission decay is observed for Mn II species due to the lowest relative intensity of the emission lines (see Table 6.2), or due to a possible low amount of ionized Mn species and recombination with electrons to form neutral Mn I species.

The emission arising from the Li species at 620 ns consists of at least three distributions, resulting in an apparent elongation along the expansion direction. Furthermore, after 920 ns the plume edge is still in close contact with the target surface, resulting in formation of a flat ″interface″ between target surface and plume (see Figure 6.4). The presence of the emission at the target surface at such a long time can be probably attributed to a delayed emission, as it will be discussed later.

The angular broadening of the plume emission is higher in case of Li I species compared with the Mn I species, but comparable with the Mn II species. Any possible different expansion of the species parallel to the target surface cannot be detected clearly in vacuum.

The plume imaging data were used to analyze the temporal and spatial evolution of the plume. The profile lines of the plume along the expansion direction were used to determine the plume front position, defined as the distance at which intensity reaches 10% of the maximum.

The plume emission profiles of the corresponding Li I, Mn I, and Mn II species along the plume

expansion were studied at different delay times. Normalized temporal profiles corresponding to the Li I, Mn I and Mn II specie at a delay time of 620 ns and 920 ns are shown in Figure 6.5 (a) and (b), respectively. Plume emission profiles corresponding to the Li I species along the expansion consist of at least three different regions, while Mn I and Mn II emission intensities profiles show mainly one intense peak, with the maximum peak intensity varying linearly in time. The first distribution is observed at the leading edge of the plume, a second distribution propagates almost at similar velocity to the other plume species (Mn I and Mn II), and the third distribution is observed at the target surface. At 920 ns or later, the plume emission exhibits a large broadening along the expansion direction, which can be assigned to the three distributions, observed at early times. Thus, the Li profile become much larger along along the expansion direction compared to Mn I and Mn II species.

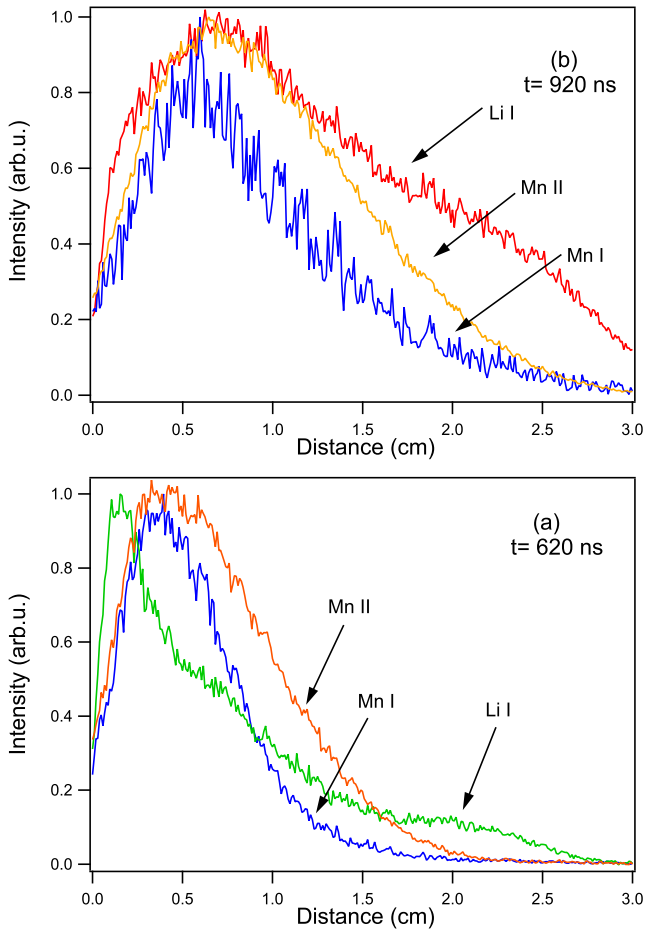

Figure 6.5: Emission intensity profiles obtained from plume imaging of Li I, Mn I and Mn II species at different delay times, 620 ns (a) and 920 ns (b). The normalized intensities are shown. The measurements were performed in vacuum at a laser fluence of 2 Jcm^{-2}.

The mean velocities of the emitted components were estimated using the plume imaging profiles. The maximum emission intensities were obtained by fitting the intensity profiles at different delay

times with Gaussian function. The derived peak positions as a function of delay time for Li I species and Mn I & II species are shown in Figure 6.6 (a) and (b), respectively. The velocities obtained for the three peaks of the Li I species, assuming a linear relation, are indicated in Figure 6.6 (a) are 3.3(±0.01) × 10^3 m/s, 1.4(±0.02)×10^4 m/s, and 1.8(±0.01)×10^4 m/s. The velocities (also assuming a linear relation) shown in Figure 6.6 (b) of the Mn II and Mn I species are 6.7 (±0.01) × 10^3 m/s and 6.1(±0.01) × 10^3 m/s, respectively.

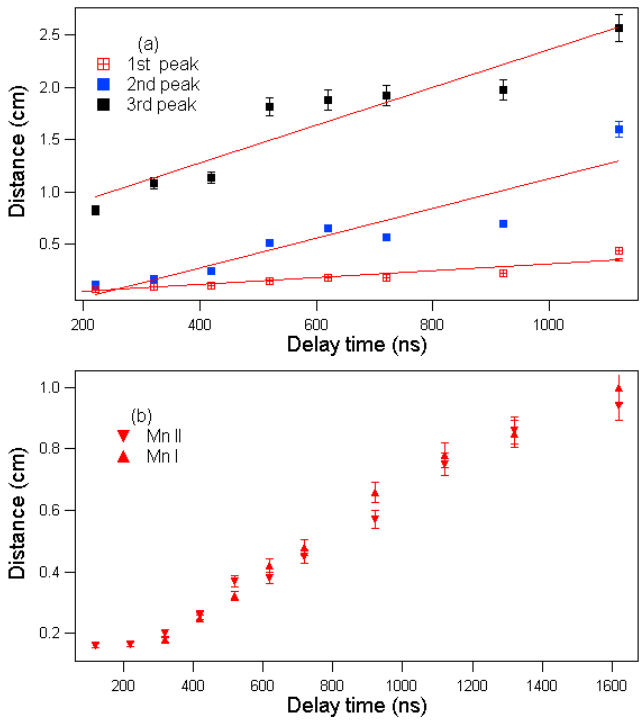

Figure 6.6: Distance versus time dependence of Li I (a) and Mn II & Mn II species (b) obtained for the analysis of the emission profiles at different delay times.

The velocities of the fastest Li species correspond quite well with the data from the spectroscopic measurements, while the velocities of the Mn species are lower compared to the values reported in Table 6.1.

Oxygen background

The plume emission evolution in 20 Pa O_2 background pressure for the Li I, Mn I, Mn II and O I species is shown in Figure 6.7. A dashed line is inserted in each series as a clear observation for plume splitting.

The high- density plume created by laser ablation expands perpendicular to the target surface. During the expansion into the background gas, it pushes the gas molecules away and the plume front undergoes multiple scattering with the gas species, while some species travels collision free resulting in the observed plume splitting [70]. Two plume distribution are observed at very long time delay for Mn I and Li I (420 ns), while for Mn II the plume splitting occurs at earlier times,

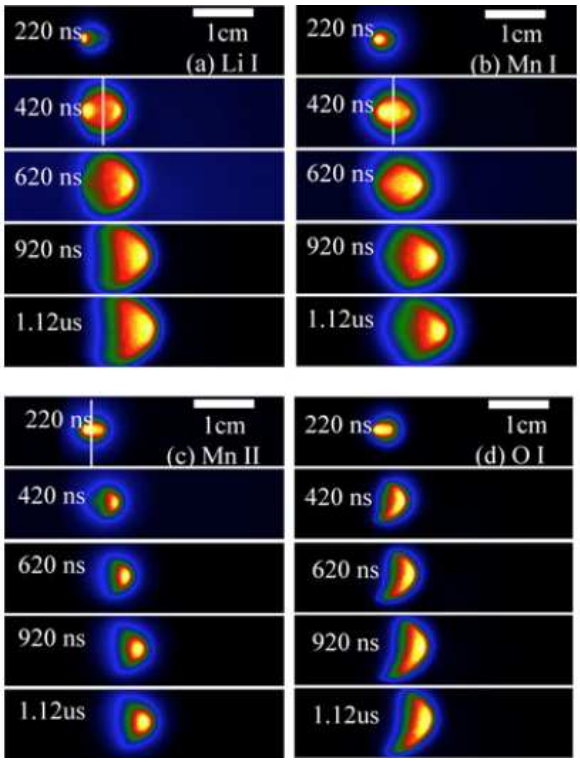

Figure 6.7: Plume emission images of the plume induced by $LiMn_2O_4$ ablation at a background pressure of 20 Pa O_2. The time scale varies from 120 ns to 1.12 μs. All images are normalized to maximum intensity. The laser fluence was 2 Jcm^{-2}.

i.e. 220 ns, consistent with literature reports [70]. The plume front is slowed progressively with a considerable plume confinement observed at later times, which is clearly observed from the fast increase in emission intensity at the plume front (see Figure 6.7).

The profiles of the emission lines along the expansion direction for the Mn I, Mn II, Li I and O I species are shown in Figure 6.8 (a), (b), (c) and (d).

Different plume dynamics for Li I are observed compared to Mn I, Mn II and O I species. At 120 ns (not shown here) the emission profiles of the Mn and O species show a single peak structure, while Li exhibits at least a double peak structure. In Figure 6.8 (c) (showing Li I profiles) a secondary peak is clearly observed and well separated from the first peak at a delay time of 420 ns. The appearance of a secondary peak is observed for the other species at later times, suggesting a faster expansion of Li compared with the Mn and O species. After few hundred nanoseconds (520 ns for Li) the secondary peak of the Li species gains intensity with respect to the first peak, and at later times the two peaks merge. A similar behavior is observed for Mn I, Mn II and O I species, but the merging effect of the two peaks occurs at earlier times, e.g. at 420 ns from Mn I. At the latest stage of plume expansion, the plume broadens considerably.

The spatial separation, S, of the two plume components for Li I, Mn I and Mn II species is shown in Figure 6.9 (a), (b) and (c), respectively. The peak positions were determined by fitting

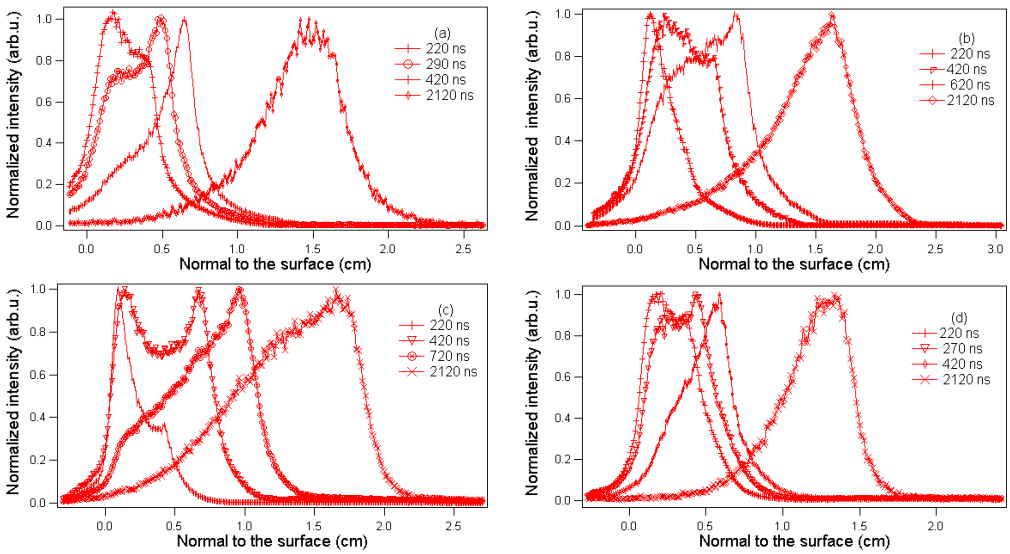

Figure 6.8: Normalized emission intensity distributions perpendicular to the target for (a) Mn I, (b) Mn II, (c) Li I and (d) O with time scale from 220 ns to 2210 ns and a background pressure of 20 Pa O_2. The profiles were selected properly to show the most dominant effects, which occur at different delay times for Li compared to Mn and O.

the profiles with Gaussians. As it can be observed, the plume splitting in the case of Li I species (see Figure 6.8 (a)) appears already at 220 ns, while the spatial separation between the two peaks is larger than for Mn I and Mn II. For Li species, the presence of two peaks is observed on a large time scale (up to 620 ns), while for Mn II the peaks can be distinguished only up to 320 ns (see Figure 6.9). In general, the first peak follows a linear behavior in time, while the second peak is attenuated due to the interaction with the background gas and probably with the plume species.

Further on, we estimate the maximum plume broadening during expansion in the background, using the plume imaging data. Plume expansion in background gas has been often described by a hemispherical blast wave model [74], with R and Z as minor and major axes of the hemisphere. The parameter Z (see insert Figure 6.10 a) was calculated as the distance between the interface of the two peaks and plume front position, which corresponds to the larger expansion of the plume along the expansion axis. The plume front position was defined as the distance at which intensity attains 10% from the maximum value. The full width of half maximum (FWHM) of the distribution (see Insert Figure 6.10 b) was used to compare the expansion of different species. The R(t) parameter was calculated by drawing the transversal profile at the interface. The temporal evolution of the lateral and longitudinal dimensions of the hemisphere, R and Z parameters, are shown in Figure 6.10.

At early stages of plume expansion (t< 220 ns) no significant difference between different plume species can be observed. After 220 ns, the broadening corresponding to Li I species increase

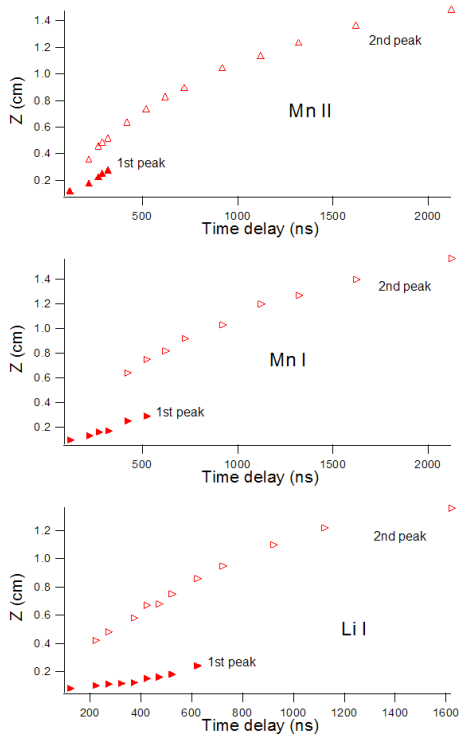

Figure 6.9: The temporal evolution of the plume peaks created during plume expansion in background gas, at a pressure of 20 Pa O_2 and at a laser fluence of 2 Jcm^{-2}. The profiles correspond to the Li I species, Mn I species and Mn II species.

faster, followed by Mn I and Mn II species. The expansion is the largest for the Li I species, followed by the Mn I and Mn II species (see Figure 6.10 down).

The transversal broadening of the plume component for the different species is shown in Figure 6.10 up. A linear increase in time is observed for all plume species until around 800 ns, with a more pronounced increase of Li compared to Mn II and Mn I. After 800 ns, the plume expansion reaches a plateau, which suggests a plume stopping effect. It is noteworthy to mention that the longitudinal dimension of the Li plume is larger than for Mn I and Mn II profiles, suggesting that the excited Li species are present over a larger volume.

The velocities derived from plume imaging and emission spectroscopy are tabulated in Table 6.3. The velocities of the plume front in vacuum are comparable with the velocities in background gas for the linear region.

6.1.4 Discussions

Optical emission spectroscopy of the excited species indicates that the plume dynamic is strongly influenced by the background pressure. There is a good agreement between the velocities derived from emission spectroscopy and plume imaging data for Li species, while the velocities derived

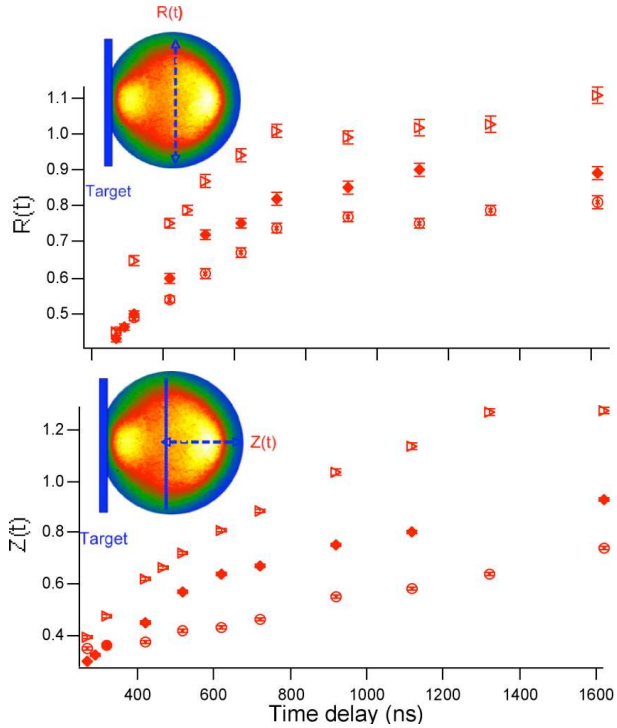

Figure 6.10: Transversal Z(t) and longitudinal R(t) profiles of the hemispherical plume attributed to Mn I (marker •), Mn II (marker ⊗) and Li I (marker ▷) species. Measurements were performed at 20 Pa O_2, with typical error bars included.

for Mn species deviates slightly.

The emission spectroscopy shows that Mn I species exhibit a lower velocity than Mn II species. Also Li I exhibit a higher velocity than Mn I, but Li I is still comparable to Mn II (ionic species). No excited ionic Li species are detected within the analyzed range, suggesting that only neutrals Li are observable in the ablation plume. The emission lines were too low to be detected in our scanning range from 300- 900 nm, although mass spectrometry analysis has shown that Li ions are major component of the plume [75].

The observation that ions are faster than neutrals agrees with previous reports [62], and can be explained by the creation of a double layer in the plume in which ions are accelerated between

Table 6.3: The ablated species velocities calculated with plume imaging.

Species	Velocities in vacuum	Velocities at 20 Pa O_2 (free flight region)
Li I	3.3 ($\pm$0.01) $\times$ 10^3 m/s 2.8 ($\pm$0.02) $\times$ 10^4 m/s 1.8 ($\pm$0.01) $\times$ 10^4 m/s	2.31 ($\pm$0.04) $\times$ 10^4 m/s
Mn I	1.8 ($\pm$0.02) $\times$ 10^4 m/s	1.89 ($\pm$0.01) $\times$ 10^4 m/s
Mn II	2.07 ($\pm$0.02) $\times$ 10^3 m/s	2.09 ($\pm$0.01) $\times$ 10^4 m/s

electron- rich layer and electron- depleted layers.
In background gas the species velocities are reduced because of the scattering with the gas molecules. Emission intensity profiles narrow in the background gas, suggesting that the plasma plume is confined during expansion due to the presence of background gas.
The plume imaging data show a free expansion of the plume in vacuum. In the presence of the background gas, the plume structure develops a double peak distribution: one is mainly due to the interaction of the plume species with the background gas, while the second one is due to the fast species which travels almost collisionsless. The shock wave created during expansion in gas follows a time dependence of $t^{0.43}$, which is in agreement with the SKW model and with other literature reports for this pressure range [62], [**?**], [10], [66].
The behavior of the Li species in the plasma plume is complex and several studies on Li atoms dynamics in a plume have been reported in the literature. Fast imaging experiments on $LiNbO_3$ indicates that Li species expand on a larger volume than the remaining plume species, but no detailed analysis of the plume expansion has been performed [**?**].

Plume expansion in vacuum

The Li I and Mn II species (velocities derived from emission spectroscopy) travel at similar velocities in vacuum, while the Mn I species are slightly slower. The emission intensity of Li I species decay at much later times compared to the Mn I and Mn II species, agreeing with the plume imaging data. The emission spectroscopy data have shown the presence of the Li I species on a double time scale (up to 820 ns) compared with Mn I and Mn II species. In order to characterize the emission temporal evolution, the radiative lifetime, defined as the time during which the excited state emission will decay collisionless by a factor of e^{-1}, needs to be considered. The radiative lifetimes of Li I species is $\sim$ 3 times larger than Mn II, and $\sim$5 times larger than Mn I. The observation of plume species for a few hundred ns while their lifetimes ranges in tens of ns indicate that excitation processes occur during plume expansion. Most probably ($Mn^+ + e^-$) recombination and collisional excitation mechanisms allow detection of Mn I at later times. The emission intensity arising from Li species can be detected at times larger than 820 ns. The radiative lifetime of Li (27 ns) cannot account for the maintained emission intensity, which suggests that excitation process occur in the plume even more complex and pronounced than in the case of Mn.
The Li species intensity is observable over a long time and length scale (Figure 6.4). The vacuum plume imaging data shows after few hundred ns a free expansion with the plume structure developing at least three peak distributions. The fastest peak, with a velocity around (1.8×10^4 m/s) is observed at the plume front, the second plume distribution tends to follow a similar behavior than the Mn I and Mn II, while the third distribution (next to the target region) has a velocity of 3.3 ($\pm$0.01) $\times$ 10^3 m/s. Possible processes that affect the plume expansion in vacuum

will be discussed below.

The presence of a fast component in the plume indicates that mainly Li species are found at the plume leading edge, while the rest of the plume consists of light and heavy particles mixture (O, Li, Mn). Considering that the plume species desorb following a Maxwell Boltzmann distribution [**?**] with the same temperature T_0, then the mean thermal velocity given by the equation 6.1:

$$v_i = (\frac{8 \times k \times T_0}{\pi m_i})^{\frac{1}{2}} \tag{6.1}$$

where m_i is the corresponding mass species. The studied material $LiMn_2O_4$ contains a mixture of three species with a mass ratio Li: O: Mn of 7: 16: 55. Assuming that all species have the same temperature, T_0, under laser irradiation, then the lithium species would acquire higher velocities than the manganese species. This model is in agreement with our observation that at early times the plume front consists mainly of light particles.

During plume expansion, multiple scattering between plume species may occur. Collisions between Li and Mn species result in a slightly deceleration of the Li plume species to a velocity comparable with Mn velocities, resulting in the formation of a second plume component.

The third plume component is observed at a 620 ns delay time and at the surface of the target. The presence of the third component at the ablation point on the target cannot be attributed to the plasma expansion but rather to other material related processes. It was previously observed by LIF a delayed emission of the Li I species during laser ablation of a $LiNbO_3$ target.

[76]. The delayed component was observed between 0.5 and 2 um, while in our experiments occurs at around 420 ns. Possible differences can be attributed to the material properties or different observation techniques. The lithium species form a large contact area with the target surface which is observed from 620 ns to 920 ns (see Figure 6.4 a).

The high velocities of the Li species compared to Mn species may be one main reason for the high Li deficiency in vacuum (in addition to- resputtering), as the high velocity light elements may not ″remain″ at the substrate. In addition, the large lateral expansion and delayed emission may contribute to the observed lithium deficiencies.

Plume expansion in 20 Pa O_2 background

Plume dynamics analysis in 20 Pa O_2 background are of significant interest because the Li content increase in thin films with increasing pressure, reaching a maximum around 20 Pa O_2; however the films are still Li deficient. A larger angular distribution of the all species in the plume would result in thinner films (lower growth rate) compared to film deposited at lower pressures. Angular differences of Li in the spatial distribution versus Mn in the plume at this pressure should be again observed in the average films composition, i.e. a different Li/Mn ratio component to the target.

Time resolved i- ICCD images of the expanding plume in 20 Pa oxygen pressure allowed detection of plume splitting and a better understanding of plume dynamics. At the initial stage a spherical plume expansion is observed, similar with the vacuum conditions. As the plume expands into the background gas, the gas will be pushed away. As a result, both gas and plume are compressed, resulting in the formation of a shock wave. The two peak distributions originating from collisions of gas- plume species, are observed at times near 220 ns (see Figure 6.7-6.8). The first peak, assigned to the free expansion of the plume species, exhibits a linear time dependence. The second peak could be fitted with the SKW model and the plume front shows a $t^{0.43}$ time dependence.

In background gas, the mean free path of the plume species is considerably reduced due to collisions with background molecules. The mean free path of the species 1, (with a velocity much higher than thermal mean velocity), in a buffer gas with species 2, is given by equation 6.2:

$$\lambda_i = \frac{k_B \times T}{\pi P d_{12}^2} \tag{6.2}$$

where k_B is the Boltzmann constant (1.38×10^{-23} J/K), T is the temperature of the gas, $d_{12}=(d_1+d_2)/2$ is the impact factor (where d_1 and d_2 are the diameters of the species 1 and 2). The estimated values of the mean free path of Li, Mn and O species in 20 Pa O_2 are summarized in Table IV, together with the corresponding atomic masses. The data shows that all species have a mean free path in the order of few mm, at a given pressure of 20 Pa O_2. The ratio λ(Mn)/ λ(Li)$\sim$1.1 indicates that Li and Mn species have a comparable collision probability during expansion in the O_2 background gas. The mass ratio of m(Mn)/m(Li)$\sim$8 suggests that a large angular distribution of Li compared to the Mn species is possible, which is in agreement with the experimental observations. The mean free path of O in the background gas is the highest from all plume species, λ(O)/ λ(Li)$\sim$ 2.4. The calculated mean free paths are much lower than the observed expansion of the ″fast peak″, suggesting that the species undergo already collisions.

The scattering cross sections of the species were determined assuming that the first peak of the plume travels almost without collisions with the background gas molecules. Thus the integrated signal at a given distance can be defined as:

$$N_g = N_0 exp(-n_g \sigma d) \tag{6.3}$$

where n_g (cm^{-3}) is the gas density, σ (cm^2) is the collisional cross section and d is the observation distance [77]. The calculated (elastic) scattering cross sections of the species are summarized in Table 6.4. The scattering cross section of Li and Mn species with gas molecules are similar, i.e. the order of 10^{-15} cm^2. The calculated values are comparable to values (2.3×10^{-16} cm^2)

obtained for $YBa_2Cu_3O_{7-x}$ species at background pressure of 40 Pa O_2, estimated from the total ion yield [78]. The experimental data can be compared with the theoretical values predicted by the kinetic theory model, in which the cross section can be estimated using the equation:

$$\pi(R_p + R_t)^2 \tag{6.4}$$

where R_p and R_p are the radius of the projectile and target particles, respectively [70]. We observe an excellent agreement between the theoretical and experimental values (included in Table 6.4). The calculated scattering cross sections are in the range of $\approx 10^{-15}$ cm^{-2}, with four times higher values for Li and Mn compared with the oxygen.

Table 6.4: Mean free path and scattering cross section of the Li, Mn and O species in 20 Pa O_2. The atomic mass, atomic radius and scattering cross section are also included.

Species	Atomic mass (amu)	Radius ($\AA$)	λ_1(cm)	$\sigma(10^{-15}\text{cm}^{-2})$ Theoretical	Experimental
Li	6.94	2.05	1.8	4.65	4.7(±0.4)
Mn	55	1.79	2	4.05	3.6(±0.5)
O	16	0.65	4.4	-	-
O_2	32	1.8	-	1.8	1.85(±0.4)

The mean free path of the particles is reduced from few cm in vacuum to a few mm in presence of a background gas. Theoretical simulations have shown that under conditions when the mean free path of the species is approaching the plume dimensions, a compression of both plasma and gas occurs, which results in shock wave formation [**?**]

The plume length estimated using the adiabatic expansion can be described by the equation 6.5 [79] :

$$L_p = A[(\gamma - 1)E]^{(1/3\gamma)}P^{(-1/3\gamma)} \tag{6.5}$$

where A is a geometrical factor which depends on the expansion geometry, where γ is the specific heat ratio of the vapour (ablation target), E is the laser energy per pulse, P is the ambient gas pressure, and V = $v_0 \times \tau \times$spot size (τ is the pulse duration, v_0 initial velocity). With γ=1.4 [80] and P=10^{-4} Pa, velocities in vacuum v_0=(0.65-1.8 $\times$ 10^4 m/s), τ= 34 ns, a spot size of 1 mm^2 and A= 1.5, we obtain a plume length L_p= 33.3 (± 5) mm. If we consider a distance to substrate distance of 40 mm (typically used for the films growth), we can conclude that the films growth occurs at the limit between plume expansion and diffusion regime. The species suffer multiple scattering in the plume, a substrate placed at 40 mm from the target will correspond to around 22 mean free paths for the Li species and 10 mean free paths for O species.

The mean free path of plume species in the background gas is reduced, resulting in plume splitting. At later times, the plume front slows down and the plume density tends to be in equilibrium with the gas density. The emission intensity profiles reveal a maximum near the front edge of the plume at later times, suggesting a contact front formation between the plume and background gas [81]. In the final stage of plume expansion, the two plume peaks converge, suggesting that all species are ″stopped″ by collisions, i.e. the species diffuse into the background gas.

The emission intensity profiles along the plume expansion axis show a different dynamic for Li species and the Mn and O species. During expansion in gas, a larger separation for Li species was observed in the plume splitting compared with the Mn and O species. As mentioned previously, in the case of Li expansion in vacuum a delayed component of the Li species is observed. The studies of Li expansion in vacuum can therefore elucidate the secondary peak plume strongly observed for the Li species at a 420 ns delayed time. The two peak components observed at 420 ns can be therefore attributed to the delayed and normal Li emission which have collided with the background gas.

The emission profiles studies at different delay times have shown the plume center moves closer to the plume front, suggesting a strong deceleration of the plume by the background gas. The effect is more pronounced for the Li species, indicating a higher scattering degree at the plume front. We can therefore conclude that the background atmosphere is the most important factor in moderating the kinetic energy of the species, preventing the re- sputtering of the films. The gas slows down the Li and Mn species and no considerable differences between the plume front and the rest of the plume can be observed.

Using a simplified hemispherical model the scattered plume components were analyzed (Figure 6.10). The longitudinal expansion shows two distinct regions: in the first stage the expansion occurs almost linear in time, while above 800 ns a plateau regime is reached.

The plateau regime indicates that the plume density reaches the gas density, corresponding to the plume stopping. The plume stopping marks a transition form a plume thermodynamically coupled with the gas to the diffusion regime [10]. After 200 ns a larger expansion of the Li species is observed compared with the Mn species, indicating that the Li species expands with higher velocity.

The most considerable difference between the plume species consists in plume angular broadening. The maximum plume broadening in background gas is observed at the interface between the two plume components (see Figure 6.10). The transversal profiles of the plume show an increase in plume broadening in time. The increase is predominant for the Li species compared to the Mn species. After 1600 ns, the broadening of Li species occur on a double scale compared with the Mn I species, reaching a maximum plume broadening of around 1.2 cm, while the expansion of Mn species scales between 0.6 and 0.8 cm. Since the calculated mean free paths of the Li

and Mn species are similar, the main difference between plume species can be attributed to the large angular scattering. Thus, the amount of neutral Li species generated during the ablation process are distributed over a larger angular volume, with a considerable angular broadening, while the Mn atoms are more confined to a more forward direction. The significant scattering of the light particles in the plume and with the gas molecules inducing a large plume broadening can explain the Li deficiency observed in the growing films. The data suggests also that a congruent transfer of the light elements is impossible, suggesting that deficiencies of light elements can only be overcome by applying targets with an excess of the light element.

6.1.5 Conclusions

Time resolved emission spectroscopy measurements have been performed on the plume induced by laser ablation of a $LiMn_2O_4$ target, showing faster velocities for ionic Mn species compared to the neutrals species.

In vacuum, the Li I plume emission is very broad compared to the other species and the plume dynamic is rather complex, consisting in (at least) three plume components. After few hundred nanoseconds, a fast Li component is observed at the plume leading edge, indicating a higher velocity of the light species in the plume. However, part of the Li species are slowed down during collisions in the plume with the Mn and O species inducing a second plume component which travels at a similar velocity with the rest of the species. And last, a third plume component observed at the target surface can be attributed to a delayed emission of the Li species from the target. The fast expansion at the Li species in vacuum compared with the Mn species lead to an elongation of the plume emission along the expansion direction after few hundred ns, while the emission of Mn species is spherical.

Moreover, when a background gas is applied, the plume species are slowed down due to collisions with background gas molecules. Plume expansion in 20 Pa oxygen can be fitted with the blast wave model and the plume front shows a $t^{0.43}$ time dependence. The free plume component is faster in the case of Li compared with the Mn I and II, but at later times the plume front consists of all species. The Li I plume center moves closer to the leading edge of plume, suggesting a strong Li species deceleration in the background gas. The major difference between plume species is observed on the angular spread of the Li species, which is almost twice larger than for the Mn species. It was found that the Li and Mn species have the same collision probability, showing that the large difference is due to a more pronounced scattering of the light masses in the plume. The deviation from the ideal stoichiometry (-5% Li) of the films grown at a background pressure of 20 Pa O_2 can be explained by the large dissipation of Li in the plume. However, the large Li distribution in the plume is only of minor importance compared to re-sputtering phenomena observed at low pressures, but it seems to explain (together with delayed

lithium emission) why it may be impossible to deposit Li containing films without deficiencies.

6.2 Ns and Fs Laser Ablation of $La_{0.6}Ca_{0.4}CoO_3$: Comparison Between Plume Dynamics

6.2.1 Motivation

Fs laser- material interaction is a research topic briefly explored until now due to the recent development of reliable fs lasers. One of the main drawbacks in ns laser deposition consist in the presence of droplets (molten particles) at the films surface. A possibility to limit thermal effects is using ultrashort laser pulses [82]. The ultrashort pulse irradiation appears to produce less damage compared to the ns laser pulse. The plume formation mechanism appears to the simplest for fs laser irradiation. The time scale for plume formation is proportional to the pulse length. Plume heating, specific to the ns laser ablation and caused by the photoabsorbtion processes of the plume are eliminated for fs laser pulses.

Emission of neutral atoms, singly and doubly charged ions, as well as neutral and ionic clusters has been reported for fs laser ablation [66]. Recent reports on laser ablation of silicon have also shown the possibility to create nanoparticles with fs ablation [65].

The growth of polycrystalline $La_{0.5}Sr_{0.5}CoO_3$ thin films by femtosecond laser ablation has been previously successful realized [83].

In previous studies in our group $La_{0.6}Ca_{0.4}CoO_3$ (LCCO) films have been deposited with ns laser, demonstrating the possibility to control film crystallinity by tuning the experimental parameters. Films with desired stoichiometry and low surface roughness were obtained [37]. The $La_{0.6}Ca_{0.4}CoO_3$ (LCCO) materials can be applied as a bifunctional catalyst for metal- air batteries, e.g. rechargeable zinc/air batteries [84].

Recent studies have shown that using a fs laser the films surface consists mainly of large grains with an average particle size of $\sim 1\mu$ m, while with the ns pulse the surface roughness is below 1 nm.

The LCCO films grown with the ns laser shows a highly epitaxial orientation (00l), while the films grown using the fs laser showed various phases, such as CaO, CoO, CaO_2 and Ca_2O_3. Furthermore, the overall films composition shows a high oxygen deficiency and a ratio Co/O smaller with 30% compared to films grown with a ns laser. Using a ns laser pulse (248 nm, 20 ns pulse), a stoichiometry of the film $La_{0.63}Ca_{0.34}Co_{0.97}O_3$ was obtained, while the films grown by fs ablation (248 nm, 500 fs pulse) the stoichiometry was $La_{0.69}Ca_{0.31}Co_{0.69}O_{2.7}$. Thus, the LCCO films grown with a fs laser exhibit a strong depletion of Co and contain various secondary phases.

The Co and Ca deficiencies in the grown films may be caused by processes similar to the processes identified for Li in $LiMn_2O_4$. We study therefore the plume generated by fs (248 nm, τ= 500 fs) and ns (248 nm, τ= 20 ns) laser ablation of the LCCO target in vacuum and in background gas.

Optical emission spectroscopy and plume imaging are used to analyze the plume in vacuum and a deposition pressure which results in high quality films for ns ablation (60 Pa O_2). The aim is the correlation of the internal plume structure with the film composition.

6.2.2 Optical emission spectroscopy studies in ns and fs ablation

The temporal profiles of the plume emission were taken at various distances from the target. The LCCO spectra presents many lines related to the contribution of neutrals, single, double, triple ions of La, Ca, Co and O. The investigated emission lines are summarized in Table 6.5.

Table 6.5: Emission lines and lifetimes of the investigated plume species.

Species	Wavelength (nm)
La I	576.1 nm
La II	394.8 nm
Ca I	585.7 nm
Ca II	396.7 nm
Co I	355 nm
O I	777.6 nm

Figure 6.11 shows a comparison between the emission spectra taken at different delay times for ns and fs laser irradiation in presence of 60 Pa O_2. The emission lines corresponding to the fs plume are narrower and weaker compared to the ns ablation, which can be at least partially explained by the lower ablation rate for fs irradiation.

Below 120 ns, close to the target region, the emission spectra corresponding to the ns ablation consists in a continuum signal overlapping with the emission lines of the excited species (see Figure 6.11- left). The continuum contribution to the overall emission spectra is most probably due to the presence of excited electrons in the plasma [85]. At later times, e.g. 920 ns, a series of intense lines can be distinguished.

At early times, e.g. t< 120 ns, the continuum contribution to the emission spectra induced by fs ablation is considerable reduced (see Figure 6.11- right), suggesting that the continuum is formed in the case of ns pulses by heating of the plume or by partial absorption of the laser pulse. At a delay time of 920 ns broad bands corresponding to the formation of CaO (548.8 nm) [66] diatomic species are observed. The diatomic intensity emission decays at distance larger than 3 mm.

Figure 6.12 shows the temporal evolution of the Co I species in the plume induced by ns ablation and fs ablation. In the case of ns ablation, the emission intensity signal decays at larger distances and longer delay times compared to fs ablation. In fs ablation, the plume emission intensity drops

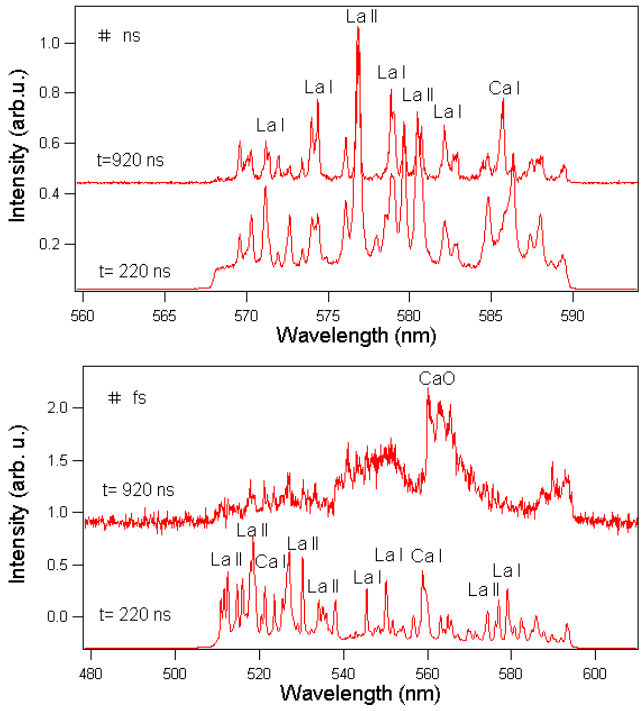

Figure 6.11: Emissions spectra of the plume induced by ns and fs laser ablation of the $La_{0.6}Ca_{0.4}CoO_3$ target. The emissions spectra were collected at the target surface and in presence of 60 Pa O_2.

to zero after 600- 700 ns, while in ns ablation a plume ca be observed for 1200 ns. Irradiation with a ns laser results in a larger initial intensity compared to fs ablation due to the larger ablation rate. The emission decays therefore at larger distances from the target.

Using the temporal and spatial distribution of the excited species, the average velocity of the species were determined. The velocity of the ablated species- calculated from the linear dependence distance versus delay time - are summarized in Table 6.2.2.

The values obtained for ns ablation in vacuum reveal that the velocity of the species increases proportional with the charge, e.g. from Ca I to Ca II and to Ca III. The same trend is observed for La species. Similar observations were reported elsewhere and explained by the ambipolar diffusion mechanism which has been discussed before and which is often described in literature [66]. According to the model, the electrons posses the highest velocity, followed by triple charged, double charged, single charged and neutral species. As expected, the calculated velocities at 60 Pa O_2 are lower compared with vacuum due to the collisions with the gas molecules.

In fs ablation the positively charged species exhibit as well larger velocities than the neutrals species (see Table 6.2.2). It is noteworthy that the Co I species exhibit a larger velocity compared to Ca I and La I species, but comparable with Ca II species. As expected, the velocity of the species are reduced in the presence of 60 Pa O_2 pressure. We do not observe a major difference

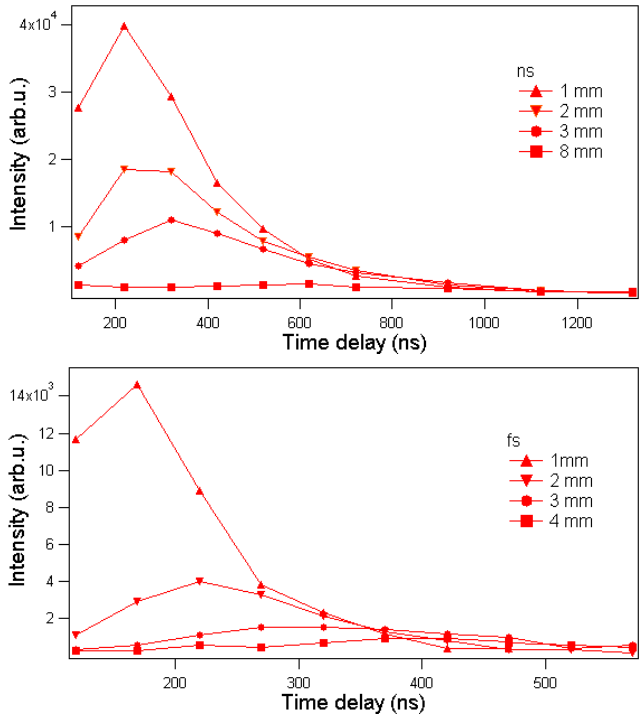

Figure 6.12: Spatial and temporal evolution of emission intensities in vacuum corresponding to the Co neutral species for ns and fs laser ablation.

between the velocities of the species in the fs ablation compared to the ns laser ablation, but it appears that the species generated by ns ablation are slightly faster, especially in the presence of the background gas. The intensity of the emission intensity lines in the laser induced plume decays at 3 mm from the target. The temporal and spatial evolution of the emission lines is therefore limited with the optical emission spectroscopy technique. The intensities cannot be compared directly (fs vs ns), as the ablation rate in fs ablation is lower than the ablation rate in ns ablation.

6.2.3 Time resolved plume imaging in fs and ns regime

6.2.3.1 Vacuum

Plume imaging analysis allows the detection of the plume dynamics and internal plume structure over a large scale (3 cm in our experiments). Typical images of the Co I species expanding in vacuum during ns and fs laser ablation are shown in Figure 6.13. As shown, the plume shape differs considerably between ns and fs laser ablation. In vacuum, the plume induced by ns ablation has a spherical shape, while the plume induced by fs laser ablation has an elliptical shape. An elliptical shape of the plume induced by fs ablation has been reported previously also

Table 6.6: The average plume species velocities obtained from emission spectroscopy.

	ns		fs	
Species	Vacuum	60 Pa O_2 (free flight region)	Vacuum	60 Pa O_2 (free flight region)
Ca I	1.8×10^4m/s	1.4×10^4m/s	9×10^3m/s	-
Ca II	2.3×10^4m/s	1.8×10^4m/s	1.5×10^4m/s	7.2×10^3m/s
Ca III	2.9×10^4m/s	2.2×10^4m/s	-	1.4×10^4m/s
La I	-	1.4×10^4m/s	1.1×10^4m/s	1.2×10^4m/s
La II	2.3×10^4m/s	2.3×10^4m/s	1.9×10^4m/s	7.2×10^3m/s
Co I	1.4×10^4m/s	-	1.4×10^4m/s	7.8×10^3m/s

for $La_{0.5}Sr_{0.5}CoO_3$ [86].

Santagata et al. [65] proposed a simply quantification of the plasma angular distribution. Considering I_0 as the intensity at an initial detection angle θ= 0, the intensity at given angle θ with respect to the normal to the surface is given by the relation:

$$I_\theta = I_0 \times cos^n(\theta) \tag{6.6}$$

where n is the fitting parameter which defines the plume anisotropy. A value of n= 1 corresponds to spherical distribution of the plume, while n> 1 corresponds to a more elongated plume.

The transversal and longitudinal profiles of the plume, denoted by the a and b axes, respectively are also included in Figure 6.13. The a and b parameters were determined from the width of the lines taken at a position where the maximum intensity decays at 20%. By fitting the line profile with the function defined by the equation 6.6, n= 0.89± 0.2 was obtained for the ns- plume, and n= 1.8± 0.2 was obtained for fs- plume. This quantifies the visual appearance of the more elongated shape in fs laser ablation compared to the ns irradiation induced plume.

Filtered i- CCD images corresponding to La and Ca ions are shown in Figure 6.14. The images present the plume expansion in vacuum of the ns ablated species (a) and fs ablated species (b) with the corresponding delay times. The ns plume has a spherical shape while expanding freely into vacuum. Comparing the plume images at a delay time of 920 ns (on similar scale), we observe that the fs plume front travels a longer distance compared to the ns plume. The fs plume exhibits a considerable elongation along the expansion direction which is most probably caused by the high kinetic energy of the fs ablated species.

The plume front position was plotted as a function of the delay time in order to estimate the front velocities for different ablation conditions. The plume front was defined as the distance at which the emission intensity attains 10% of its maximum value. From the slope of the linear dependence, the plume front velocities were calculated. In ns ablation a plume edge velocity of

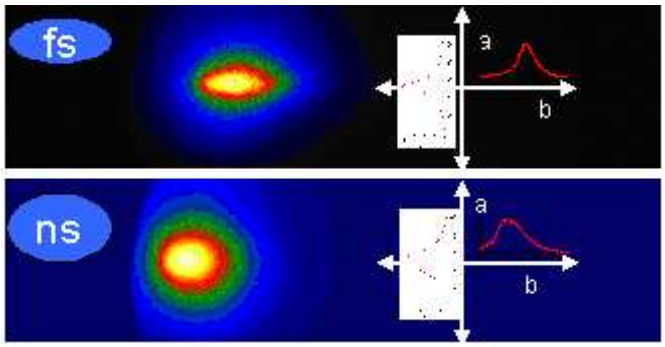

Figure 6.13: Schematic of the a and b axes of the plume corresponding to Co I species taken at delay time of 320 ns for ns and fs ablation.

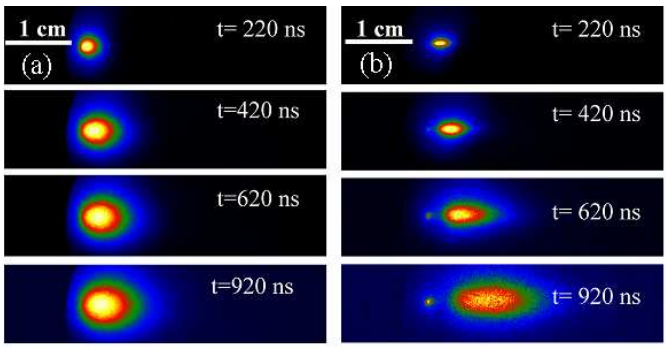

Figure 6.14: Filtered i- CCD images of the optical emission induced by ns (left) and fs (right) laser ablation, allowing the detection of both La II and Ca II species.

1.6×10^4 m/s and for fs ablation a plume front velocity of 2.5×10^4 m/s, which reveals that in vacuum the fs plume has twice velocity of the ns plume front.

The larger values obtained in fs ablation compared to ns ablation are not in agreement with the emission spectroscopy data. This is probably due to the different analysis. For emission spectroscopy, the maximum intensity of a given species at a given distance is used, while the plume front, determined by the position where the maximum intensity decays at 10

The temporal evolution of plume emission in vacuum corresponding to Co I species in presented in Figure 6.15. The ns plume emission corresponding to the Co I species has a spherical distribution, while for fs ablation the emission assigned to the Co I species expands in a more elongated shape (similar with previous observations). At a delay time of around 920 ns, the plume emission exhibits a long tail (see figure 6.15 b) for fs ablation.

The transversal profiles of the plume were used to investigate the internal plume structure, such as plume splitting and plume oscillations. The profile lines of Co I induced by fs ablation are shown in Figure 6.16. The emission intensity profiles consist of two main distributions which can be well resolved at a delay time of 920 ns. The first distribution, closer to the target surface,

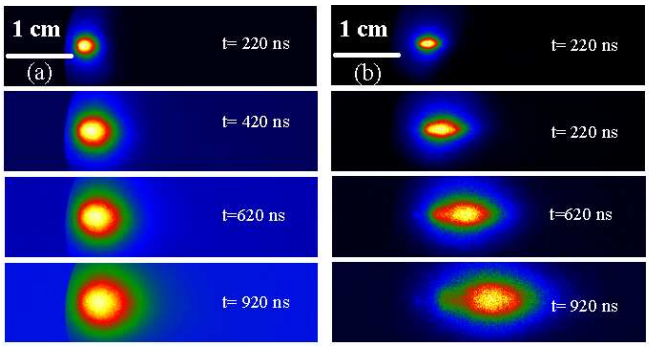

Figure 6.15: Wavelength filtered i- CCD images using a narrow band width filter which allows detection of the Co I species. Data collected in vacuum using a ns (a) and fs (b) laser as a irradiation source.

is quite slow, while the second distribution exhibits a maximum peak at larger distances from the target. The velocities of the first and second distributions are 6×10^3 m/s and 1.4×10^4 m/s, respectively.

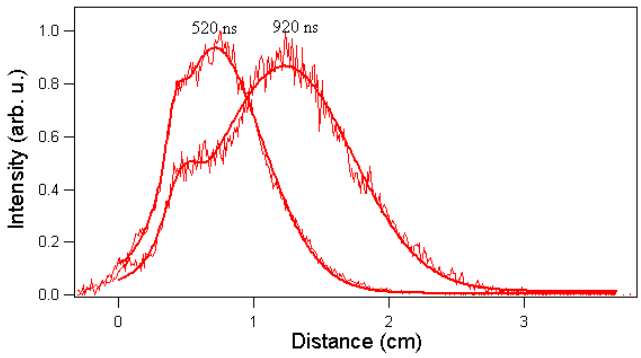

Figure 6.16: Fs laser ablation in vacuum: Profiles along the expansion direction of the Co I species at a delay time of 520 ns and 920 ns. The Gaussians are also included.

A comparison between the line profile of the La II & Co I versus Co I and La II & Ca II are illustrated in Figure 6.17 (a) and (b), respectively. The longitudinal profiles of the images were fitted using Gaussian functions. The peak observed at the target surface (constant in time) can be assigned most probably to reflections from the target surface. Comparing the intensity profiles in 6.17 (a) and (b) we observe that Co I species have the widest distribution.
Furthermore, the emission profiles are broadener for the Co I containing species, suggesting that the double peak population of the Co I species contribute to the increase in the broadening of the distribution.
The maximum emission intensity and its corresponding delay time were plotted as a function of the distance from the target (Figure 6.18 a and b). In the case of La II and Ca II species,

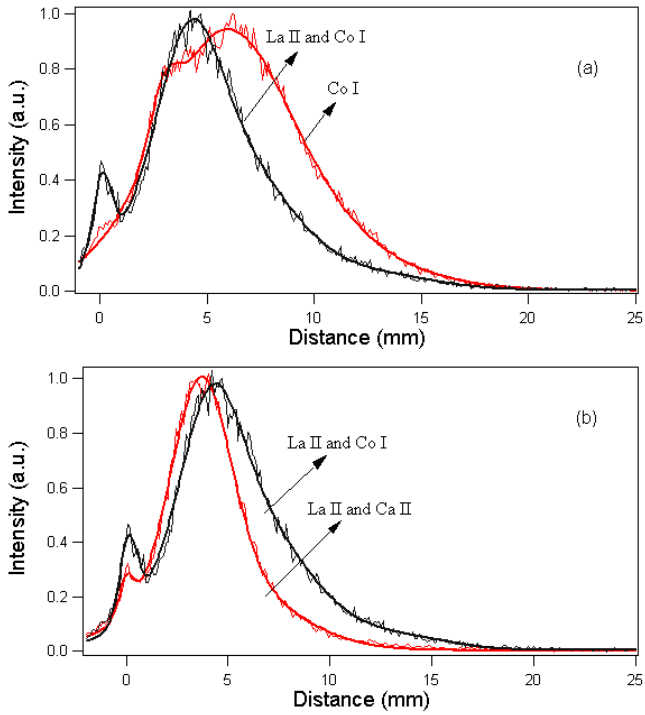

Figure 6.17: Normalized intensity profiles of the plume induced by fs laser ablation in vacuum. The intensity profiles fitted with Gaussians function are included. The profiles correspond to the plume emission at the delay time of 520 ns.

the maximum intensity decays at around 8 mm from the target, while the Co I species exhibit a tail which extends up to 14 cm from the target (Figure 6.18 a). The delay time of the La II and Ca II species increases faster increase up to 8 mm from the target, suggesting a faster decay (in space) of these excited species.

The Co neutrals exhibit two velocity distributions during expansion in vacuum. The slow component develops temporally and spatially similar with the rest of the plume species, such as neutrals and ions, while the second plume has a two times greater velocity. As the lifetime of the Co I excited species (355 nm) is relatively short (few ns), plume collisions leading to excitation and emission should take place on a similar time scale as for the rest of the plume species. If the electron- ion recombination processes in the plume (Co II + $e^- \longrightarrow$ Co I) would be responsible for the fastest plume component, the the Co II species would be initially much faster than the La II and Ca II species, which is not likely.

Two plume components have been observed during laser ablation of a BiSrCaCuO target and the formation of the second species has been assigned to processes such as the dissociation of the cluster species during plume expansion or due to the electron impact processes [85]. The presence of clusters in the plume induced by femtosecond ablation has often been reported [87] and the emission of neutral and cationic silicon clusters has been studied for femtosecond laser ablation of silicon in detail [88]. However, the emission of clusters in the plume is observed on

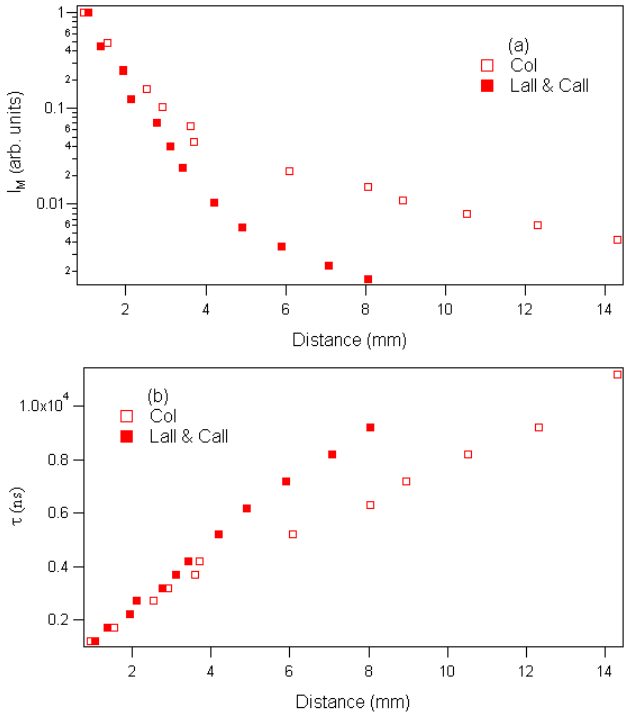

Figure 6.18: Maximum emission intensity (a) and the corresponding delay time (b) versus the observation distance for Co I and La II & Ca II pair. Data were recorded in vacuum.

a time scale of tens of microseconds. Unfortunately, our experimental data were only recorded up to a time scale of 2μs, which is relatively short for the observation of clusters in the plume. Anyhow, we observe the second Co distribution on a time scale which appears as too short for clusters formation, and it is therefore not likely that the Co I species are formed during the dissociation of the Co containing clusters.

6.2.3.2 Plume expansion at 60 Pa O_2

Figure 6.19 shows the plume front evolution corresponding to La II and Ca II species in vacuum and at a background pressure of 60 Pa O_2 for ns laser irradiation. From the plots of the linear dependence in vacuum and in the free flight region in gas, the plume front velocities were found to be 1.9 $\times$ 10^4 m/s and 1.7 ($\pm$ 0.01)$\times 10^4$ m/s, respectively. After 620 ns, the plume front is decelerated in agreement with the blast wave model, e.g. $\sim t^{0.47}$ (see Table 6.2.3.2).

The plume expansion at 60 Pa O_2 corresponding to the La II and Ca II species is shown in Figure 6.20. The plume splitting effect is visible at 420 ns delay time (see Figure 6.20 a). The plume splits into two components, the first component travels almost collisionless, while the second plume component is decelerated by multiples scattering with the other plume species and background gas molecules. The plume emission intensity for fs ablation is smaller compared to ns plume due to the fact that there are no additional interactions between the laser and the

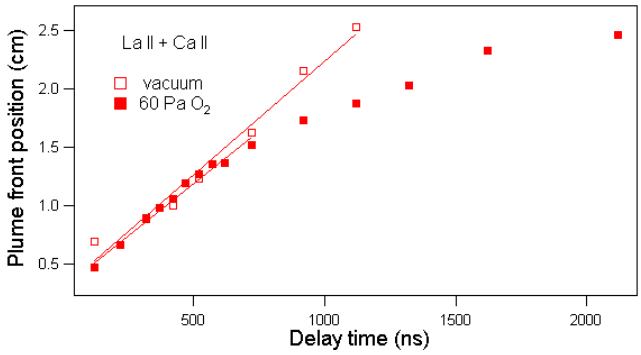

Figure 6.19: Ns laser irradiation: The plume front position evolution vacuum and at 60 Pa O_2 for La II and Ca II species. The solid lines represent fitting of the liner dependence.

plasma plume, but also due to the lower ablation plume.

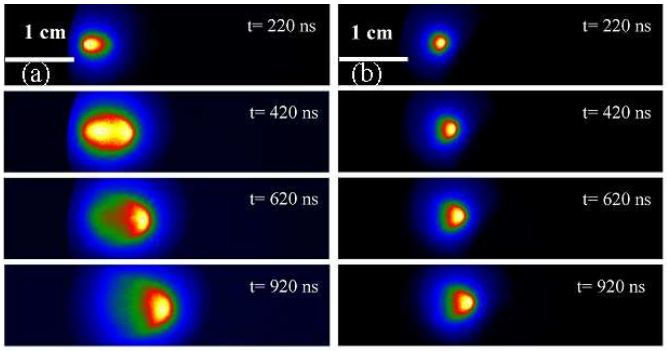

Figure 6.20: Optical emission of La II and Ca II species induced by ns (a) and fs (b) laser ablation in 60 Pa O_2 pressure.

It is noteworthy to mention that the intensity shape changes from vacuum to gas conditions, especially for fs irradiation. The plume shape is now spherical for both pulse length. The increase of the intensity at the leading edge of the plume gives the appearance that higher velocities are present, but is mainly due to the different distribution of the plasma along the expansion direction.

Furthermore, in ns ablation the plume front position shows a time dependence which is in agreement with the theoretical modelling for the shock wave propagation in gases, while the fitting coefficients (n) obtained for fs plume expansion deviates considerable from the theoretical value. We can therefore conclude that the SKW model can not be used to fit the fs plume expansion at a background pressure of 60 Pa O_2.

Plume images corresponding to the Co I species in background gas are shown in Figure 6.21. The plume emission for the fs plume is much weaker compared to the ns plume, and the plume splitting effect is less pronounced. The overall emission intensity for fs ablation is initially much

smaller than for ns ablation, with a fast spatial and temporal decay.

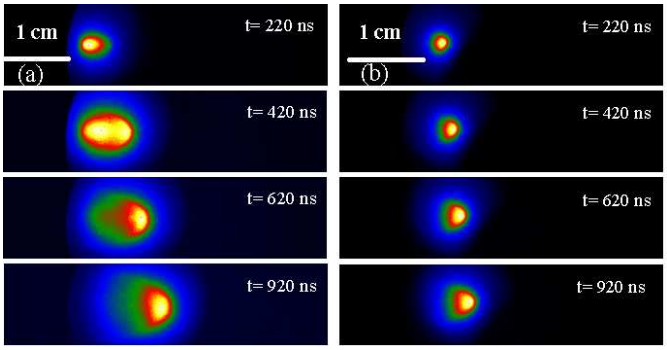

Figure 6.21: The temporal evolutions of the Co I emission during expansion in 60 Pa O_2 pressure. The i- CCD images show the plume emission induced by ns laser irradiation (a) and fs laser irradiation (b).

The velocities of the species calculated for vacuum and background conditions are summarized in Table 6.2.3.2. In the presence of a background gas all species are decelerated and the Co I species detected by fs irradiation in the background gas reveal now the same velocity as the other species. The obtained velocities do not reveal large differences for ns ablation compared to fs ablation. The velocity values of fs ablated species are comparable with the values reported for ns ablation. Therefore sputtering of the Co species from the substrate due to higher velocities should not be the origin of Co depletion in the growing films for fs laser ablation. The two different velocity distributions of Co I have only been observed in vacuum, and this can not be responsible for the Co depletion in the films deposited at aa background pressure.

Table 6.7: The plume front velocities (m/s) of the species obtained from the plume imaging data.

	ns			fs		
	Vacuum	60 Pa O_2		Vacuum	60 Pa O_2	
Species		free region	SKW		free region	SKW
La II + Ca II	1.6×10^4	1.6×10^4	$a \times t^{0.47}$	2.4×10^4	9.2×10^3	$a \times t^{0.4}$
La II + Co I	1.6×10^4	1.9×10^4	$a \times t^{0.47}$	6.8×10^3	9.2×10^3	$a \times t^{0.3}$
Co I	1.9×10^4	1.8×10^4	$a \times t^{0.47}$	2.4×10^4	8.8×10^3	$a \times t^{0.36}$
Ca I	1.4×10^4	2×10^4	$a \times t^{0.47}$	2.2×10^4	7×10^3	$a \times t^{0.45}$

6.2.4 Discussions and conclusions

The plasma expansion dynamics of the species generated by ns and fs laser ablation from a $La_{0.6}Ca_{0.4}CoO_3$ target were investigated using time resolved emission spectroscopy and plume imaging techniques.

In vacuum, the plume induced by ns ablation has a spherical distribution, while in fs ablation the plume exhibits an elongated shape, indicating a faster displacement of the plume front.

In ns ablation in vacuum, the velocity of the species increases with the increasing of the particles charge. For example. larger velocities were obtained for Ca III compared to Ca II and Ca I.

In fs laser ablation in vacuum, the Co I species exhibit two main distributions,one distribution has a similar velocity as the rest of the plume species, while the other moves with a two times higher velocity. The origin of the double distribution of the Co I species is not clear, but the observations at higher times suggest that they are not generated from the dissociation of clusters during plume expansion.

In the presence of 60 Pa O_2, which represents the optimum pressure for films growth, the ns ablated species are attenuated in time according to the shock wave model, e.g. with a $t^{2/3}$ time dependence.

For fs laser ablation in vacuum, where Co and Ca depletion in the growing films was observed, the plume front attenuation does not follow the predicted time dependence estimated by the SKW model. The plume shape in O_2 background gas is similar for ns and fs ablation.

The reasons for Ca and Co deficiencies in the case of fs irradiation in the growing films with O_2 background gas are not clear, but in the case of Co cannot be related to a larger angular distribution of the plume. Whether the slightly lower velocities found for fs (compared to ns ablation) can explain the low Co content in not likely, but the lower kinetic energy may explain the lower degree of crystallinity in the films created bs fs irradiation, because the epitaxial quality of the films is determined by the substrate temperature and kinetic energy of the species. The lower kinetic energies of the fs ablated species may not be enough to support the formation of a single crystalline phase, resulting in a a polycrystalline film.

Possible mechanisms for the losses of Co may be related to:

(i) Lower sticking coefficient of Co under the given conditions (not likely);

(ii) The different composition of the plume, which was not quantitatively determined;

(iii) Emission of Co clusters, which were not observed in our plume imaging data due to the short recording time. These clusters do not participate to the films growth, resulting in Co deficiencies.

Chapter 7

Conclusions

The aim of the work which has been presented in this research report is to understand the physics underlying the deposition and properties of manganite thin films. This includes studies on the colossal magnetoresistance effect, which has been suggested for potential possible applications in magnetic devices, and on the plasma induced by laser ablation. Pulsed Reactive Crosses Beam Laser ablation (PRCLA) has been used as a method for the synthesis of the $La_{0.6}Ca_{0.4}Mn_{1-x}Fe_xO_3$ (with x= 0, 0.2) thin manganite films.

Thin manganite films

The manganite thin films were deposited on different oxide substrates to investigate the influence of the PLD parameters, such as laser fluence, target to substrate distance, and post- annealing treatments, on the crystallography, composition, morphology and transport properties of the films.

The films deposited in a wide fluence range, i.e. 2 Jcm^{-2} to 8 Jcm^{-2}, have a similar elemental composition, but Ca and O deficiencies were observed. The RBS results reveal that films with the composition of $La_{0.7}Ca_{0.3}MnO_{3-\delta}$ are obtained from a target with a composition of $La_{0.6}Ca_{0.4}MnO_3$.

The best epitaxial quality of the films was obtained for a target to substrate distance of 4 to 5 cm. A high epitaxial quality results in a high colossal magnetoresistance (CMR) of films. Thinner films exhibit the largest CMR values, suggesting that the strain induced by the substrate plays an important role on the CMR effect.

High oxygen deficiencies in the growing films lead to a dramatic reduction of the colossal magnetoresistance (CMR) ratio. Oxygen acts as a bridge between the Mn^{3+} and Mn^{4+} ions and has therefore a pronounced influence on the double exchange interaction which is the main mechanism for the CMR. The films cooled in vacuum have the highest oxygen deficiencies and therefore the lowest magnetoresistance ratio, while the films cooled in oxygen atmosphere have a higher oxygen content resulting in a larger magnetoresistance. Further annealing after deposition at

high temperatures and long times (900^0 for 10 hours) can improve the magnetoresistance even more.

The effect of the oxygen content, which is controllable by different postdeposition treatments, on the oxidation states of the Mn species was probed by XPS (surface sensitive) and XAS (bulk sensitive). A higher oxygen content leads to an increase in the oxidation states of the Mn species, and thus to an increase of the Mn^{4+} species. This favors the hopping of electrons in the Mn^{3+}- O $^{2-}$- Mn^{4+} network, which increases the electrical conductivity and the magnetoresistance.

The hopping mechanism in the Mn^{3+}- O $^{2-}$- Mn^{4+} network was therefore tested by replacing some of the Mn ions with Fe ions. The as deposited films exhibit mixed valence states of Fe^{2+} and Fe^{3+}, inducing disorder in the perovskite structure. After annealing, only Fe^{3+} was detected. The XAS data shows a localization of the Mn 3d orbitals after Fe doping, suggesting that the Fe ions act as trapping centers for the exchange of electrons. The resulting Fe doped films exhibit a large bulk resistivity and a reduced CMR. This suggests that the mixed valence states of Mn^{3+} and Mn^{4+} is important for the CMR effect.

Plume analysis by mass spectrometry

An investigation of the plasma induced by laser ablation from a manganite target was performed to combine the studies on the ablation plume with film properties for a deeper understanding of the manganite growth by PRCLA. The spectroscopic analysis was carried out by an ion energy and mass analyzer to determine the plume species and their energy distribution. In vacuum, the plume consists of metal ions, LaO, and CaO diatomics. The ionic yield of the plume is dependent on the irradiation wavelength, i.e. for higher photon energies, a larger degree of ionization is detected.

In vacuum, the ionic species exhibit larger kinetic energies and broadener angular distributions compared to the neutral species.

The MnO diatomic species, which are considered to be important for the growth of manganites, were detected only in the presence of the oxygen background gas and N_2O gas pulse, suggesting that oxidation of Mn species is less favorable compared to the oxidation of La and Ca species.

One important aspect of the N_2O gas pulse crossing the laser plume is the formation of negative diatomic species. The O^- ions are among the most abundant species in the plume, but the formation mechanism of negative ions and their role on the properties of the manganite films is not well understood at the moment. The largest kinetic energies are observed for the positive ions, followed by neutrals and negative ions.

Alternative spectroscopic methods

The manganite films grown by PLD exhibit Ca deficiencies, which can be probably related to wider angular distribution of the light elements in the plume. To efficiently probe this

mechanism, a material which contains a very light element, e.g. Li in $LiMn_2O_4$, has been selected. Plume imaging and emission spectroscopy techniques have been used to study the plume expansion/dynamics in vacuum and in an O_2 background. The film analysis has shown that even for the optimum deposition conditions of the $LiMn_2O_4$ films, a Li deficiency is present. The plasma plume analysis reveals that Li species exhibit a larger angular distribution compared to the other plume species. It is therefore impossible to achieve a congruent material transfer by laser ablation, when light elements are contained in the target.

Furthermore, the influence of the laser pulse length on the ablation of $La_{0.6}Ca_{0.4}MnO_3$ has been studied. Laser ablation of the oxide target using an ultrashort pulse (248 nm, τ= 500 fs, but also for τ= 100 fs at 800 nm) leads to large deficiencies in the Co content, which are not present for ns ablation (248nm, τ= 20 ns). In vacuum, the Co neutral species exhibit a two component distribution, while the other plume species posses only a single distribution. The neutral Co species reveal also an unexpected velocity, which is higher than all other neutral species, but similar to the velocity of La^+ and Ca^+. The plume shape for ns ablation is spherical, while for fs ablation an elliptical shape is obtained. The plume front of the fs plume travels with a double velocity compared to the ns plume.

With a background pressure of O_2, no differences between the plume shapes induced by fs and ns ablation are observed, and no major difference between the velocities of the different ablation species were observed. The fs ablated species exhibit even smaller velocities than the ns ablated species. The observed mechanisms in ns ablation, such as large angular distribution and high kinetic energies, were not encountered for fs ablation. This suggests that the depletion of Co in the background gas is related to other reasons. A possible mechanism would be the emission of Co clusters during fs ablation which do not participate to the films growth. Our experimental data did not shown the presence of clusters in the fs plume, but further detailed experiments may be necessary.

List of Figures

1.1 Schematic of the Pulsed Reactive Crossed Beam Laser Ablation. 7

2.1 A photograph of the UHV experimental setup used in this work. On the left side (A) emission spectroscopy (1), ion gun (2), sample manipulator system (3), and load lock (4) are visible, and on the right side (B) the EQP mass spectrometer (5) and laser entrance window (6). 10

2.2 Schematic top view of the UHV chamber, showing the Laser In section, Mass Spectrometer, Ion Gun, Emission Spectroscopy, Energy Out, Gas Pulse, RF-Discharge, TMP (turbomolecular pump), Langmuir Probe and Metastable Detector. 12

2.3 Diagram of the EQP mass spectrometer. 14

2.4 The ionization section of the QMS. The recommended operating cage voltage is between +3 V and +10 V 16

2.5 The measured energy distribution of the nitrogen neutrals ionized and accelerated at different cage voltages, e.g. 3 V, 7 V and 9V. 16

2.6 The measured energy distribution of the LaO positive ions (upper graph) and negative ions (lower graph) using an energy analyzer. 17

2.7 Schematic of a quadrupole mass filter. 18

2.8 Mass spectra up to 200 amu of a NIST reference sample. 19

2.9 Scheme of the synchronization between the spectrometer and laser. 20

3.1 Schematic diagram of the AFM operating in contact mode. 23

3.2 The principle of Rutherford Backscattering. 24

3.3 The principle of Elastic Recoil Detection Analysis (ERDA). 25

3.4 The XPS emission of an electron from a core level into vacuum. 27

3.5 The XAS emission of an electron from a core level into an unoccupied level above the Fermi level. 28

3.6 The typical XAS spectrum of a solid. 28

3.7 The diagram of the XAS setup. 29
3.8 Schematic view of the four point circuit, left, and geometry of the contacts on the sample, right. 29
3.9 Schematic view of the Van der Pauw configuration used to determine the two characteristic resistances R_A and R_B. 31

4.1 Crystallographic structure of $LaMnO_3$. 34
4.2 The splitting of the Mn 3d levels into e_g and t_{2g} levels and the resulting Jahn-Teller distortion. 35
4.3 The schematic of the double exchange interaction. 36
4.4 Composition of the $La_{0.6}Ca_{0.4}MnO_3$ films deposited at various laser fluences. The relative error is 5 percent. 37
4.5 Average growth rate of the $La_{0.6}Ca_{0.4}MnO_3$ films versus laser fluence. 38
4.6 (2D) and (3D) AFM images of the LCMO films grown on (a) $LaAlO_3$ and (b) $SrTiO_3$ substrates. 40
4.7 Bulk resistivity versus temperature for the films deposited on STO and LAO substrates (a) and the magnetoresistance $\Delta\rho/\rho$ ratio of the LCMO thin films (b). 41
4.8 FWHM and films thickness as a function of the target to substrate distance. . . . 43
4.9 Electrical transport curves of the films deposited at different target to substrate distances. 43
4.10 Resistivity versus temperature (upper graph) and the corresponding MR ratio (lower graph)of a films deposited 4 cm for a field of 4T. 44
4.11 XRD patterns of the $La_{0.7}Ca_{0.3}MnO_3$ thin films grown on $SrTiO_3$ substrates. . . 45
4.12 Cross section TEM image of LCMO/STO, b) $[100]_c$ STO SAED (selected area electron diffraction) pattern, c) $[011]_M$ LCMO SAED pattern. 46
4.13 High resolution of the LCMO/STO interface in cross section geometry. 46
4.14 AFM images of the LCMO films grown on $SrTiO_3$ substrates which were heated in vacuum (left) and in an oxygen atmosphere (right). 49
4.15 Plots of $\ln(\rho/T)$ vs $T^{-1}(K^{-1})$ for the $La_{0.7}Ca_{0.3}MnO_3$ thin films for fast and slow cooling. 49
4.16 Temperature dependence of the resistivity for a film cooled in O_2 atmosphere at applied magnetic fields of 0 and 5 T, respectively. 50
4.17 Temperature dependence of the bulk resistivity for a LCMO film heavy annealed at the applied fields of 0 and 5 T, respectively. Inset: The maximum MR at different magnetic fields. 50
4.18 Survey spectra of the annealed $La_{0.7}Ca_{0.3}Mn_3$ thin film. 51
4.19 O1s core level spectra of the $La_{0.7}Ca_{0.3}Mn_3$ thin films. 52

4.20 The Ca 2p signals of the as deposited and annealed $La_{0.7}Ca_{0.3}MnO_3$ films. 52
4.21 The La $3d_{5/2}$ core level of the as-deposited and annealed $La_{0.7}Ca_{0.3}Mn_3$ films. . . 53
4.22 Mn 3s multiplet splitting of the as-deposited films (continuous line) and annealed at 0.5 mbar O_2 atmosphere (dash-dot line) fitted with Gaussian functions. 53
4.23 Normalized Mn-K main edges of $LaMnO_3$ (Mn^{3+})(thin dotted line) and $SrMnO_3$ (Mn^{4+}) (thin dashed line) reference compounds versus the annealed $La_{0.7}Ca_{0.3}MnO_3$(dash dot line) and as-deposited (continuous line) thin films. The arrows indicate the positions of the main edges. 55
4.24 Surface morphology of the LCMFO/LAO film deposited with N_2O gas pulse. . . 57
4.25 XRD scans of the LCMFO films prepared on $LaAlO_3$(100) substrate 58
4.26 PIXE spectra of the LCMO films (a) and Fe doped LCMO films (b). 59
4.27 Plots of ln(ρ/T) vs 1000/T(K^{-1}) for $La_{0.7}Ca_{0.3}Mn_{1-x}Fe_xO_3$ samples with x=0 and 0.2. 60
4.28 Resistivity of the $La_{0.7}Ca_{0.3}Mn_{0.8}Fe_{0.2}O_3$ films with and without magnetic field as a function of temperature. 60
4.29 Normalized Mn-K main edges of the as deposited $La_{0.7}Ca_{0.3}Mn_{1-x}Fe_xO_3$ (x=0, 0.2) films grown on [$(LaAlO_3)O_3(Sr_2AlTaO_6)_{0.7}$] (100) (LSAT) substrates. The inset shows the Mn-K pre edges of the same films. 61
4.30 Normalized Mn-K main edges of $La_{0.7}Ca_{0.3}Mn_{1-x}Fe_xO_3$ (x=0, 0.2) not-annealed thin films grown on LSAT substrates. Inset: enlargement of the Mn-K pre edge region. 62
4.31 Normalized Fe-K edges of Fe_2O_3 (Fe^{3+}) versus those of the $La_{0.7}Ca_{0.3}Mn_{1-x}Fe_xO_3$ (x=0, 0.2) annealed and not-annealed films. The arrows indicate the positions of the edges. The inset shows an enlargement of the Fe-K pre edges features. 62
4.32 Fe $2p_{3/2}$ XPS peaks for the as deposited $La_{0.7}Ca_{0.3}Mn_{0.8}Fe_{0.2}O_3$ films. The fitting curves inserted in the graph reveal the presence of Fe^{2+} and Fe^{3+} valence states. 63

5.1 The mass distribution of the ionic species generated by 193 nm, 266 nm and 308 nm laser ablation of a LCMO target, using a laser fluence of 1 Jcm^{-2}. 68
5.2 The mass distribution of the ionic species generated by laser ablation of the LCMO target using a laser fluence of 1.5 Jcm^{-2}. 70
5.3 Integrated area in counts of the Ca ions generated by laser ablation at 193 nm and a fluence of 0.8 Jcm^2. 71
5.4 The dependence of the signal intensities of the ionic and neutral Ca species as a function of the laser fluence at a wavelength of 193 nm. 71

5.5 Kinetic energy distribution of Mn^+ and LaO^+ ions emitted by 193 nm laser irradiation of the La- Ca- Mn- O target. The solid curves represent Maxwell Boltzmann fits of the experimental data. 74
5.6 Angular distributions of the La and Ca species induced by 193 nm laser ablation in vacuum from the La- Ca- Mn- O target. The solid lines represents the fits with the function $\cos^n$(t). 76
5.7 Angular distribution of the neutrals and ions emitted during laser ablation of the manganite target at 193 nm, at a laser fluence of 1 Jcm^{-2}. 77
5.8 Angular dependence of the kinetic energy of the Ca ionic species induced by ablation at 193 nm, using a laser fluence of 1 Jcm^{-2}. The arrow indicates the angular spread corresponding to a typical target to substrate distance of 4 cm. . 78
5.9 Time of Flight (TOF) of the ions detected at different angles with respect to the surface normal (a), and the angular distribution of the ionic species determined from the integrated signal as different detection angles (b). The irradiation wavelength was 193 nm and the laser fluence ~3 J/cm^{-2}. 79
5.10 Comparison between the angular distribution of the species detected using a Langmuir probe (LP) and with the mass spectrometer (MS). 80
5.11 Mass distribution of the neutrals and ions generated by laser ablation of a $La_{0.6}Ca_{0.4}MnO_3$ target in a N_2O gas pulse using an irradiation wavelength of 266 nm and a laser fluence of 0.5 Jcm^{-2}. 82
5.12 Off- axis configuration of the mass spectrometer, allowing detection of the species generated by collisions with gas pulse particles (a) and on- axis configuration of the mass spectrometer, allowing detection of the particles along the plume expansion (b). 83
5.13 Kinetic energy spectra of O^+ and O^- in the presence of a N_2O gas pulse (τ= 400 μs and 200 kPa pressure), induced by 266 nm laser irradiation at a laser fluence of 0.5 Jcm^{-2}. 84
5.14 Translation energy of the MnO^+ diatomic species at a static O_2 pressure of 10^{-3} mbar and PRCLA. 84
5.15 Kinetic energy distribution of La^+/LaO^+ and Ca^+/CaO^+ diatomic species measured in PRCLA setup. 85
5.16 Kinetic energy distribution of the diatomic negatively charged species. 86
5.17 Kinetic energy dependence on the atomic mass of the ablated species. 88

6.1 Optical emission spectra generated from laser ablation in vacuum of the $LiMn_2O_4$ target, using a KrF excimer laser (fluence 2 Jcm^{-2}) as an irradiation source. . . 93

6.2 Normalized emission intensity distribution from Mn I, Mn II and Li I species recorded at 6 cm from the target surface in (a) vacuum and (b) at 20 Pa O_2, using a laser fluence of 2 Jcm^{-2}. 94
6.3 Distance versus time dependence of the Li I (a) and Mn II species (b), respectively, in vacuum and at 20 Pa O_2 pressure. The fittings corresponding to the free flight in vacuum (straight line) and plume expansion in gas (based on the shock wave model) are shown. Laser fluence was 2 Jcm^{-2}. 95
6.4 ICCD images of the emission of the plume induced by ablation of the $LiMn_2O_4$ target in vacuum. The images were filtered using appropriate band width filters, allowing detection of single species such as (a) Li I, (b) Mn I and (c) Mn II. Each image is normalized to maximum intensity. The laser fluence was set at 2 Jcm^{-2}. The target position is indicated by the dashed lines. 96
6.5 Emission intensity profiles obtained from plume imaging of Li I, Mn I and Mn II species at different delay times, 620 ns (a) and 920 ns (b). The normalized intensities are shown. The measurements were performed in vacuum at a laser fluence of 2 Jcm^{-2}. 98
6.6 Distance versus time dependence of Li I (a) and Mn II & Mn II species (b) obtained for the analysis of the emission profiles at different delay times. 99
6.7 Plume emission images of the plume induced by $LiMn_2O_4$ ablation at a background pressure of 20 Pa O_2. The time scale varies from 120 ns to 1.12 μs. All images are normalized to maximum intensity. The laser fluence was 2 Jcm^{-2}. . . 100
6.8 Normalized emission intensity distributions perpendicular to the target for (a) Mn I, (b) Mn II, (c) Li I and (d) O with time scale from 220 ns to 2210 ns and a background pressure of 20 Pa O_2. The profiles were selected properly to show the most dominant effects, which occur at different delay times for Li compared to Mn and O. 101
6.9 The temporal evolution of the plume peaks created during plume expansion in background gas, at a pressure of 20 Pa O_2 and at a laser fluence of 2 Jcm^{-2}. The profiles correspond to the Li I species, Mn I species and Mn II species. 102
6.10 Transversal Z(t) and longitudinal R(t) profiles of the hemispherical plume attributed to Mn I (marker $\bullet$), Mn II (marker $\otimes$) and Li I (marker $\triangleright$) species. Measurements were performed at 20 Pa O_2, with typical error bars included. . . 103
6.11 Emissions spectra of the plume induced by ns and fs laser ablation of the $La_{0.6}Ca_{0.4}CoO_3$ target. The emissions spectra were collected at the target surface and in presence of 60 Pa O_2. 113
6.12 Spatial and temporal evolution of emission intensities in vacuum corresponding to the Co neutral species for ns and fs laser ablation. 114

6.13 Schematic of the a and b axes of the plume corresponding to Co I species taken at delay time of 320 ns for ns and fs ablation. 116
6.14 Filtered i- CCD images of the optical emission induced by ns (left) and fs (right) laser ablation, allowing the detection of both La II and Ca II species. 116
6.15 Wavelength filtered i- CCD images using a narrow band width filter which allows detection of the Co I species. Data collected in vacuum using a ns (a) and fs (b) laser as a irradiation source. 117
6.16 Fs laser ablation in vacuum: Profiles along the expansion direction of the Co I species at a delay time of 520 ns and 920 ns. The Gaussians are also included. . 117
6.17 Normalized intensity profiles of the plume induced by fs laser ablation in vacuum. The intensity profiles fitted with Gaussians function are included. The profiles correspond to the plume emission at the delay time of 520 ns. 118
6.18 Maximum emission intensity (a) and the corresponding delay time (b) versus the observation distance for Co I and La II & Ca II pair. Data were recorded in vacuum. 119
6.19 Ns laser irradiation: The plume front position evolution vacuum and at 60 Pa O_2 for La II and Ca II species. The solid lines represent fitting of the liner dependence. 120
6.20 Optical emission of La II and Ca II species induced by ns (a) and fs (b) laser ablation in 60 Pa O_2 pressure. 120
6.21 The temporal evolutions of the Co I emission during expansion in 60 Pa O_2 pressure. The i- CCD images show the plume emission induced by ns laser irradiation (a) and fs laser irradiation (b). 121

List of Tables

2.1 Targets and substrates. 9

4.1 Elemental composition of the powders and thin films measured by EDX and RBS/ERDA. 38

4.2 EDX analysis of the near surface layer and interface layer of the thin films obtained from a target of $La_{0.6}Ca_{0.4}MnO_3$. 39

4.3 Elemental composition of the films after post deposition treatments. 49

4.4 Multiplet splitting values of the Mn 3s core level. 54

4.5 Mössbauer results on $La_{0.7}Ca_{0.3}Mn_{0.8}Fe_{0.2}O_3$ films. 58

4.6 Stoichiometry evaluation of the $La_{0.7}Ca_{0.3}Mn_{0.8}Fe_{0.2}O_3$ thin films. 59

5.1 The ion to neutral ratios for different irradiation wavelengths, e.g. 193 nm, 266 nm and 308 nm, using a laser fluence of 1 Jcm^{-2}. 69

5.2 Parameters obtained from the Maxwell- Boltzmann fitting of the kinetic energy distributions. The parameters $k_B T_z(eV)$, u(m/s) and E_p(eV) denotes the temperature along the expansion direction (z), the corresponding velocity (stream velocity) and most probable energy, respectively. 75

5.3 The main energy values of the species generated by laser irradiation at 266 nm in the presence of the N_2O gas pulse. 87

6.1 The calculated velocities of the species obtained from emission spectroscopy. 96

6.2 Optical emission lines of the manganese and lithium species with emission signal relative intensity and dielectric filters used for plume imaging experiments shown above. 97

6.3 The ablated species velocities calculated with plume imaging. 103

6.4 Mean free path and scattering cross section of the Li, Mn and O species in 20 Pa O_2. The atomic mass, atomic radius and scattering cross section are also included. 107

6.5 Emission lines and lifetimes of the investigated plume species. 112

6.6 The average plume species velocities obtained from emission spectroscopy. 115

6.7 The plume front velocities (m/s) of the species obtained from the plume imaging data. . 121

Bibliography

[1] Singh R.K. Pulsed laser deposition and characterization of high-tc yba2cu3o7-x superconducting thin films. *Materials Science and Engineering: R: Reports*, 22:113–185 29 30 31 32, 15 April 1998.

[2] B. Mitu, P. Bilkova, V. Marotta, S. Orlando, and A. Santagata. Rf plasma reactive pulsed laser deposition of boron nitride thin films. *Applied Surface Science*, 247(1-4):123–127, 2004.

[3] A. A. Voevodin, M. A. Capano, A. J. Safriet, M. S. Donley, and J. S. Zabinski. Combined magnetron sputtering and pulsed laser deposition of carbides and diamond-like carbon films. *Applied Physics Letters*, 69(2):188–190, 1996.

[4] R. Singh, R. Paily, A. Das Gupta, N. Das Gupta, P. Misra, and L. M. Kukreja. Optimized dual temperature pulsed laser deposition of TiO_2 to realize MTOS (metal- TiO_2; SiO_2; Si) capacitors with ultrathin gate dielectric. *Semiconductor Science and Technology*, 20(1):38–43, 2005.

[5] I. Satoh, T. Kobayashi, K. Katayama, T. Okada, and T. Itoh. Magneto-photoluminescence of novel magnetic semiconductor $Zn_{1-x}Cr_xO$ grown by PLD method. *Applied Physics A: Materials Science and Processing*, 79(4-6):1445–1447, 2004.

[6] X. Y. Wang, D. M. Riffe, Y.S. Lee, and M. C. Downer. Time-resolved electron-temperature measurement in a highly excited gold target using femtosecond thermionic emission. *Physical Review B*, 50(11):8016–8019.

[7] S. Amoruso, G. Ausanio, C. de Lisio, V. Iannotti, M. Vitiello, X. Wang, and L. Lanotte. Synthesis of nickel nanoparticles and nanoparticles magnetic films by femtosecond laser ablation in vacuum. *Applied Surface Science*, 247(1-4):71–75, 2005.

[8] P. R. Willmott and J. R. Huber. Pulsed laser vaporization and deposition. *Review of Modern Physics*, 72(1):315–328, 2000.

[9] S. Amoruso, R. Bruzzese, N. Spinelli, and R. Velotta. Characterization of laser-ablation plasmas. *Journal of Physics B: Atomic, Molecular and Optical Physics*, 32:R131–R172, 1999.

[10] M. Vitiello S. Amoruso, A. Sambri and X. Wang. Propagation of $LaMnO_3$ laser ablation plume in oxygen gas. *Applied Surface Science*, 252(13):4712–4716, 2006.

[11] F. J. Morin and J. P. Maita. Electrical properties of silicon containing arsenic and boron. *Physical Review*, 96(1):28–35, 1954.

[12] E. A. G. Hamers, H. M. van Sark, J. Bezemer, W. J. Goedheer, and W. F. van der Weg. On the transmission function of an ion-energy and mass spectrometer. *International Journal of Mass Spectrometry and Ion Processes*, 173(1-2):91–98, 1998.

[13] M. N. Baibich, J. M. Broto, A. Fert, F. Van Dau, F. Nguyen Petroff, P. Eitenne, G. Creuzet, A. Friederich, and J. Chazelas. Giant Magnetoresistance of (001)Fe/(001)Cr Magnetic Superlattices. *Physical Review Letters*, 61(21):2472–2475, 1988.

[14] R. von Helmolt, J. Wecker, B. Holzapfel, L. Schultz, and K. Samwer. Giant negative magnetoresistance in perovskite like $La_{2/3}Ba_{1/3}MnO_x$ ferromagnetic films. *Physical Review Letters*, 71(14):2331–2333, 1993.

[15] M. McCormack, S. Jin, T. H. Tiefel, R. M. Fleming, Julia M. Phillips, and R. Ramesh. Very large magnetoresistance in perovskite-like La-Ca-Mn-O thin films. *Applied Physics Letters*, 64(22):3045–3047, 1994.

[16] E. O. Wollan and W. C. Koehler. Neutron Diffraction Study of the Magnetic Properties of the Series of Perovskite-Type Compounds $La_{1-x}Ca_xMnO_3$. *Physical Review*, 100(2):545–563, 1955.

[17] P. W. Anderson and H. Hasegawa. Considerations on double exchange. *Physical Review*, 100(2):675–681, 1955.

[18] Y. Morimoto, A. Asamitsu, H. Kuwahara, and Y. Tokura. Giant magnetoresistance of manganese oxides with a layered perovskite structure. *Nature*, 380:141–144, 1996.

[19] I.D. Fawcett, G.M. Veith, M. Greenblatt, M. Croft, and I. Nowik. Properties of the perovskites, $SrMn_{1-x}Fe_xO_3$ (x=1/3, 1/2, 2/3). *Solid State Sciences*, 2:821–831(11), 2000.

[20] J. P. Zhou, J. T. McDevitt, J. S. Zhou, H. Q. Yin, J. B. Goodenough, Y. Gim, and Q. X. Jia. Effect of tolerance factor and local distortion on magnetic properties of the perovskite manganites. *Applied Physics Letters*, 75(8):1146–1148, 1999.

[21] Q. Yuan. Strain effect and the phase diagram of $La_{1-x}Ba_xMnO_3$ thin films. *Physical Review B (Condensed Matter and Materials Physics)*, 70(6):066401, 2004.

[22] A. M Haghiri-Gosnet and J. P Renard. Cmr manganites: physics, thin films and devices. *Journal of Physics D: Applied Physics*, 36(8):R127–R150, 2003.

[23] C. Zener. Interaction between the d-Shells in the Transition Metals. II. Ferromagnetic Compounds of Manganese with Perovskite Structure. *Physical Review*, 82(3):403–405, 1951.

[24] E. Gommert, H. Cerva, A. Rucki, R. V. Helmolt, J. Wecker, C. Kuhrt, and K. Samwer. Structure and magnetoresistive properties in La- manganite thin films. *Journal of Applied Physics*, 81(8):5496–5498, 1997.

[25] H. Y. Hwang, S. W. Cheong, P. G. Radaelli, M. Marezio, and B. Batlogg. Lattice Effects on the Magnetoresistance in Doped LaMnO_3. *Physcal Review Letters*, 75(5):914–917, 1995.

[26] B. C. Min, Y. H. Choi, S. H. Moon, S. M. Lee, S. Y. Lee, and B. Oh. Double-sided $YBa_2Cu_3O_{3-\delta}$ thin films made by off-axis pulsed laser deposition. *Superconductor Science and Technology*, 14(8):543–547, 2001.

[27] M. Ziese, H. C. Semmelhack, K. H. Han, S. P. Sena, and H. J. Blythe. Thickness dependent magnetic and magnetotransport properties of strain-relaxed $La_{0.7}Ca_{0.3}MnO_3$ films. *Journal of Applied Physics*, 91(12):9930–9936, 2002.

[28] M. Koubaa, A. M. Haghiri-Gosnet, R. Desfeux, Ph. Lecoeur, W. Prellier, and B. Mercey. Crystallinity, surface morphology, and magnetic properties of $La_{0.7}Sr_{0.3}MnO_3$ thin films: An approach based on the laser ablation plume range models. *Journal of Applied Physics*, 93(9):5227–5235, 2003.

[29] E. van de Riet, J. C. S. Kools, and J. Dieleman. Incongruent transfer in laser deposition of FeSiGaRu thin films. *Journal of Applied Physics*, 73(12):8290–8296, 1993.

[30] W. Zhang, X. Wang, and I. W. Boyd. Incongruent transfer related to surface segregation in pulsed-laser-deposited La-Ca–Mn-O films. *Applied Physics Letters*, 73(19):2745–2747, 1998.

[31] Th. Dumont, T. Lippert, M. Döbeli, H. Grimmer, J. Ufheil, P. Novak, A. Wursig, U. Vogt, and A. Wokaun. Influence of experimental parameter on the Li-content of $LiMn_2O_4$ electrodes produced by pulsed laser deposition. *Applied Surface Science*, 252(13):4902–4906, 2006.

[32] C. J. Lu, Z. L. Wang, C. Kwon, and Q. X. Jia. Microstructure of epitaxial $La_{0.7}Ca_{0.3}MnO_3$ thin films grown on $LaAlO_3$ and $SrTiO_3$. *Journal of Applied Physics*, 88(7):4032–4043, 2000.

[33] R. Desfeux, A. Da Costa, and W. Prellier. Thickness dependence on the surface morphology and the magnetic microstructure of $La_{0.7}Sr_{0.3}MnO_3$ films under different strains. *Surface Science*, 497(1-3):81–92, 2002.

[34] X. T. Zeng, H. K. Wong, J. B. Xu, and I. H. Wilson. Step flow growth of (La,Ca)$MnO_{3-\delta}$ thin films on (110)$NdGaO_3$. *Applied Physics Letters*, 67(22):3272–3274, 1995.

[35] T. K. Nath R. A. Rao, D. Lavric, C. B. Eom, L. Wu, and F. Tsui. Three-dimensional strain states and crystallographic domain structures of epitaxial colossal magnetoresistive $La_{0.8}Ca_{0.2}MnO_3$ thin films. *Applied Physics Letters*, 30(22):3294–3296, 1995.

[36] J. C. Lee, D. G. You, S. Y. Ie, M. C. Sung, H. S. Song, H. S. Park, S. H. Lee S. K. Kang, K. Jeong, S. J. Kim, and C. S. Kim. Annealing effect on the magnetoresistance in $La_{0.75}Ca_{0.25}MnO_3$ thin films grown on Si (100) substrates. *Journal of Applied Physics*, 91(1):221–224, 2002.

[37] M. J. Montenegro, M. Döbeli, T. Lippert, S. Muller, A. Weidenkaff, P. R. Willmott, and A. Wokaun. Microstructures and film properties of $La_{0.7}Ca_{0.3}CoO_3$ produced by pulsed reactive crossed-beam laser ablation. *Thin Solid Films*, 453-454:182–186, 2004.

[38] J. Choi, J. Zhang, S.H. Liou, P. A. Dowben, and E. W. Plummer. Surfaces of the perovskite manganites $La_{1-x}Ca_xMnO_3$. *Physical Review B*, 59(20):13453–13459, 1999.

[39] P. Delichere N. H. Batis and H. Batis. *Applied Catalyst A: General*, 282:173–177, 2005.

[40] E. Beyreuther, S. Grafstrom, L.M. Eng, C. Thiele, and K. Dorr. XPS investigation of Mn valence in lanthanum manganite thin films under variation of oxygen content. *Physical Review B (Condensed Matter and Materials Physics)*, 73(15):155425, 2006.

[41] M. Croft, D. Sills, M. Greenblatt, C. Lee, K. V. Ramanujachary S.W. Cheong, and D. Tran. Systematic Mn d-configuration change in the $La_{1-x}Ca_xMnO_3$ system: A Mn K- edge XAS study. *Phys. Rev. B*, 55(14):8726–8732, 1997.

[42] A. J. Millis, P. B. Littlewood, and B. I. Shraiman. Double Exchange Alone Does Not Explain the Resistivity of $La_{1-x}Sr_xMnO_3$. *Physical Review Letters*, 74(25):5144–5147, 1995.

[43] K. H. Ahn, X. W. Wu, K. Liu, and C. L. Chien. Magnetic properties and colossal magnetoresistance of La(Ca)MnO_3 materials doped with Fe. *Physical Review B*, 54(21):15299–15302, 1995.

[44] J. W. Cai, C. Wang, B. G. Shen, J. G. Zhao, and W. S. Zhan. Colossal magnetoresistance of spin-glass perovskite $La_{0.67}Ca_{0.33}Mn_{0.9}Fe_{0.1}O_3$. *Applied Physics Letters*, 71(12):1727–1729, 1997.

[45] P.D. Battle, W.R. Branford, A. Mihut, M.J. Rosseinsky, J. Singleton, J. Sloan, L.E. Spring, and J.F. Vente. Structural chemistry and electronic properties of the n = 3 ruddlesden - Popper phases $Ca_4Mn_2FeO_{9.75}$ and $Sr_4Mn_2FeO_{9.80}$. *Chemistry of Materials*, 11(3):674–683, 1999.

[46] S. Canulescu, T. Lippert, A. Wokaun, R. Robert, D. Logvinovich, A. Weidenkaff, M. Dobeli, and M. Schneider. Preparation of epitaxial $La_{0.6}Ca_{0.4}Mn_{1-x}Fe_xO_3$ (x = 0, 0.2) thin films: Variation of the oxygen content. *Progress in Solid State Chemistry*, 35(2-4):241–248, 2007.

[47] J. Schubert, M. J. Schöninga, Yu. G. Mourzinab, A. V. Leginb, Yu. G. Vlasovb, W. Zandera, and H. Lütha. Multicomponent thin films for electrochemical sensor applications prepared by pulsed laser deposition. *Sensors and Actuators B: Chemical*, 76:327–330, 2001.

[48] P.R. Willmott and H. Spillmann. Materials by design—exploiting the unique properties of pulsed laser deposition for the synthesis of novel hard materials and structures. *Applied Surface Science*, 197–198:432–437, 2002.

[49] P. R. Willmott, R. Herger, and C. M. Schlepütz. Multilayers, alloys, and complex profiles by pulsed laser deposition using a novel target geometry. *Thin Solid Films*, 1:436– 439, 2004.

[50] R. Jordan, D. Cole, J.G. Lunney, K. Mackay, and D. Givord. Pulsed laser ablation of copper. *Applied Surface Science*, 86:24–28, 1995.

[51] G. Koren, A. Gupta, R. J. Baseman, M. I. Lutwyche, and R. B. Laibowitz. Laser wavelength dependent properties of $YBa_2Cu_3O_{7-\delta}$ (YBCO) thin films deposited by laser ablation. *Applied Physics Letters*, 55(23):2450–2452, 1989.

[52] H.J. Dang, Z. H. Han, Z. G. Dai, and Q. Z. Qin. Characterization of laser ablated species from a La-Ca-Mn-O target by angle- and time-resolved mass spectrometry. *International Journal of Mass Spectrometry*, 178:205–212, 1998.

[53] H.J. Dang and Q. Z. Qin M.J. Zhou. Optical emission spectrometric characterization of plumes generated from laser-ablated $Pr_{0.67}Sr_{0.33}MnO_3$. *Applied Surface Science*, 140:118–125, 1999.

[54] S. Amoruso, V. Berardi, R. Bruzzese, N. Spinelli, and X. Wang. Kinetic energy distribution of ions in the laser ablation of copper targets. *Applied Surface Science*, 127-129:953– 958, 1998.

[55] L. Torrisi, F. Caridi, D. Margarone, A. Picciotto, A. Mangione, and J.J. Beltrano. Carbon-plasma produced in vacuum by 532 nm–3 ns laser pulses ablation. *Applied Surface Science*, 252(18):6383–6389, 1990.

[56] J. Gottmann, G. Schlaghecken, and E.W. Kreutz. Determining the properties of pulsed laser deposited thin films by controlling the kinetic energy of the film-forming particles. *Applied Physics A: Materials Science and Processing*, 69(1):S597–S600, 1999.

[57] J. C. S. Kools, T. S. Baller, S. T. De Zwart, and J. Dieleman. Gas flow dynamics in laser ablation deposition. *Journal of Applied Physics*, 71(9):4547–4556, 1999.

[58] S. Amoruso, M. Armenante, V. Berardi, R. Bruzzese, G. Pica, and R. Velotta. Chargel species analysis as a diagnostic tool for laser produced plasma characterization. *Applied Surface Science*, 106(9):507–512, 1996.

[59] C. R. Phipps, T. P. Turner, R. F. Harrison, G. W. York, W. Z. Osborne, G. K. Anderson, X. F. Corlis, L. C. Haynes, H. S. Steele, K. C. Spicochi, and T. R. King. Impulse coupling to targets in vacuum by KrF, HF, and CO_2 single-pulse lasers. *Journal of Applied Physics*, 64(3):1083–1096, 1988.

[60] Wenbin Wu, K. H. Wong, X.-G. Li, C. L. Choy, and Y. H. Zhang. Effect of annealing in reduced oxygen pressure on the electrical transport properties of epitaxial thin film and bulk $(La_{1-x}Nd_x)_{0.7}Sr_{0.3}MnO_3$. *Journal of Applied Physics*, 87(6):3006–3010, 2000.

[61] P.R. Willmott, R. Herger, M.C. Falub, L. Patthey, M. Döbeli anmd C.V. Falub, M. Shi, and M. Schneider. Pulsed laser deposition of atomically flat $La_{1-x}Sr_xMnO_3$ thin films using a novel target geometry. *Applied Physics A: Materials Science and Processing*, 79(4-6):1199–1201, 2004.

[62] P. Lecoeur, A. Gupta, P. R. Duncombe, G. Q. Gong, and Gang Xiao. Emission studies of the gas-phase oxidation of Mn during pulsed laser deposition of manganates in O_2 and N_2O atmospheres. *Journal of Applied Physics*, 80(1):513–517, 1996.

[63] E. R. Buzin, W. Prellier, Ch. Simon, S. Mercone, B. Mercey, B. Raveau, J. Sebek, and J. Hejtmanek. Control of the colossal magnetoresistance by strain effect in $Nd_{0.5}Ca_{0.5}MnO_3$ thin films. *Applied Physics Letters*, 79(5):647–649, 2001.

[64] S. C. Langford, L. C. Jensen, J. T. Dickinson, and L. R. Pederson. Negative charge emission due to excimer laser bombardment of sodium trisilicate glass. *Journal of Applied Physics*, 68(8):4253–4257, 1990.

[65] Y. Konishi, Z. Fang, M. Izumi, T. Manako, M. Kasai, H. Kuwahara, M. Kawasaki, K.Terakura, and T. Yoshinori. Orbital-state-mediated phase-control of manganites. *Journal of the Physical Society of Japan*, 68(12):3790–3793, 1999.

[66] M. Allegrini, F. Fuso, G. Lorenzi, L. N. Vyacheslavov, and E. Arimondo. Spectroscopy as in-situ diagnostics for pulsed laser deposition of superconductive and ferroelectric thin films. *Applied Surface Science*, 106:438–446, 1996.

[67] C. Julien, E. Haro-Poniatowski, M. A. Camacho-Lopez, L. Escobar-Alarcon, and J. Jimenez-Jarquin. Growth of $LiMn_2O_4$ thin films by pulsed-laser deposition and their electrochemical properties in lithium microbatteries. *Materials Science and Engineering B-Solid State Materials for Advanced Technology*, 72(1):36–46, 2000.

[68] A. Perea, J. Gonzalo, C. N. Afonso, C. Vivien, and Ch. Leborgne. Fast imaging of the plume expansion produced by laser ablation of $LiNbO_3$. *Applied Physics A: Materials Science and Processing*, 69:S141–S144, 1999.

[69] D. O'Mahony, J. G. Lunney, G. Tobin, and E. McGlynn. Pulsed laser deposition of manganese doped GaN thin films. *Solid-State Electronics*, 47(3):533–537, 2003.

[70] S. Amoruso, J. Schou, and J. G. Lunney. Multiple-scattering effects in laser ablation plume propagation in gases. *Europhysics Letters (EPL)*, 47(3):436–442, 2006.

[71] J. Giapintzakis, A. Sfounis, and M. Velegrakis. A comparative mass spectroscopic study between infrared and ultraviolet laser ablation of a superconducting $YBa_2Cu_3O_{7-x}$ target . *International Journal of Mass Spectrometry*, 189(1):1–7, 2006.

[72] C. J. Druffner, G. P. Perram, and R. R. Biggers. Time-of-flight emission profiles of the entire plume using fast imaging during pulsed laser deposition of $YBa_2Cu_3O_{7-x}$. *Review of Scientific Instruments*, 76(9):093101–093107, 2005.

[73] N. Arnold, J. Gruber, and J. Heitz. Spherical expansion of the vapor plume into ambient gas: an analytical model. *Applied Physics A: Materials Science and Processing*, 69:S87–S93, 1999.

[74] M. Tanaka, Y. Fujisawa, T. Nakajima, Y. Tasaka, K. Ota, and S. Usami. Space- and time-resolved optical spectroscopy of plumes generated by laser ablation of NiO in a vacuum. *Journal of Applied Physics*, 83:3379–3385, 1998.

[75] D. O'Mahony, J. Lunney, T.Dumont, S.Canulescu, T. Lippert, and A. Wokaun. Laser-produced plasma ion characteristics in laser ablation of lithium manganate. *Applied Surface Science*, 254:811–815, 2007.

[76] J. A. Chaos, R. W. Dreyfus, A. Perea, R. Serna, J. Gonzalo, and C. N. Afonso. Delayed release of Li atoms from laser ablated lithium niobate. *Applied Physics Letters*, 76:649–651, 2000.

[77] R. F. Wood, J. N. Leboeuf, D. B. Geohegan, A. A. Puretzky, , and K. R. Chen. Concentration of li atoms in plasmas produced from laser ablation of linbo3. *Physical Review B*, 58:103–110,, 1998.

[78] D.B. Geohegan and A.A. Puretzky. Dynamics of laser ablation plume penetration through low pressure background gases. *Applied Physics Letters*, 67(2), 1995.

[79] V. Berardi, S. Amoruso, N. Spinelli, M. Armenante, R. Velotta, F. Fuso, M. Allegrinim, and E. Arimondo. Diagnostics of $YBa_2Cu_3O_{7-\delta}$ laser plume by time-of-flight mass spectrometry. *Journal of Applied Physics*, 76(12):8077–8087, 1998.

[80] A. Issa P. E. Dyer and P. H. Key. An investigation of laser ablation and deposition of Y-Ba-Cu-O in an oxygen environment. *Applied Surface Science*, 46(1-4):89–95, 1990.

[81] G. G. Amatucci, J. M. Tarascon, and L. C. Klein. CoO_2, the end member of the Li_xCoO_2 solid solution. *Journal of the Electrochemical Society*, 143(3):1114–1123, 1996.

[82] E. Millon, J. Perrière, R. M. Défourneau, D. Défourneau, O. Albert, and J. Etchepare. Femtosecond pulsed-laser deposition of $BaTiO_3$. *Applied Physics A: Materials Science and Processing*, 77:73–80, 2003.

[83] D. Brodoceanu, A. Manousaki, I. Zergioti, A. Klini, M. Dinescu, and C. Fotakis. Growth of polycrystalline $La_{0.5}Sr_{0.5}CoO_3$ films by femtosecond pulsed laser deposition. *Applied Physics A: Materials Science and Processing*, 70:911–914, 2004.

[84] S. Muller, K. Striebel, and O. Haas. $La_{0.6}Ca_{0.4}CoO_3$ - a stable and powerful catalyst for bifunctional air electrodes. *Electrochimica Acta*, 39(11-12):1661–1668, 1994.

[85] J. Gonzalo, J.M. Ballesteros, and C.N. Afonso. Expansion dynamics of Bi atoms produced by laser ablation of Bi and BGO targets. *Applied Surface Science*, 138-139:52–56, 1999.

[86] J. Perriere, E. Millon, W. Seiler, C. Boulmer-Leborgne, V. Craciun, O. Albert, J. C. Loulergue, and J. Etchepare. Growth of polycrystalline $La_{0.5}Sr_{0.5}CoO_3$ films by femtosecond pulsed laser deposition. *Journal of Applied Physics*, 91:690–696, 2002.

[87] A. De Bonis, A. Galasso, V. Marotta, S. Orlando, A. Santagata, R. Teghil, S. Veronesi, P. Villani, and A. Giardini. Pulsed laser ablation of indium tin oxide in the nano and femtosecond regime: Characterization of transient species. *Applied Surface Science*, 252(13):4632–4636, 2006.

[88] A. V. Bulgakov, I. Ozerov, and W. Marine. Cluster emission under femtosecond laser ablation of silicon. *Thin Solid Films*, 453-454:557–561, 2003.

CURRICULUM VITAE

Stela Canulescu

PERSONAL Born on April 2, 1979 in Pitesti, Romania
Citizen of Romania

EDUCATION

2004- 2007 PhD. Student at Paul Scherrer Institut
Supervisors: PD Dr. T. Lippert and Prof. A. Wokaun
Topic: Growth and characterization of thin manganite films and in- situ analysis of the laser- induced plasma

2002- 2004 Master degree at University of Bucharest, Faculty of Physics, Romania
Specialization: Master in Nonconventional Technologies with Lasers and Plasma
Title of project: Characterization of barium titanate thin films deposited by Radiofrequency discharge assisted pulsed laser deposition

1997- 2002 Bachelor studies at University of Bucharest, Faculty of Physics, Romania
Specialization: Technological Physics and Optotechnics
Title of project: A study about PLZT thin films deposited by pulsed laser deposition

1993- 1997 College "Ion Barbu, Pitesti, Romania
Profile: Mathematics-Computer science

LIST OF PUBLICATIONS

2006 **S. Canulescu**, T. Lippert, H. Grimmer, A. Wokaun, R. Robert, D. Logvinovich, A. Weidenkaff, M.Döbeli, Structural characterization and magnetoresistance of manganates thin films and Fe-doped manganates thin films, Applied Surface Science 252, 4599- 4603, 2006.

2007 **S. Canulescu**, Th. Lippert, A. Wokaun, R. Robert, D. Logvinovich, A.Weidenkaff, M. Döbeli, M. Schneider, Preparation of epitaxial $La_{0.6}Ca_{0.4}Mn_{1-x}Fe_xO_3$ (x= 0, 0.2) thin films: variation of the oxygen content, Progress in Solid State Chemistry 35, 241- 248, 2007.

2007 **S. Canulescu**, Th. Lippert, A. Wokaun, M. Döbeli, A. Weidenkaff, R. Robert, D. Logvinovich, The effect of the fluence on the properties of La-Ca-Mn-O thin films prepared by pulsed laser deposition, Applied Surface Science 253, 8174–8178, 2007.

2007 C. N. Borca, **S. Canulescu**, F. Loviat, D. Grolimund, T. Lippert, A. Wokaun, Electronic Properties of Pulsed Laser Deposited $La_{0.7}Ca_{0.3}Mn_{0.8}Fe_{0.2}O_3$ thin films, Applied Surface Science 254, 1352–1355, 2007.

2007 **S. Canulescu**, Th. Lippert, A. Wokaun, Mass and kinetic energy distribution of the species generated by laser ablation of $La_{0.6}Ca_{0.4}MnO_3$, Applied Physics A: Materials Science & Technology, 2008.

2007 D. O' Mahony, J. Lunney, Th. Dumont, **S. Canulescu**, T. Lippert, A. Wokaun, Laser produced Plasma Ion Dynamics and Composition in PLD of Lithium Manganate, Applied Surface Science 254, 811–815, 2007.

2008 A. Weidenkaff, R. Robert, M. H. Aguirre, L. Bocher, T. Lippert, S. Canulescu, Development of Thermoelectric Oxides for Renewable Energy Conversion Technologies, Renewable Energy 33, 342–347, 2008.

2008 M.H. Aguirre, **S. Canulescu**, R. Robert, N. Homazava, D.Logvinovich, L. Bocher, T. Lippert, M. Döbeli and A. Weidenkaff, Structure, microstructure and high temperature transport properties of $La_{1-x}Ca_xMnO_{3-\delta}$ thin films and polycrystalline bulk materials, Journal of Applied Physics 103, 013703- 013716, 2008.

2008 **S. Canulescu**, E. Papadopoulou, D. Anglos, T. Lippert, A. Wokaun, Plume expansion during laser ablation of $LiMn_2O_4$ target, Journal of Applied Physics, 2008.

2008 **S. Canulescu**, E. Papadopoulou, D. Anglos, T. Lippert, A. Wokaun, Plume emission induced by fs and ns laser ablation of $La_{0.6}Ca_{0.4}CoO_3$ target: Comparisons between plume dynamics- in preparation.

BOOK CHAPTER

2008 S. Canulescu, C.N. Borca, T. Lippert, M. Döbeli, P. Schaaf, D. Grolimund, A.Wokaun, *Electronic Properties of Pulsed Laser Deposited $La_{0.7}Ca_{0.3}Mn_{1-x}Fe_xO_3$ (x=0, 0.2) thin films*, Nova Science Publishers- in preparation